TÉCNICO LISBOA

Study of Photons Orbital Angular Momentum for Optical Communications

André Madeira Bastos da Cunha

Thesis to obtain the Master of Science Degree in

Engineering Physics

Supervisors: Professor Paulo Sérgio de Brito André

Professor Gonçalo Nuno Marmelo Foito Figueira

Examination Committee

Chairperson:	Professor Luís Paulo da Mota Capitão Lemos Alves
Supervisor:	Professor Gonçalo Nuno Marmelo Foito Figueira
Members of the Committee:	Professor João Alberto dos Santos Mendanha Dias
	Professor Armando Humberto Moreira Nolasco Pinto

November 2015

B

A journey of a thousand miles begins with a single step.

老子

Acknowledgments

I'd like to start by thanking my parents Juvenal and Lídia, who have encouraged and supported me throughout all my life and my wife Joana who stood by my side and provided me great support during this journey.

Furthermore, this work would not have been possible without the openness, encouragement and great support provided by both Professors Paulo André and Gonçalo Figueira. I would like to remark that only the promptness and openness of both to inter-collaboration and new ideas provided the necessary basis for the bridging between physics and optical communications by allowing this work, which focus on an albeit exotic, but rather trendy and innovative subject.

And of course, I must also thank the support of Instituto de Telecomunicações (IT) and Fundação para a Ciência e Tecnologia (FCT) who provided equipment and financial support to enable this work, the Group of Lasers and Plasmas (GOLP), Instituto de Plasmas e Fusão Nuclear (IPFN) who provided the necessary installations at Laboratório de Lasers Intensos (L2I) for our setup and provided multiple optical equipment but also a scientific environment of highly capable and helpful people who provided support throughout this work.

Finally, I want to acknowledge my colleagues and friends, who were there for me when I needed them, especially João Romão for the prolific discussions and insights and Pedro Miguel Cruz and Manuel Nascimento for their patience and companionship but also colleagues Alexandra Gouveia and Tiago Guerra Marques given the work we developed together years ago.

For the ones unmentioned, a word of apology but the assurance that I hold a special place for you in my heart.

Resumo

A capacidade de tráfego de dados na internet está rapidamente a atingir os limites impostos pelos efeitos não lineares da fibra óptica, tendo quase esgotado os graus de liberdade disponíveis necessários para multiplexar ortogonalmente o tráfego de dados. Desta forma, resultados recentes sugerem que o momento angular orbital (MAO) dos fotões talvez possa ser usado como grau de liberdade adicional para este fim, providenciando em teoria, um número potencialmente ilimitado de estados ortogonais, apresentando-se assim como um possível salto de gigante para as redes de telecomunicações do futuro.

Palavras Chave

Momento Angular Orbital (MAO), Telecomunicações Ópticas, Óptica em Espaço Livre, Laguerre-Gaussiano (LG), Óptica, Modulador Espacial de Luz (MEL)

Abstract

The internet data traffic capacity is rapidly reaching the limits imposed by optical fiber nonlinear effects, having almost exhausted the available degrees of freedom needed to orthogonally multiplex data. Therefore the need urges to develop new methods in order to avoid the upcoming capacity crunch using classical communications channels. In this regard, recent results have suggested that the use of the orbital angular momentum (OAM) of photons as an additional degree of freedom is potentially unlimited in the number of achievable orthogonal states, therefore presenting itself as a possible major technological leap for future communication networks.

Keywords

Orbital Angular Momentum (OAM), Optical Communications, Free Space Optics (FSO), Laguerre-Gaussian (LG), Optics, Spatial Light Modulator (SLM)

Publications, Conferences & Presentations

- André B Cunha, Gonçalo Figueira, and Paulo S André. Enabling the study of photons OAM applications for optical communications. In *The 23rd Annual International Conference on Advanced Laser Technologies ALT'15*, Faro, 2015. Instituto de Telecomunicações
- André B Cunha, Gonçalo Figueira, and Paulo S André. Generation of Orbital Angular Momentum Beams . In *10a Conferência Nacional de Telecomunicações CONF TELE 2015*, Aveiro, 2015. Instituto de Telecomunicações

Under preparation:

- André B Cunha, Gonçalo Figueira, and Paulo S André. Enabling the study of photons OAM applications for optical communications. *Optical and Quantum Electronics*, 2015

Contents

List of Figures

List of Tables

ASK Amplitude-Shift Keying

CCD Charge-Coupled Device

CGH Computer Generated Hologram

CMOS Complementary Metal-Oxide Semiconductor

CoWDM Coherent Wavelenght-Domain Multiplexing

CWDM Coarse Wavelenght-Domain Multiplexing

DC Direct Current

DEMUX Demultiplexing

DMD Digital Micromirror Device

EASLM Electrically Addressed Spatial Light Modulator

ETDM Electronic Frequency-Division Multiplexing

FFT Fast Fourier Transform

FSK Frequency-Shift Keying

FTTH Fiber-To-The-Home

HG Hermite-Gaussian

HWP Half Wave Plate

LC Liquid Crystal

LCoS Liquid Crystal on Silicon

LG Laguerre-Gaussian

MQW Multiple Quantum Well

MSK Minimum-Shift Keying

MUX Multiplexing

OAM Orbital Angular Momentum

OASLM Optically Addressed Spatial Light Modulator

oCDMA optical Code-Division Multiple-Access

OFDM Orthogonal Frequency-Division Multiplexing

OOK On/Off Keying

OTDM Orthogonal Time-Division Multiplexing

PAN Parallel Alligned Nematic Liquid Crystal

PDM Polarisation-Division Multiplexing

PolSK polarisation-Shift Keying

PPM Pulse-Position Modulation

PSK Phase-Shift Keying

QAM Quadrature Amplitude Modulation

QPSK Quadrature Phase-Shift Keying

QWP Quarter Wave Plate

RF Radio Frequency

SDM Spatial-Domain Multiplexing

SLM Spatial Light Modulator

SNR Signal To Noise Ratio

TDM Time-Division Multiplexing

TEM Transverse Electromagnetic Mode

TN Twsited Nematic Liquid Crystal

VAN Vertically Alligned Nematic Liquid Crystal

WDM-PDM Wavelenght-Domain Multiplexing with polarisation-Division Multiplexing

WDM Wavelenght-Domain Multiplexing

WFS Wavefront Sensor

1

Introduction & State of the Art

Contents

Motivation

Over the last 50 years, a fast transition from analog to digital communications has enabled lossless universal processing of information [4]. The synergy between the advances in digital semiconductor technologies and a cost-effective mass-production of highly functional, reliable and power efficient microchips enabled a worldwide spread of these technologies, present in any electronic device today, from high-end internet routers to low-end consumer electronics [5]. The growing establishment of this reality enables the need for better data transport technologies, ranging from short on-chip [6] and board-level [7] data buses all the way to long-distance transport networks across the planet [8], to deep-space probes [9].

Before advancing within the optical communication systems, it is pertinent to contextualize these systems in the broader world of communication technologies. Optical communication technologies usually have the edge over baseband electronic or Radio Frequency (RF) transmission systems whenever high aggregate bit rates or long distances are needed. These features are both deeply rooted in physics: the high optical carrier frequencies allow for high capacity systems at small relative bandwidths and transmission losses at optical frequencies are usually very small compared to the traditional alternative technologies. As optical integration improves and transponder footprint, power consumption, and costs diminish, optical communications are replacing their electronic counterparts, starting with capacity-constrained and sensitivity-constrained systems and slowly becoming a palpable reality in systems limited by hardware implementation aspects [5].

This process started on a large scale in the late 1970's with the most demanding requirements for both bandwidth and distance in applications of terrestrial [8] and undersea [10] transport. Nowadays, with massive Fiber-To-The-Home (FTTH) deployments underway, optics is currently paving its way to optical chip-to-chip and eventually on-chip communications once electronic transmission reaches its limits regarding capacity [6], power consumption [11] and interface density [7].

Within this framework, juggling the sensitivity, capacity and implementation constraints of an optical communications system, is necessary to choose the best suited modulation and multiplexing techniques based on the available physical dimensions often referred as degrees of freedom [5].

This reality spotlights optical communications as both the present choice and future hope for faster, more efficient communication technologies. However, the challenge for further increasing the systems capacity is a constant struggle urging for the discovery, research and development of additional degrees of freedom. Most notably as an example, the internet data traffic capacity is rapidly reaching the limits imposed by optical fiber nonlinear effects, having almost exhausted the available degrees of freedom needed to orthogonally multiplex data [5].

Recent results have demonstrated that the use of the Orbital Angular Momentum (OAM) of photons as an additional degree of freedom in multiplexing is possible [12]. Since OAM offers a theoretically unlimited number of orthogonal states, it presents itself as a possible contender for a major technological leap in the future of both classical and quantum communications opening a venue of research and development in its regard [13].

Optical Communications

Multiplexing & Modulation

Ingrained in the optical communication systems is the definition of orthogonality, which in a broad sense, means that if two of these dimensions are used to send two different signals, then it will be possible to distinguish them at the receiver without them impacting each other's detection. If these signals share a common transmission medium, we refer to it as multiplexing. The method by which information is imprinted onto an optical carrier, and in its most broad definition, with the inclusion of coding to prevent transmission errors is referred to as modulation [5].

Currently Available Multiplexing Techniques

We shall now review the state of the art regarding the currently available multiplexing and modulation techniques for optical signals. Since orbital angular momentum appears to pose itself directly as a more physical aspect regarding data transmission, coding mechanisms are at this point not the key subject of this discussion, and therefore will only approached if needed.

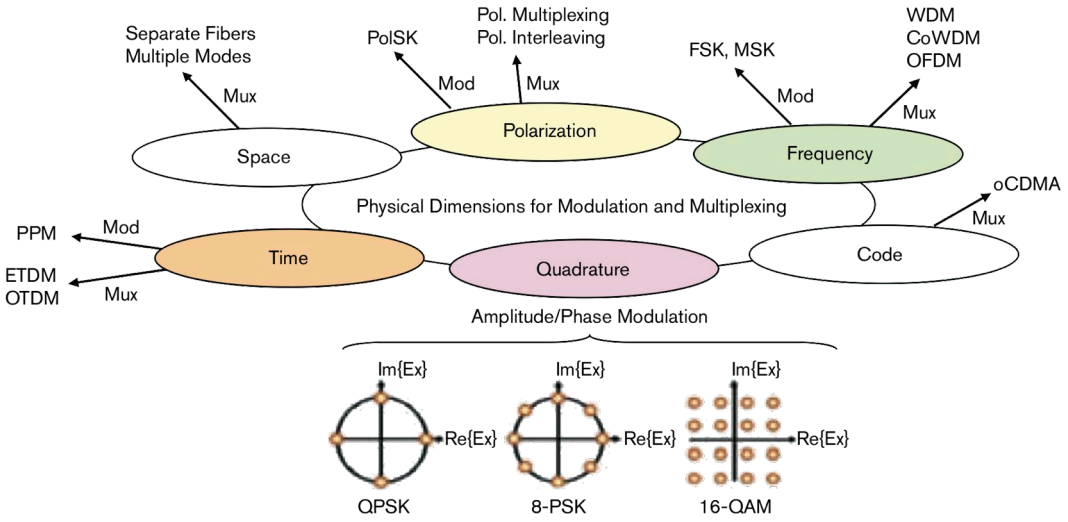

Winzer [5]

Figure 1.1: Perspective diagram over multiplexing and modulation techniques according to each physical dimension used.

Wavelenght-domain Multiplexing (WDM)

In Wavelenght-Domain Multiplexing (WDM), optical signals with different carrier frequency are naturally orthogonal and individual bit streams can be recovered using optical bandpass filters or a technique involving electronic filters followed by a coherent receiver front-end [5, 14]. If signals leak energy into neighboring frequency bins, we have WDM crosstalk, which results in a compromised orthogonality which implies that perfect reconstruction of the signal may no longer be possible. To reduce this problem, one may try to add another physical property of optical signals, performing polarisation interleaving in order to improve the orthogonality between frequency bins [5].

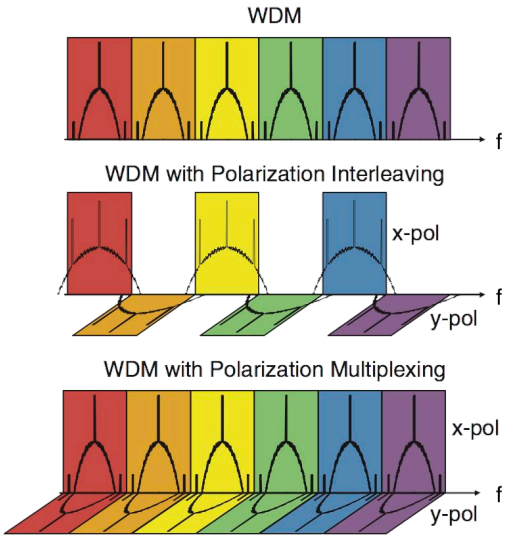

Winzer [5]

Figure 1.2: Image depicting WDM, WDM with polarisation interleaving and WDM-PDM.

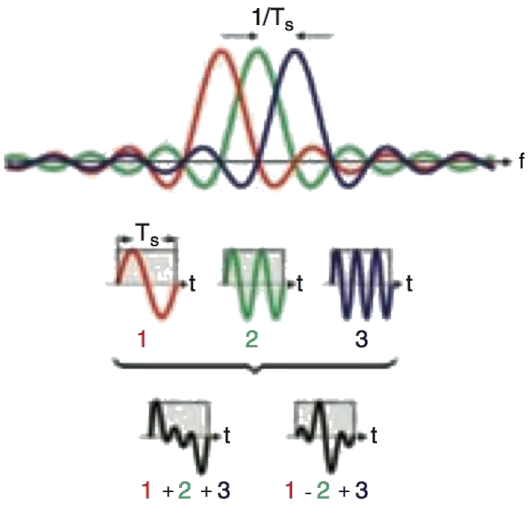

Winzer [5]

Figure 1.3: Graphic depicting TDM basic principle.

Polarisation-division Multiplexing (PDM)

In Polarisation-Division Multiplexing (PDM), two orthogonal signals are transmitted on the polarisation plane in a single mode fiber. In order to perform this technique one may recover the signal by using a polarisation beam splitter whose axis are always kept aligned with the signal polarisations on what we call 'polarisation control', or by detecting two arbitrary orthogonal polarisations using coherent detection on what is referred to as 'polarisation diversity' which also requires further numerical processing because the signal will be randomly rotated after propagating through an optical fiber [5, 14].

CoWDM, OFDM, ETDM, OTDM & oCDMA

Another way of achieving orthogonality in the frequency domain allows overlapping but imposes an exactly defined frequency spacing equal to the inverse of the Nyquist frequency. As it is expected, in Coherent Wavelenght-Domain Multiplexing (CoWDM) and Orthogonal Frequency-Division Multiplexing (OFDM) the original individual bit streams can be easily recovered by decomposing the signal using the Fast Fourier Transform (FFT) optically in the former and electronically in the latter [15, 16]. In the time domain, one refers to these techniques as Orthogonal Time-Division Multiplexing (OTDM) and Electronic Frequency-Division Multiplexing (ETDM) respectively [5]. If the orthogonal waveforms are not sine waves but rather orthogonal sequences of short pulses or 'chirps', we arrive at optical Code-Division Multiple-Access (oCDMA) [5].

Spatial-domain multiplexing (SDM)

By sending different signals on different parallel waveguides, one can make use of the Spatial-Domain Multiplexing (SDM). This is particularly of interest in the implementation of constrained systems such as rack to rack interconnects and shorter connections, since frequency stable lasers, filters and the subsequent signal processing schemes over a significant temperature range leads to power-consuming solutions or simply

become problematic and overly complex to deliver. Naturally, in this type of systems Coarse Wavelenght-Domain Multiplexing (CWDM) becomes attractive since it allows channel spacing of about 20 nm using uncooled optical signal emitter devices. However, for long-haul systems, spatial multiplexing is not cost efficient and dense WDM is a requirement. The key parameter used to describe these systems is the spectral efficiency defined as the ratio of per-channel bit rate to WDM spacing. It should also be mentioned that some authors consider the usage of different regions within a waveguide (for example, concentric rings in free space or a fiber) as an SDM implementation [5].

Currently Available Modulation Techniques

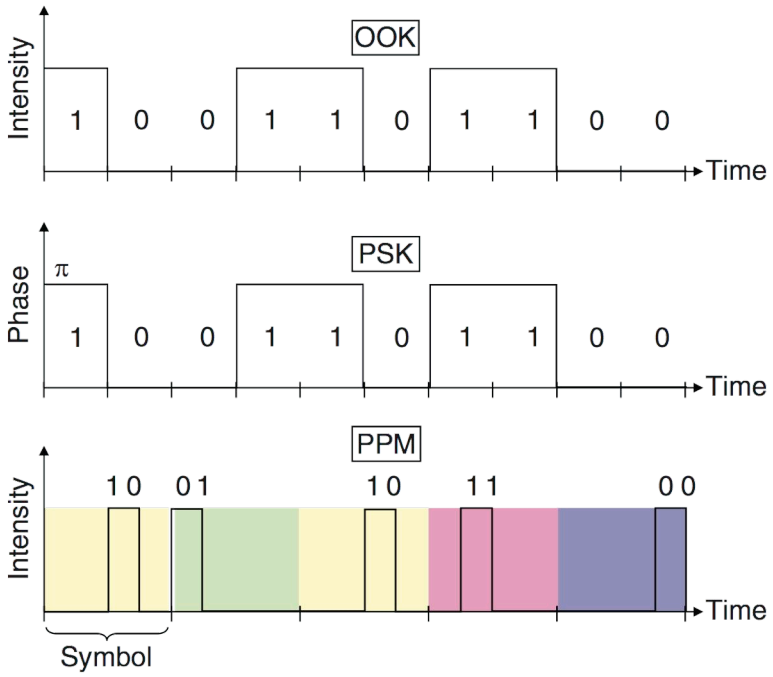

Winzer [5]

Figure 1.4: Diagram depicting OOK, PSK and PPM digital waveforms.

OOK & PPM

Uncoded On/Off Keying (OOK) in its various reincarnations has been used in optical communications for decades since it provides the simplest format in terms of hardware implementation and integration. As it should be evident through figure 1.4, OOK uses intensity as a criteria for encoding 0 and 1 using a certain time basis. Pulse-Position Modulation (PPM) is an orthogonal modulation technique where in addition to OOK basis of operation, other orthogonal dimensions are added to encode information. In the PPM depicted in image 1.4, the wavelength is added to provide an additional level of coding.

FSK, MSK & PolSK

In Frequency-Shift Keying (FSK), digital data can be encoded and transmitted through a carrier wave by shifting the carrier's frequency among a predefined set of frequencies. Minimum-Shift Keying (MSK) is a spectral efficient FSK where 0 and 1 differ by exactly one carrier period. As it is shown figure 1.4, using the

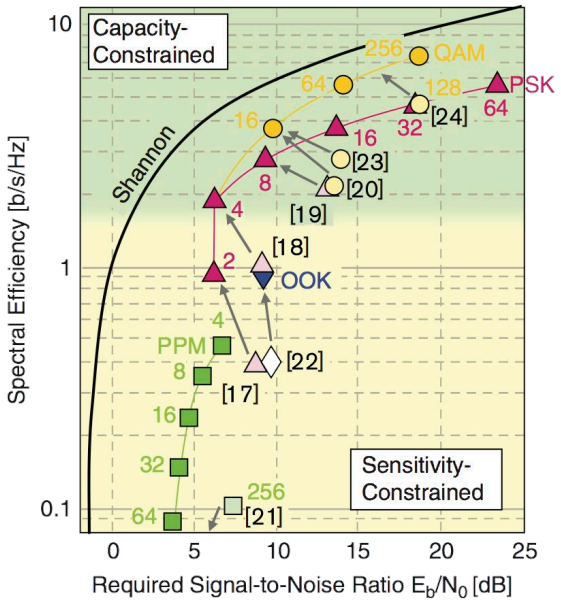

Winzer [5]

Figure 1.5: Spectral efficiency versus required SNR in various technology implementations compared to the theoretical limit predicted by Shannon's theory of information [4, 5]. Different optical communications technologies: [17–24].

same principle of FSK, in polarisation-Shift Keying (PolSK), data can be encoded and transmitted through a carrier wave by shifting polarisation [5].

Quadrature Amplitude & Phase Modulation

In the simplest of cases, two carrier waves, usually sinusoids, are out of phase with each other by 90° and are thus called quadrature carriers or quadrature components which gives the name to this method. Then, the modulated waves are summed and the resulting waveform is a combination of both Phase-Shift Keying (PSK) and Amplitude-Shift Keying (ASK) which uses the same principle but in regard to amplitude. Currently, this concept can be extended to other divisions of phase other than 90° resulting in n-PSK or n-Quadrature Amplitude Modulation (QAM) if amplitude is also used. Current state of the art relies heavily on Quadrature Phase-Shift Keying (QPSK) (although 8-PSK is also possible) and 16-QAM is also common. These modulation techniques are ideally represented in a constellation diagram, some of which can be checked in figure 1.1 [5].

Evolution & Tendencies

In information theory, Shannon's source coding theorem (or noiseless coding theorem) establishes the limits to possible data compression, and the operational meaning of the Shannon entropy. In the history of optical communications, Shannon theory has established a behaviour and ceiling to expected evolution regarding spectral efficiency and the required Signal To Noise Ratio (SNR) [4]. As it can be checked in the graphic in figure 1.5, Shannon's theory appears to provide a solid framework regarding the evolution of optical communications.

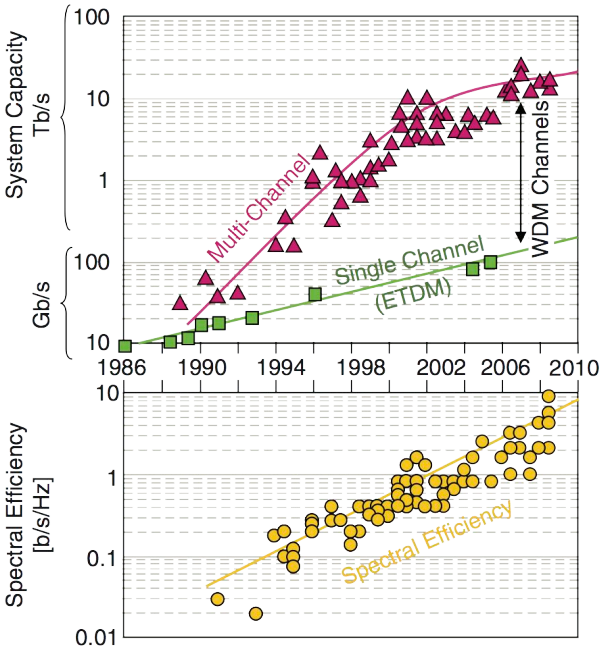

Winzer [5]

Figure 1.6: Evolution of WDM system capacity, ETDM bit rates and spectral efficiency in the age of modern optical communications.

On the other hand, as it can be easily checked in figure 1.5, despite an offset, current optical communication technologies appear to be evolving as expected, although it can also be inferred that saturation may be near [5]. Adding to the fact that WDM capacity gains appear to be slowly diminishing while the number of WDM channels appears to be stagnant if imposing faster ETDM bit rates (see graphic in figure 1.6), new degrees of freedom must be found and exploited if improved capacities are expected.

It is in this regard that the OAM may provide a substantial improvement over existing technologies. As it is shown in the graphic in figure 1.5, OAM may greatly reduce the current offset from which current technologies are, relatively to Shannon's curve, catapulting optical communications to their expectable limits within information theory.

At the time of the finishing of this thesis, a comprehensive overview of OAM in optical communications was published by Willner et al. [25] providing an invaluable source of information compiling several studies that were the basis for our work among others.

Orbital Angular Momentum

A light beam can be described as a stream of photons. Each photon has an energy $\hbar\omega$, a linear momentum $\hbar k$, directed along the axis perpendicular to the wavefronts and a *spin* angular momentum (SAM) of $\hbar$ parallel or anti-parallel to the direction of propagation [26]. Less widely known is that light beams can also carry an *orbital angular momentum* (OAM) with no relation to polarisation and therefore also to photon spin [27]. This difference shall be further made explict on through appropriate concept and calculation descriptions.

The energy flux in any light beam is conveyed by the Poynting vector, which may be calculated from the vector product of the electric and magnetic fields [28]. In vacuum or any isotropic material, this vector is always parallel to the wavevector and perpendicular to the wavefront of the beam[28]. In its most usual form as it is presented in figure 1.7a, the wavefronts of laser light are approximately planar and therefore the wavevector and the linear momentum of the photons is directed along the beam axis in the propagation direction. The field distributions associated with such beams are paraxial solutions to the wave equation providing the most common and simple approach, although it is not the only one [27, 29].

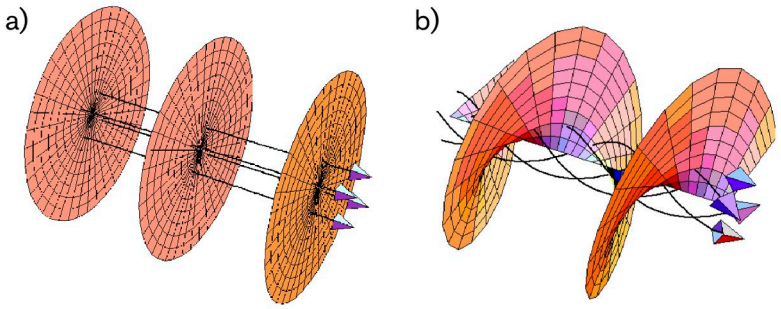

Padgett and Allen [27]

Figure 1.7: Comparison between planar and spiraled wavefronts and respective Poyinting vector for $l = 0$ in a) and $l = 1$ in b).

Among others, the Laguerre-Gaussian beams, which have l intertwined helical wavefronts as shown in figure 1.7b are also valid solutions to the paraxial wave equation [30]. As a subfamily of the greater family of Hermite-Gaussian beams, the Laguerre-Gaussian beams are obtained by solving the paraxial wave equation in cylindrical coordinates r, ϕ, z and are described by equation given by result 1, where z_R is the Rayleigh range, w is the waist of the beam, k is the wavevector, $p+1$ is the number of annular regions, l is the number of intertwined helices and C is a normalization constant [30].

Result 1 (Laguerre-Gaussian Beam Modes)**.**

$$U_{pl}(r,\varphi,z) = \frac{C_{lp}^{LG}}{\left(1+z^2/z_R^2\right)^{1/2}}\left(\frac{r\sqrt{2}}{w(z)}\right)^{l} L_p^l\left(\frac{2r^2}{w^2(z)}\right)\exp\left[\frac{-r^2}{w^2(z)} - \frac{ikr^2 z}{2\left(z^2+z_R^2\right)}\right] \times \exp\left[i(2p+l+1)\arctan\left(\frac{z}{z_R}\right)\right]\exp(-il\varphi) \tag{1.1}$$

Although rather difficult to visualize,the geometry of the wavefront of these beams is perhaps familiar to some of us, resembling *fusilli* when $l = 3$, as presented in figure 1.8 [31]. More importantly, these helical wavefronts will result in a Poyinting vector and a wavevector that spiral around the beam axis [32] which

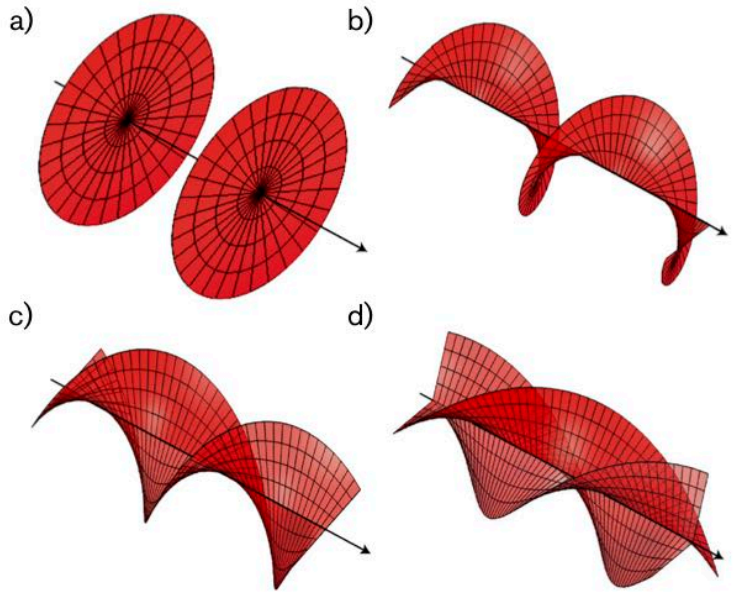

Yao and Padgett [31]

Figure 1.8: Helical wavefronts for $l = 0$ in a), $l = 1$ in b), $l = 2$ in c) and $l = 3$ in d).

means that the momentum of each photon has an non-zero azimuthal component from which the angular momentum will mainly depend [31]. The angular momentum density $\mathbf{M}$ is given by equation 1.2 whereas $\mathbf{J}$ will be the total angular momentum of the beam while the total angular momentum $\mathbf{J}$ be defined as the sum of the orbital component $\mathbf{L}$ and spin component $\mathbf{S}$. [33].

$$\mathbf{M} = \varepsilon_0 \mathbf{r} \times (\mathbf{E} \times \mathbf{B}) \tag{1.2}$$

$$\mathbf{J} = \varepsilon_0 \int \mathbf{r} \times (\mathbf{E} \times \mathbf{B})\, d\mathbf{r} \tag{1.3}$$

$$\mathbf{J} = \mathbf{L} + \mathbf{S} \tag{1.4}$$

Defining the local angular momentum as described by equation 1.2, applying it to the Laguerre-Gaussian distribution in linearly polarised beams ($\sigma = 0$ and therefore $\mathbf{S} = 0$) one obtains the following equation [30]:

$$\mathbf{M} = -|u|^2 \left[\frac{l}{\omega} \frac{z}{r} \mathbf{r} - \frac{r}{c} \left[\frac{z^2}{z^2 + z_R^2} - 1 \right] \boldsymbol{\phi} - \frac{l}{\omega} \mathbf{z} \right] \tag{1.5}$$

If integrated according to equation 1.3, the r and ϕ components disappear, since the radial and azimuthal components are symmetric about the axis, leaving only the z component [30]. Therefore, disregarding these components in 1.2 one promptly obtains the equation 1.6.

$$M_z = \varepsilon_0 \mathbf{r} \times (\mathbf{E} \times \mathbf{B})_\phi = \frac{l}{\omega} |u|^2 \tag{1.6}$$

The linear momentum density per unit power for linearly polarised Laguerre-Gaussian beams is given by equation 1.7 [30].

$$\mathscr{P} = \frac{|u|^2}{c} \left[\frac{rz}{\left(z^2 + z_R^2\right)} \mathbf{r} + \frac{l}{kr} \boldsymbol{\phi} + \mathbf{z} \right] \tag{1.7}$$

If one divides M_z by the z component of the linear momentum density per unit power in equation 1.7, l/ω is obtained [30]. The same result is obtained using the integrated physical quantities [34]. Imposing a single photon energy given by equation 1.9, one readily obtains $l\hbar$ for the orbital angular momentum of a photon.

$$\frac{M_z}{\mathscr{P}_z c} = \frac{J_z}{P_z c} = \frac{l}{\omega} \tag{1.8}$$

$$E = \hbar\omega \tag{1.9}$$

For non-linearly polarised Laguerre-Gaussian beams, an additional component appears in 1.6 becoming 1.10[30]. This additional term is related to spin angular momentum.

$$M_z = \frac{l}{\omega}|u|^2 + \frac{\sigma_z \rho}{2\omega}\frac{\partial |u|^2}{\partial r} \tag{1.10}$$

Although the paraxial approximation is sufficient to describe OAM in many applications, the separation of the spin and orbital components of the angular momentum has been derived for non-paraxial beams from the Maxwell's equations [35].

It should also be noted that, despite this rather rough approach to determine OAM per photon, OAM has been measured at the single photon level in 2001 [13].

Historical evolution

It is well known from Maxwell's theory that electromagnetic radiation carries both energy and momentum which can have both linear and angular contributions [26]. The latter has a spin part associated with polarisation and an orbital one related to spatial distribution [33]. Despite the first experimental demonstrations of the mechanical torque created by the transfer of angular momentum performed about 70 years ago [26], until rather recently, most of the work done within this subject has been related to linear momentum [30].

In 1936 Beth [26], through the interaction between polarised light and the rotational motion of a birefringent wave plate suspended by a fine quartz fiber, Beth was able to perform the first observation of the angular momentum of light. He followed the work proposed by Poynting in 1909 [36], who first reasoned that any transformation of the polarisation state, say, from linear to circular, must be accompanied by an angular momentum exchange with the optical system [31]. Beth was able to show that the ratio of angular to linear momentum should be equal to $\lambda/2\pi$ and therefore that an angular to energy ratio of $\pm\hbar$ should be related to spin angular momentum (SAM) [26].

It was only in 1992 that Allen et al. [30] realized that all hellically-phased beams carry an OAM equal to $l\hbar$ per photon, and perhaps even more surprising and in addition, OAM comes in units of $\hbar$ which can be shown through a geometric argument [31, 32, 37] but also more formally from Maxwell's equations [35] by imposing quantization *a posteriori* [31]. However, the keypoint of this breakthrough in the context of this article is that OAM constitutes a natural property of all helically phased beams, and hence can be readily generated in a standard optics laboratory [30].

From this point forward, from the possibility of easily generating OAM carrying beams, arose the idea of using it as new degree of freedom in optical communications systems [38, 39].

State of the Art

OAM Generation

In the scope of optical communications systems, the available methods to generate OAM carrying beams are of great importance. In order to be able to explore OAM as a new degree of freedom in optical communication systems, dynamic signal generation and control are required to conceive such systems. Therefore, in this section, current generation technologies will be reviewed.

Refractive optical elements

In 1936, Beth [26] used passive refractive optic elements to generate OAM carrying beams as proposed by Poynting [36]. Again, following the theoretical work by Abramochkin and Volostnikov [40] which predicted the mode conversion of Hermite-Gaussian (HG) modes to Laguerre-Gaussian (LG) modes through certain astigmatic transformations, in 1992 Allen et al. [30] were able to assemble an apparatus of specifically designed cylindrical lenses. They successfully converted laser HG modes to LG modes and confirmed experimentally that LG modes laser beams carry OAM, as described in the previous section. Here, the production of LG modes is based on the fact that an HG mode at 45 degrees can be decomposed into a set of HG modes, which when rephased and recombined result in a certain LG mode as presented in figure 1.9.

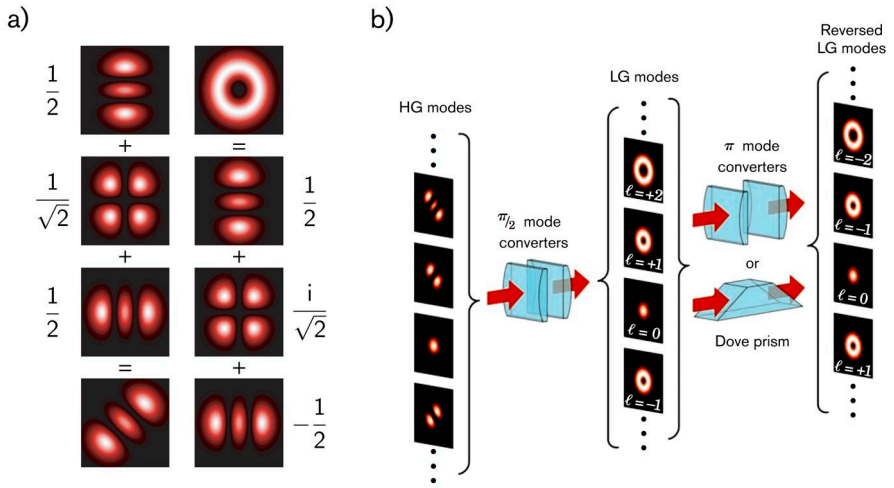

Yao and Padgett [31]

Figure 1.9: a) Combining Hermite – Gaussian modes to produce Laguerre – Gaussian modes: $\frac{-1}{2}HG_{02} + \frac{i}{\sqrt{2}}HG_{11} + \frac{1}{2}HG_{20} = LG_{02}$; b) $\pi/2$ and π converters.

These lenses come mainly in two main forms: the $\pi/2$ converter changes any incident HG mode of indices m,n into an LG mode of indices $l = m - n$ and $p = min(m,n)$ and the π, which transform any mode into its mirror image and are optically equivalent to a Dove prism[41].

However, keeping close to the mechanical analogy proposed by Poyinting, the method of generating OAM carrying beams through spiral phase plates proves itself very useful and pertinent to understanding the most basic physical nature of OAM.

The optical thickness of the element increases with the azimuthal position according to $l\lambda\theta/2\pi(n-1)$. In optical wavelengths, this approach requires extreme precision in the pitch of the helical surface. In the first demonstrations, a spiral phase plate with a much larger physical step was immersed in an index-matched fluid bath, the temperature of which could be controlled to obtain precisely the required refraction index mismatch to tune the step height to the operating wavelength.[31]

This method illustrates the mechanical analogy proposed by Poyinting. The resulting helically phased beam is 'carved' from the plane phased beam through the transfer of momentum from the optical element to the beam itself.

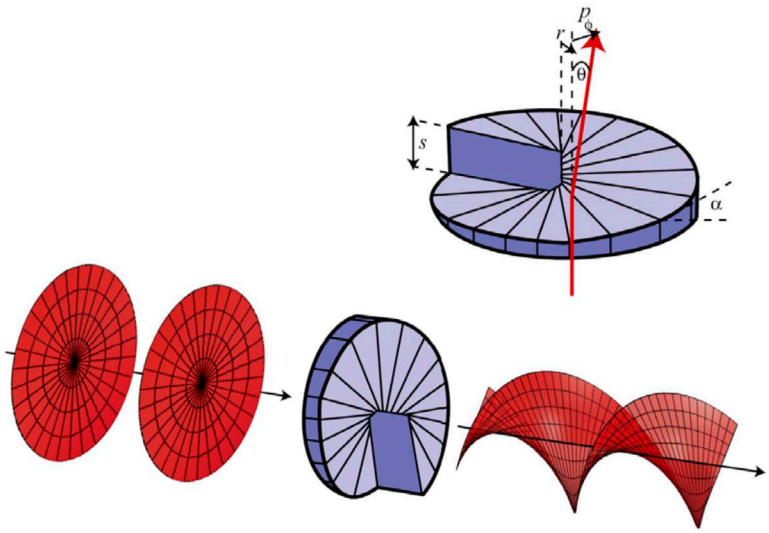

Yao and Padgett [31]

Figure 1.10: A spiral phase plate can generate a helically phased beam from a Gaussian. In this case $l = 0$ to $l = 1$.

In the case of normal incidence to the phase plate shown in figure 1.10, at the exit the ray is refracted in the azimuthal direction. Therefore, the linear momentum acquires an azimuthal component when expressed to a radius vector results in an angular momentum along the beam axis [31].

Regarding coherence, perhaps it should be expected that OAM would require coherence of phase along the beam. However, illuminating a spiral plate with a incoherent source results in a beam which can be divided into various annular regions. The azimuthal and momentum flow per photon has an average value proportional to the radius [42]. This establishes a relation between the angle of incidence and the obtained ring radii as it is presented in figure 1.11. Note that due to interference phenomena, the zero or non-zero on-axis intensity is a possible indication of spatial coherence [31].

Although crucial for the development of OAM experiments and research, optical elements aren't the prime choice for most OAM optical communications research, since they are passive and don't allow a true dynamic signal generation, as opposed to more contemporary methods.

Computer generated holograms

As an alternative to complex refractive optics, computer generated holography produces readily designed diffractive optic elements which mimic any refractive element of choice. In concept, a helical phase distribution

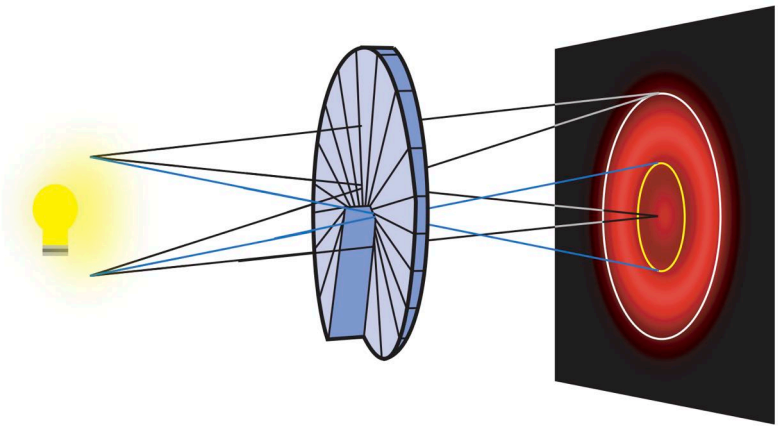

Swartzlander Jr and Hernandez-Aranda [42]

Figure 1.11: Uncoherent source causes casts light on axis singularity through interference.

applied to $\exp(il\phi)$ a Gaussian beam converts it into a desired helical beam. Combining this profile and a linear phase ramp, a forked diffraction grating is obtained, as shown in figures 1.12 and 1.13. The same effect can be produced through spiral Fresnel lenses [31].

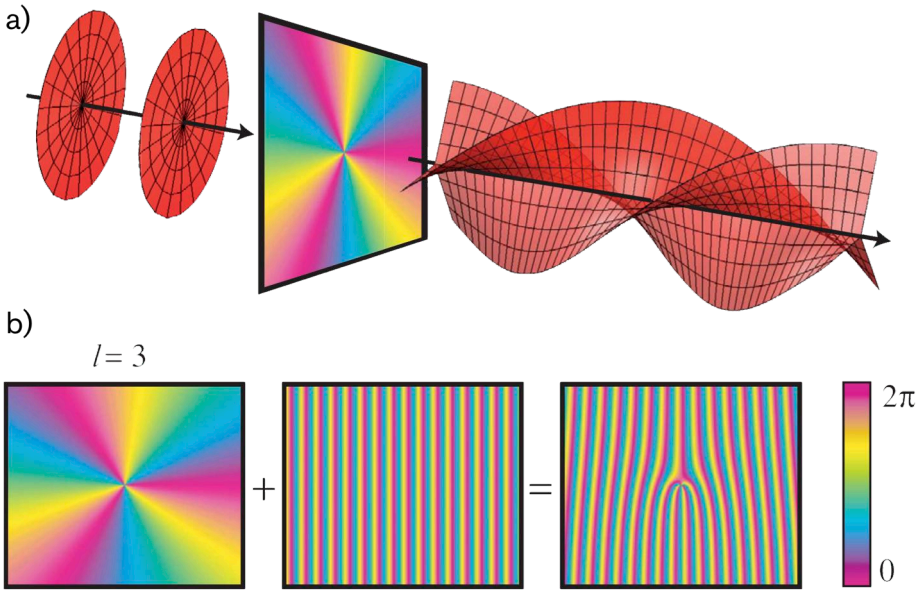

Yao and Padgett [31]

Figure 1.12: Conceptual conversion from a Gaussian to a helical wavefront through application of a helical phase distribution for $l = 3$: a) spiral phase pattern OAM generation; b) forked diffraction pattern.

Despite being the prime choice for most applications nowadays due to its cost, availability and wide range of specifications, the passive nature of these elements still make them unsuitable for optical signal generation.

However, what really makes computer generated holography appealing regarding OAM in optical communications is that the same computational methods used to generate specific diffraction gratings can be applied to signal generation in SLMs which are widely commercially available.

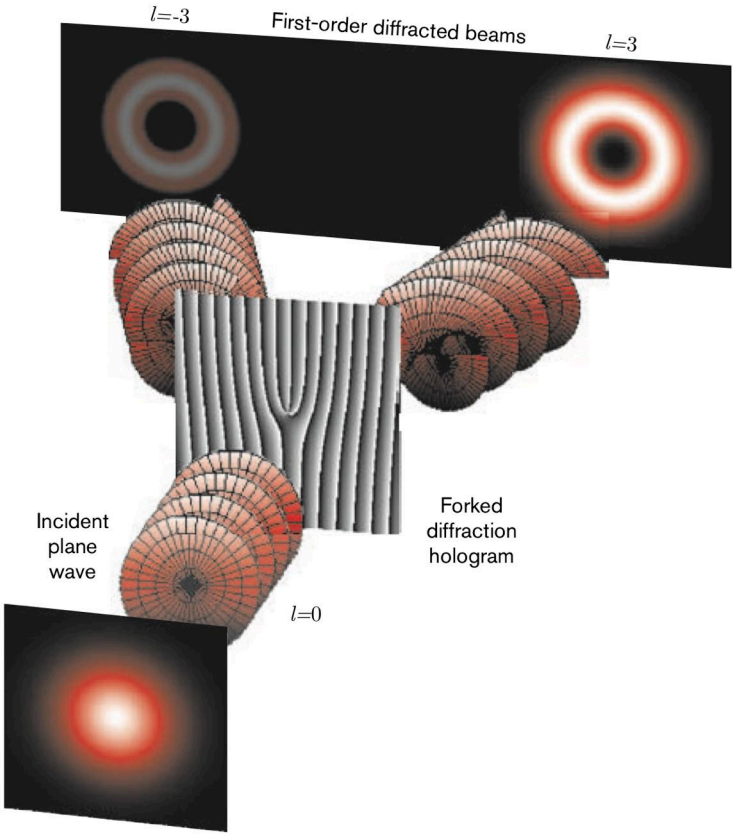

Courtial [43]

Figure 1.13: Conversion from a $l = 0$ Gaussian to a $l = \pm 3$ helical wavefront through application of forked diffraction grating for $l = 3$. Note the conservation of OAM in the conversion from $l = 0$ to $l = 3$ & $l = -3$.

Spatial light modulators (SLMs)

Spatial Light Modulators (SLMs) are pixellated liquid crystal devices that can be programmed through the video interface of a computer to act as holograms, which makes changing their design as easy as changing the image displayed by the computer interfacing the SLM. This is why computer generated holography is interesting to OAM communication systems: the computational methods used in the latter may be implemented in the former, opening the possibility for true dynamic OAM optical signals generation [44].

Accurate holograms are the complex far-field diffraction patterns of the desired beams which are defined in terms of both intensity and phase. When a helical beam is generated as presented in the figure 1.12, the transmitted beam is a superposition of LG modes with all the same l index predominantly with $p = 0$ [31].

However small, since p has a non-zero contribution, precise control over it is needed requiring the hologram to define both the phase and the intensity of the diffracted light. Unfortunately, SLMs are designed to modify only one or the other [31]. However several approaches exist and others are being developed to overcome these issues making SLMs the current *defacto* choice in optical signal generation for OAM related studies in optical communication systems as it is easily shown by the array of experimental studies available to this day.

Regarding coherence, SLMs work like forked diffraction gratings. They are able to deal with the relatively broad bandwidth optical signals. The grating introduces an angular dispersion through the various spectral

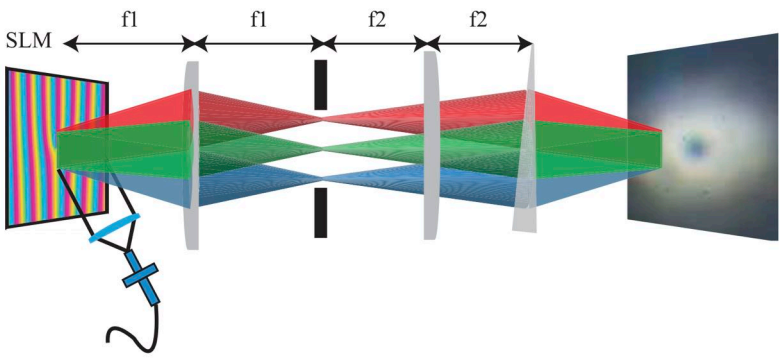

Leach and Padgett [45]

Figure 1.14: Illumination of a forked diffraction grating with a broad spectral bandwidth source.

components which will allow to separate the multiple wavelength bins in an optical signal as shown in figure 1.14 [45]. This is of possible importance since it may allow the combination of WDM with OAM multiplexing.

Optical Communications Applications

In recent years, OAM has found interest regarding optical communication systems in both optic fibers and free space applications (see on appendice A, table A.1). Despite still being a vanguard subject, the most relevant applications (see on appendice A, table A.1) in recent years have relied mainly on commercially available components and fibers [46–49], although also some new approaches based on yet to be available equipment are being developed [50–54].

Optic Fibers

Regarding fibers, current state of the art has recently achieved 1.6 terabit per second single core fiber capacity through OAM-WDM and specific fiber design [46]. Data transmission was successful through more than 1 km long maintaining bit error rate (BER) below the forward error correction (FEC) limit. In the same experiment, a OAM-PDM configuration allowed data transmission for also more than 1 km with a capacity of 400 gigabit per second. Detailed information available in the work by Bozinovic et al. [46] and the table A.1 on appendice A.

Free Space

Since OAM modes are more stable in free space, better results regarding aggregated capacity are usually the norm. However, as it can be expected, the research on these systems is still performed deeply in laboratory conditions with some disregard to distance [48, 49]. Nevertheless, the results regarding capacity are impressive and the state of the art appears to reach 0.1 Pbit/s aggregate capacity using 24 OAM modes across 42 wavelengths.

Quantum Communications & Security

Another interesting application regarding OAM is in quantum communications and security. A quantum protocol known as ‘quantum coin tossing’ [13, 55] was implemented, where two parties share codified

information (the result of a coin toss) that can be retrieved by a posteriori manipulations, but cannot be deciphered before a determined unveiling time, thus allowing the toss to be secret until the parties have bet on the result. In this particular protocol, OAM allows the use of qutrits (quantum states in three dimensions) offering an advantage over classical communication, and also over two-dimensional quantum systems. This kind of protocol is of most of interest for applications where two partners wish to undertake a secure transaction, but do not fully trust each other.

Conclusions

OAM has the potential to greatly improve aggregate system capacity through the offering of possibly a *unlimited* number of l modes. The current limitations regarding the inherent instability of these modes while combining them with established technologies such as WDM and PDM , if overcome, may allow OAM to be the next workhorse for optical communication systems in a world with ever-growing need for more aggregate capacity than ever and where more than ever, photonics technology imposes itself as the future communications.

Additionally, OAM is being researched for countless other applications outside the scope of optical communication systems and is establishing itself in several areas raging from quantum physics, quantum computation to nanotechnologies and biophysics[31]. This engorges the importance of the study of these phenomenon and its value for future technologies and knowledge.

2

Theoretical Background

Contents

Theoretical Context

In a first phase, we will provide the physics theoretical basis of our work in a practical approach which will allow us to run some simulations which will mirror the experiments we wish to perform. Essentially, this basis will be presented in a condensed need-to-know approach consisting of some special topics within the broader area of Fourier Optics. Basically we shall establish the necessary foundations of the Scalar Diffraction Theory starting from the Maxwell's equations and the Huygens-Fresnel Principle. From there we will present the Angular-Spectrum Propagation Method which will enable us to derive the Fresnel Diffraction Integral and interpret it at the light of Fourier optics. The references used for this context are the books by Goodman and Gustafson [56] and Lauterborn et al. [57].

In order to proceed with our study, it is rather important to offer a theoretical framework to contextualize the nature our work. We shall start by providing a brief derivation of relevant Gaussian beam modes solutions. This mathematical description will enable us to predict some special properties which will be further addressed, associated with the main topic of our interest, OAM carrying beams. The references used for this context are the books by Saleh and Teich [58] for the fundamental Gaussian beam and Lakshmi Narayanan et al. [59] for the Laguerre-Gaussian higher order modes.

Finally, given this context we will then be able to justify the comprehensive scope of applications we wish to explore in the regard of optical communications.

Fourier Optics

The Fourier transform plays a transversal role in science and technology. Its applications are numerous, but perhaps the most immediate, it is deeply related to communications, namely in the area of signal processing and transmission where the the one-dimensional Fourier transform $\mathscr{F}$ allows for instance, the connection between a time signal $f(t)$ with its complex spectral function $\widetilde{f}(\nu)$ which provides information about its frequency:

$$\widetilde{f}(\nu) = \mathscr{F}[f(t)](\nu) = \int_{-\infty}^{+\infty} f(t) \exp(-2\pi i \nu t)\, dt \tag{2.1}$$

In a rather bold way, the main strength of the Fourier signal analysis is that it allows us to interpret an apparently complicated signal as a superposition of elementary sinusoidal signals as used in TDM for instance. Through this property we are then able to combine different signals to encode information for instance, transmit them through a single channel and rebuild the original signals afterwards.

In Fourier optics, we will be concerned about the two-dimensional Fourier transform shown in equation 2.2 which will allow us to treat the challenges of optics through a similar approach.

$$\widetilde{U}(\nu_X, \nu_Y) = \mathscr{F}[U(x,y)](\nu_X, \nu_Y) = \iint_{-\infty}^{+\infty} U(x,y) \exp[-2\pi i (\nu_X x + \nu_Y y)]\, dxdy \tag{2.2}$$

By assuming the complex field distribution of a monochromatic wave as Fourier-analyzed across any plane, then the various spatial Fourier components can be identified as plane waves traveling in different directions away from that plane. As for the field amplitude at any other point (or across any other parallel plane), it can be calculated by adding the contributions of these plane waves, taking due account of the phase shifts they

have undergone during propagation. These considerations are expressed in more detail when we approach the Angular Spectrum Propagation Method.

Scalar Wave Equation

The most fundamental beginning of our theory resides in the Maxwell's equations:

$$\nabla \times \mathbf{E} = -\mu \frac{\partial \mathbf{H}}{\partial t} \tag{2.3}$$

$$\nabla \times \mathbf{H} = \varepsilon \frac{\partial \mathbf{E}}{\partial t} \tag{2.4}$$

$$\nabla \cdot \varepsilon \mathbf{E} = 0 \tag{2.5}$$

$$\nabla \cdot \mu \mathbf{H} = 0 \tag{2.6}$$

Since we are working in free space, it is safe to assume a linear, isotropic, homogeneous and non-dispersive medium. By applying the following operator in both sides of the the first equation of Maxwell,

$$\nabla \times (\nabla \times \mathbf{E}) = \nabla (\nabla \cdot \mathbf{E}) - \nabla^2 \mathbf{E} \implies \nabla^2 \mathbf{E} - \frac{n^2}{c^2} \frac{\partial^2 \mathbf{E}}{\partial t^2} = 0 \tag{2.7}$$

since the vector wave equation is obeyed by both $\mathbf{E}$ and $\mathbf{H}$, an identical equation is obeyed by all components of those vectors. Therefore, its behaviour can be summarised through a single scalar wave equation where $\psi(x,y,z,t)$ represents any of the scalar field components dependent both on position and time.

$$\nabla^2 \psi(x,y,z,t) - \frac{n^2}{c^2} \frac{\partial^2 \psi(x,y,z,t)}{\partial t^2} = 0 \tag{2.8}$$

It should be noticed that this approach is valid within the restrictions we imposed over its derivation. If more exotic situations were considered, coupling effects derived from the Maxwell equations would arise and would need to be dealt with accordingly.

As final remark, by describing a monochromatic wave through its phasor, which is reasonable since we are not interested in describing our wave over time, but solely over position, and if we perform the method of separation of variables regarding time and space over the scalar wave equation 2.8, we obtain the Helmholtz equation we used previously.

Result 2 (Helmholtz Equation)**.**

$$\left(\nabla^2 + k^2\right) U = 0 \tag{2.9}$$

Huygens-Fresnel Principle

As it has been established in the previous section, in our conditions the propagation problem becomes solely a diffraction problem which provides a good starting point in this section. Sommerfeld first coined the term diffraction as any deviation of light rays from rectilinear paths which cannot be interpreted as reflection or refraction. This rather elusive definition reflects the somewhat complicated history of diffraction in physics. Christian Huygens established intuitively that by considering each point on the wavefront to be a new source of a secondary spherical disturbance, then the original wavefront could be found by constructing the envelope of the secondary wavelets as it is shown in 2.1. About one hundred years later, Thomas Young introduced the concept of interference which predicted that under proper conditions, light could be added to light to

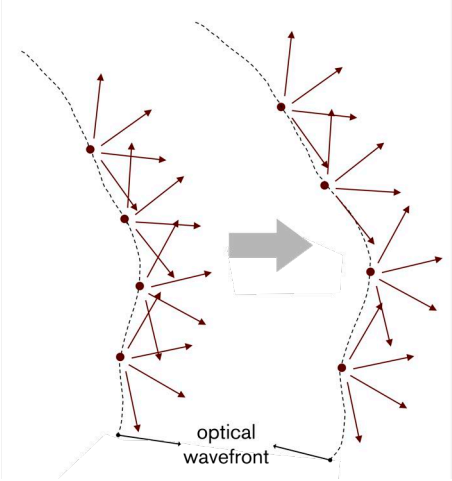

Figure 2.1: Huygens' envelope construction.

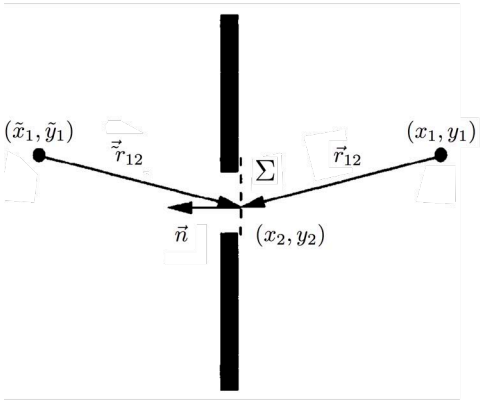

Goodman and Gustafson [56]

Figure 2.2: Rayleigh-Sommerfeld formulation of diffraction by a plane screen.

produce darkness. Finally, about ten years later Fresnel was able to merge both concepts by allowing the various wavelets to mutually interfere. In spite of some rather arbitrary assumptions about the amplitudes and phases of Huygens' secondary sources, he successfully calculated the distribution of light in diffraction patterns with excellent precision. This successful albeit approximate interpretation and its successful results and predictions established the basis from which more sophisticated approaches emerged.

The Rayleigh-Sommerfeld diffraction formula mathematically describes the Huygens-Fresnel Principle, as accompanied by figure 2.2 through the integral 2.10.

Result 3 (Rayleigh-Sommerfeld Diffraction)**.**

$$U(x_1, y_1) = \frac{1}{i\lambda} \iint_{\Sigma} U(x_2, y_2) \frac{\exp(ikr_{12})}{r_{12}} \cos\theta ds \tag{2.10}$$

This integral, which gives us the observed field at position (x_1, y_1), may be interpreted as a superposition of diverging spherical waves $\exp(ikr_{12})/r_{12}$ originated from secondary sources located at each and every point (x_2, y_2) within the aperture Σ.

The Angular Spectrum Propagation Method

Assuming the considerations referred in the beginning of this section, by taking the equation 2.2, we can write a complicated field U as a decomposition of simpler complex-exponential functions as shown in 2.11.

$$U(x, y, 0) = \int_{-\infty}^{+\infty} \widetilde{U}(\nu_X, \nu_Y, 0) \exp[i2\pi(\nu_X x + \nu_Y y)] d\nu_X d\nu_Y \tag{2.11}$$

In order to provide some physical meaning insight about the former equation, by writing the time independent phasor of the plane wave as shown in equation 2.12, it becomes clear that the complex exponential in equation 2.12 may be interpreted as a plane wave across the plane $z = 0$ propagating with the direction cosines defined in the relations 2.13.

$$\exp\left(i\vec{k} \cdot \vec{r}\right) = \exp i\frac{2\pi}{\lambda}(\alpha x + \beta y) \exp i\frac{2\pi}{\lambda}\gamma z \tag{2.12}$$

$$\alpha = \lambda \nu_X \qquad \beta = \lambda \nu_Y \qquad \gamma = \sqrt{1-\alpha^2-\beta^2} \tag{2.13}$$

For this reason, the function 2.14 is called the angular spectrum of the disturbance $U(x,y,0)$.

$$\widetilde{U}\left(\frac{\alpha}{\lambda},\frac{\beta}{\lambda},0\right) = \iint_{\infty}^{+\infty} U(x,y,0)\exp\left[-i2\pi\left(\frac{\alpha}{\lambda}x+\frac{\beta}{\lambda}y\right)\right]dxdy \tag{2.14}$$

Since the technicalities associated with the analytical treatment of the Angular Spectrum Propagation Method are outside our scope of work, it suffices to state that a relationship is found between $U(x,y,0)$ and $U(x,y,z)$ holding these concepts true while satisfying the Helmholtz equation resulting in the following equation.

Result 4 (Angular Spectrum Propagation)**.**

$$\begin{aligned} U(x,y,z) = \iint_{\infty}^{+\infty} \widetilde{U}\left(\frac{\alpha}{\lambda},\frac{\beta}{\lambda},0\right)\exp\left[i\frac{2\pi z}{\lambda}\sqrt{1-\alpha^2-\beta^2}\right] \\ \times \operatorname{circ}\left(\sqrt{\alpha^2+\beta^2}\right)\exp\left[i2\pi\left(\frac{\alpha}{\lambda}x+\frac{\beta}{\lambda}y\right)\right]d\frac{\alpha}{\lambda}d\frac{\beta}{\lambda} \end{aligned} \tag{2.15}$$

Unfortunately, this equation is inappropriate for computational purposes, however it can be approximated by two different methods: Fraunhofer approximation for far-field and Fresnel approximation for near-field. Regarding the dimensions expected in this study, we will be addressing the latter approach.

Regarding the choice of Fresnel regime, since both the calculation of the Rayleigh range (since OAM carrying beams are partially Gaussian in nature) and the Fresnel number weren't entirely clear since it's hard to know where exactly (due to the symmetry of the spiral phase patterns, the diffractive phenomenon occurs, and the grid size of the SLM is simply a too demanding criterion, an implementation of the Shannon-Whittaker sampling theorem available in [60] was used. This calculation is implemented in the simulation. Then, simulations were made using spiral phase Computer Generated Holograms (CGHs) for both regimes. The results were in fact quite similar despite a scale difference but Fresnel regime provided more accurate predictions of what we saw in the laboratory even when above the used implementation of the Shannon-Whittaker sampling theorem. Additionally, one of the most important work regarding this subject choose the Fresnel regime [48]. For reference, propagation distances of OAM beams in our experiment don't exceed 50 cm.

Fresnel Diffraction Approximation

Recalling the Huygens-Fresnel principle stated in equation 2.10, it can be re-written in rectangular coordinates in equation 2.16.

$$U(x_2,y_2) = \frac{z}{i\lambda}\iint_{\Sigma} U(x_1,y_1)\frac{\exp(ikr)}{r}dx_1dy_1 \tag{2.16}$$

$$r = \sqrt{z^2+(x_2-x_1)^2+(y_2-y_1)^2} \tag{2.17}$$

By performing the binomial expansion of r, the following approximation may be obtained.

$$r = z\sqrt{1+\left(\frac{x_2-x_1}{z}\right)^2+\left(\frac{y_2-y_1}{z}\right)^2} \simeq z\left[1+\frac{1}{2}\left(\frac{x_2-x_1}{z}\right)^2+\frac{1}{2}\left(\frac{y_2-y_1}{z}\right)^2\right] \tag{2.18}$$

By injecting this approximation in the Sommerfeld shown in equation 2.10, one immediately obtains the Fresnel Diffraction Integral as shown in equation 2.19.

$$U^{out}(x_2,y_2) = \frac{\exp(ikz)}{i\lambda z}\iint_{-\infty}^{+\infty} U^{in}(x_1,y_1)\cdot\exp\left\{i\frac{k}{2z}\left[(x_2-x_1)^2+(y_2-y_1)^2\right]\right\}dx_1dy_1 \tag{2.19}$$

Equation 2.19 can be identified as the following convolution where the convolution kernel is the Fresnel Diffraction Impulse shown in equation 2.21.

Result 5 (Fresnel Diffraction Approximation)**.**

$$U^{out}(x_2,y_2) = \iint_{-\infty}^{+\infty} U^{in}(x_1,y_1)\cdot h(x_2-x_1,y_2-y_1)\,dx_1dy_1 = U^{in}(x_1,y_1) * h(x_1,y_1) \tag{2.20}$$

$$h(x_1,y_1) = \frac{\exp(ikz)}{i\lambda z}\exp\left[\frac{ik}{2z}\left(x_1^2+y_1^2\right)\right] \tag{2.21}$$

It should be noticed that from the perspective from the angular spectrum, the Fresnel approximation is accurate provided only small angles of diffraction are involved. For this reason it is often stated that the paraxial approximation and the Fresnel approximations are equivalent.

Beam Characterization

In order to build a solid framework for future usage, it is pertinent to provide a brief, yet solid mathematical foundation to our work. As it was shown in the first chapter, mathematical beam characterisation proved itself as the corner stone of the modern OAM experimental proof. Also, if omitted, later justifications pertaining our choices become hard to contextualize and justify. Therefore, the fundamental and higher order modes solutions of the paraxial wave equation in cylindrical coordinates shall be derived and discussed.

Concluded our mathematical optics foundation, some conclusions and choices shall be addressed.

The Fundamental Gaussian Beam Mode Solution in Cylindrical Coordinates

As it has been shown in the introduction, OAM has proved itself as a rather elusive physical property. The fundamental Gaussian beam mode is not enough to describe it, however before moving to higher order modes with that in mind, it is needed to establish the basic fundamental equation for this mode.

A single component, ψ, of an electromagnetic wave propagating in a uniform medium satisfies the Helmholtz equation 2 where k is the wave number.

Result 2 (Helmholtz Equation)**.**

$$\left(\nabla^2+k^2\right)U = 0 \tag{2.9}$$

Our approach is a simplified description of the propagation of electromagnetic waves, where by restricting the region over which there is initially a nonzero field we obtain a problem solely of diffraction.

Starting by using a quasi-plane wave approximation definition where we still assume mutual perpendicularity between the electric and magnetic fields and also with the propagation axis and given the context of our work, it is still reasonble to further simplify the problem by assuming a largely collimated beam of radiation

where propagation along a z axis is assured but allowing transverse albeit limited variations. These considerations along with the introduction of the *complex field amplitude* u[1], are reflected in the reduced form of the Helmholtz equation shown in 2.22.

$$\frac{\partial^2 u}{\partial x^2}+\frac{\partial^2 u}{\partial y^2}+\frac{\partial^2 u}{\partial z^2}-2ik\frac{\partial u}{\partial z}=0 \tag{2.22}$$

The *paraxial approximation* consists of assuming that the variation along the direction of propagation of the complex amplitude u will be small over a distance comparable to a wavelenght and also that the axial variation will be small compared to the radial variation. Both statements allow us to neglect the third term in equation 2.22 since the former implies that it is negligible compared to the fourth term while the latter implies it is small compared to the first two resulting in the *paraxial wave equation* shown in 2.23.

$$\frac{\partial^2 u}{\partial x^2}+\frac{\partial^2 u}{\partial y^2}-2ik\frac{\partial u}{\partial z}=0 \tag{2.23}$$

The paraxial wave equation can be solved in different coordinate systems. OAM is a property related to cylindrical symmetry patterns. In cylindrical coordinates, r represents the axial radius, z is the propagation axis, and φ is the polar angle where $u=u(z,r,\varphi)$.

$$\frac{\partial^2 u}{\partial r^2}+\frac{1}{r}\frac{\partial u}{\partial r}+\frac{1}{r}\frac{\partial^2 u}{\partial \varphi^2}-2ik\frac{\partial u}{\partial z}=0 \tag{2.24}$$

For now, axial symmetry shall be assumed, resulting in the independence of φ nullifying the third term in equation 2.24.

$$\frac{\partial^2 u}{\partial r^2}+\frac{1}{r}\frac{\partial u}{\partial r}-2ik\frac{\partial u}{\partial z}=0 \tag{2.25}$$

It is widely known that the simplest solution to this equation is given by equation 2.26 where A and ρ are two complex functions of z only, which remain to be determined.

$$u(r,z)=A(z)\exp\left[\frac{ikr^2}{2\rho(z)}\right] \tag{2.26}$$

By injecting the unknown terms in equation 2.25 we obtain equation 2.27.

$$-2ik\left(\frac{A}{\rho}+\frac{\partial A}{\partial z}\right)+\frac{k^2r^2A}{\rho^2}\left(\frac{\partial \rho}{\partial z}-1\right)=0 \tag{2.27}$$

Both terms are independent of each other so the method of separable variables can be used.

$$\frac{\partial \rho}{\partial z}=1 \qquad\qquad \frac{\partial A}{\partial z}=-\frac{A}{\rho} \tag{2.28}$$

Thus yielding the solution shown in equation 2.29, assuming z_0 as the source point along the z propagation axis.

$$\rho(z)=\rho(z_0)+(z-z_0) \implies \rho(z)=\rho(0)+z \tag{2.29}$$

ρ or the *complex beam parameter* can be separated, for practical reasons, in both real and imaginary parts as shown in equation 2.30.

$$\frac{1}{\rho}=\left(\frac{1}{\rho}\right)_r-i\left(\frac{1}{\rho}\right)_i \tag{2.30}$$

[1] By using a *quasi-plane wave* approximation, one can write $U(x,y,z)=u(x,y,z)\exp(-ikz)$ where the second term will reflect gaussian propagation along z. Through this expression, we introduce the complex field amplitude u where we are able to describe both amplitude through its real component and phase by using the imaginary component.

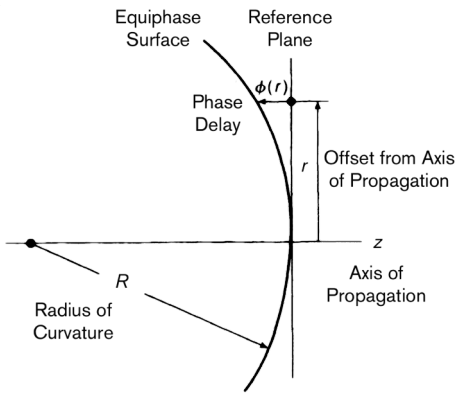

Figure 2.3: Spherical phase delay visual description.

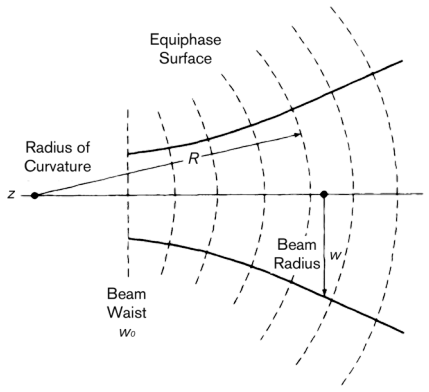

Figure 2.4: Gaussian beam parameter visual description.

Substituting in the equation 2.27, the exponential term becomes the equation 2.31.

$$\exp\left[-\frac{ikr^2}{2\rho}\right] = \exp\left[\left(\frac{-ikr^2}{2}\right)\left(\frac{1}{\rho}\right)_r - \left(\frac{kr^2}{2}\right)\left(\frac{1}{\rho}\right)_i\right] \tag{2.31}$$

Since the imaginary term expresses the phase shift, by assuming a spherical wave front in the paraxial limit one can define the equation 2.32[2] accordinggly with figure 2.3.

$$\phi(r) \simeq \frac{\pi r^2}{\lambda R} = \frac{kr^2}{2R} \tag{2.32}$$

Since ρ is a function of z and as one might expect, the radius of curvature of the beam will depend on the position along the axis of propagation.

By inspecting equations 2.31 and 2.32 , the relationship between the radius of curvature and the real part of of the complex beam parameter is established through the pair of equations 2.33.

$$\left(\frac{1}{\rho}\right)_r = \frac{1}{R} \qquad\qquad \rho = \frac{i\pi w_0^2}{\lambda} + z \tag{2.33}$$

Taking the general form for a Gaussian distribution along r given by 2.34

$$f(r) = f(0)\exp\left[-\left(\frac{r}{r_0}\right)^2\right] \tag{2.34}$$

then, the imaginary part of the complex beam parameter is obtained and can be written in relation to w_0 and z along with the rest of the beam parameters. The physical significance of these parameters is self-explanatory in figure 2.4.

Result 6 (Beam Parameters)**.**

$$R = z + \frac{1}{z}\left(\frac{\pi w_0^2}{\lambda}\right)^2 \tag{2.35}$$

$$w = w_0\sqrt{1 + \left(\frac{\lambda z}{\pi w_0^2}\right)^2} \tag{2.36}$$

$$z_R = \frac{\pi w_0^2}{\lambda} \tag{2.37}$$

[2]Given a certain ambiguity in terms and variables, it is important to notice that the phase-shift $\phi(r)$ should not be confused with the angular coordinate φ which shall be very important further on while describing the phase front geometry in order to predict OAM. PSK based modulation techniques make use of the phase-shift and not the phase front geometry (which is related to OAM).

By solving the second pair of equations obtained from the general solution, the final not normalized expression for $u(r,z)$ is obtained where ϕ_0 is the *Gaussian beam phase-shift*, z_R stands for *Rayleigh's range* and all the remaining variables and parameters were previously defined.

Result 7 (Fundamental Gaussian Beam)**.**

$$U(r,z) = u(r,z)\exp(-ikz) = \frac{w_0}{w}\exp\left[\frac{-r^2}{w^2} - i\frac{\pi r^2}{\lambda R} + i\arctan\left(\frac{z}{z_R}\right)\right]\exp(-ikz) \tag{2.38}$$

The plane wave phase factor $\exp(-ikz)$ should be noticed since it's imposed by the inspection of the general expression trough which the the complex field amplitude u is defined. Since we wish to describe non-plane phases, this approach is unsuited as a final result towards our objective.

The Higher Order Gaussian Beam Modes Solution in Cylindrical Coordinates

The Gaussian beam solutions of the paraxial wave equation may provide the simplest approach to describe the propagation of a quasi-collimated beam of radiation. While certainly the most important and widely used, they are not the only ones.

In order to be able to describe OAM carrying beams, the fundamental mode is not enough. The fundamental Gaussian mode equation promptly eliminates the azimuthal angle φ dependence.

Since in order to assess OAM, a non-plane phase front is needed and to obtain it, one simply can't eliminate the φ dependence as it was done previously, since this variable is deeply related to the phase front geometry in the axial planes.

From the general equation 2.26 the following *ansatz* may be presented in equation 2.39.

$$u(r,\varphi,z) = A(z)\exp\left[-\frac{ikr^2}{2\rho(z)}\right]S(r)\exp(il\varphi) \tag{2.39}$$

This expression is not innocent regarding our objective. A physically rather intuitive and mathematically sound way to describe a OAM carrying beam is by imposing an angular spiral phase expressed by $\exp(il\varphi)$ where l is an integer. This special phase is expected to provide the phase we seek. However, in order to maintain the validity of our solution while accommodating this phase structure restriction, an unknown radial function S must be introduced.

Since we wish to maintain the parameters already defined in the previous section to the fundamental Gaussian beam mode solution, the paraxial wave equation will reduce to a differential equation for S whose solutions are

$$S(r) = \left(\frac{\sqrt{2}r}{w}\right)^l L_p^l\left(\frac{2r^2}{w^2}\right) \tag{2.40}$$

where L_p^l is the generalized Laguerre polynomial where p is the angular index and l is the angular index and can be directly obtained from the expression 2.41.

$$L_p^l(x) = \frac{e^x u^{-l}}{p!}\frac{d^p}{dx^p}\left(e^{-x}x^{p+l}\right) \tag{2.41}$$

These polynomials are solutions to the Laguerre's differential equation. From this point, one is ready to compute the final form of the solution to obtain the Laguerre-Gaussian modes equation shown in equation 1.1 as they were presented in the previous chapter.

Result 1 (Laguerre-Gaussian Beam Modes)**.**

$$U_{pl}(r,\varphi,z) = \frac{C_{lp}^{LG}}{\left(1+z^2/z_R^2\right)^{1/2}} \left(\frac{r\sqrt{2}}{w(z)}\right)^l L_p^l\left(\frac{2r^2}{w^2(z)}\right) \exp\left[\frac{-r^2}{w^2(z)} - \frac{ikr^2 z}{2\left(z^2+z_R^2\right)}\right] \times \exp\left[i(2p+l+1)\arctan\left(\frac{z}{z_R}\right)\right] \exp(-il\varphi) \tag{1.1}$$

These modes provide a complete basis solution for the paraxial wave equation which we need to correctly explain the next section. In figure 2.5 several intensity plots are shown by using different values of p and l.

Historically, following the theoretical work by Abramochkin and Volostnikov [40] with LG mode conversion, Allen et al. [30] was able to experimentally obtain LG modes which carry OAM thus rekindling the modern age investigation in the subject.

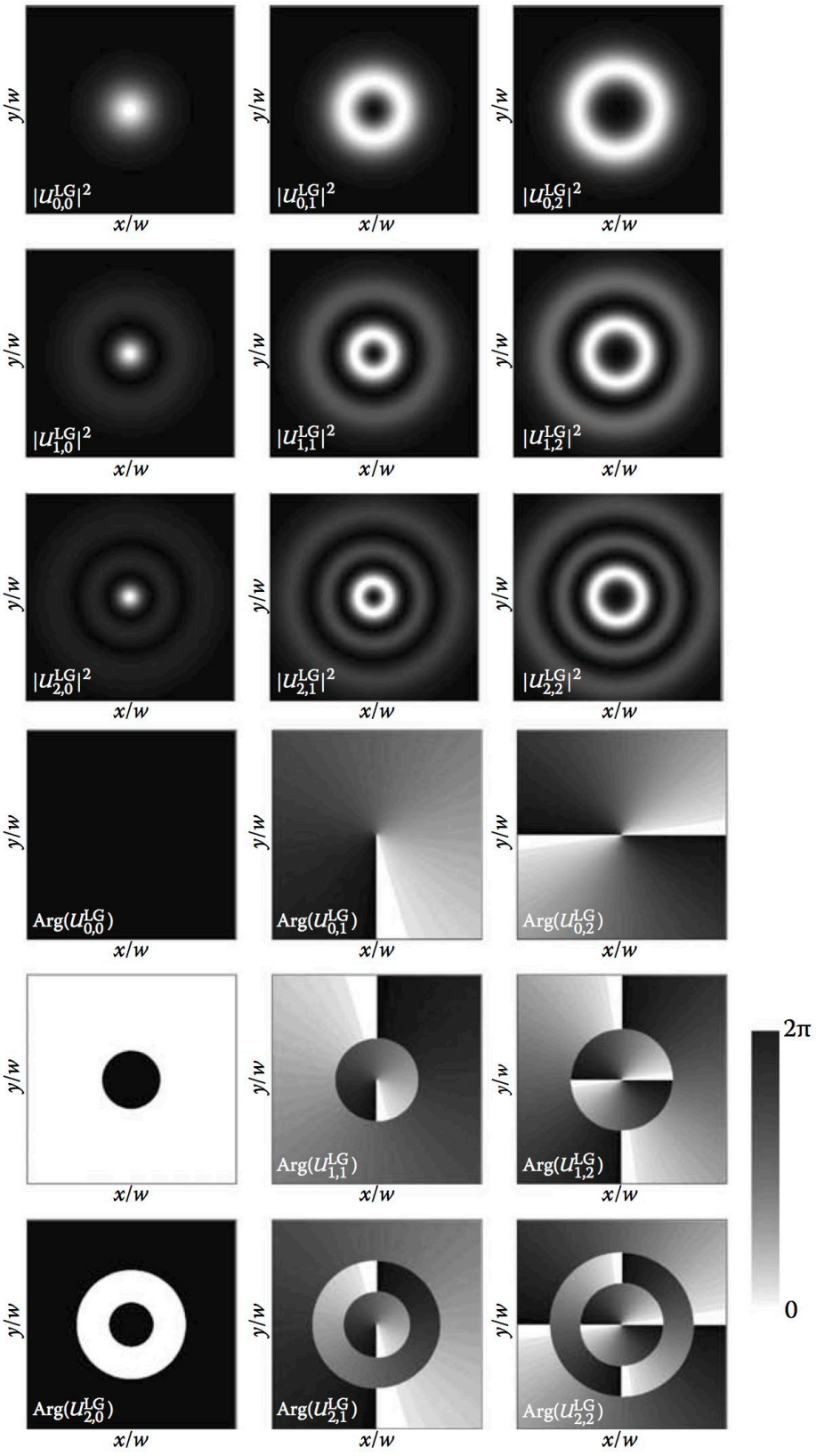

Lakshmi Narayanan et al. [59]

Figure 2.5: Cross sections of the irradiance $|U|^2$ and phase (at the waist plane) for LG beams with $l = 0, 1, 2$ and $p = 0, 1, 2$. Modes with negative m are identical in irradiance to those with positive p, and their phase is a mirror image with respect to the y-axis.

Practical Considerations

Now that the mathematical framework has been established, some practical implementation considerations regarding our work must be addressed. In ideal circumstances, in order to provide a solid experimental framework regarding future experiments in the scope of optical communications, pure LG modes would provide an attractive choice.

Pure LG modes are, as it is expected, beams that closely resemble both in phase and amplitude the theoretical results predicted by result 1 [61].

Since these modes are heavily mathematically characterised, physically very studied and still researched and have attractive features for several applications, a panoply of possibilities would be available regarding future studies in optical communications. Some examples are OAM multiplexing and demultiplexing, beam information exchange studies, advanced modulation techniques, quantum information and communication experiments and beam shaping itself [25, 31].

In addition to the usual challenges of high precision experimental beam shaping, LG modes must be shaped both in amplitude and phase as it is shown in figure 2.5 [61].

Unfortunately, generating pure LG modes may prove itself still quite challenging. As it was previously presented, prompt LG mode generation is possible through rather complex refractive mode conversion methods, advanced computer generated holograms, dual operation SLMs or multiple single operation SLMs setups. At the time of this work, only a very limited number of phase only low cost SLMs were available. Despite LG modes generation have been reported through the usage of a single phase only SLM [62], at the time of this work these methods were not sufficiently developed in order to provide a viable work basis while presenting themselves as complete field on their own merit and complexity.

Unable to modulate both phase and amplitude in order to generate pure LG modes and given our timeline and limited resources, a simpler approach is needed.

Recalling that the core of this work is the study of OAM in optical communications, other OAM carrying beams may be used or less pure forms of LG modes. By using single operation phase SLMs, different methods will be explored to generate OAM carrying beams which can be interpreted as impure LG modes: through direct helical phase shaping and LG mode decomposition. Both these methods are still present in state of the art work and therefore provide a relevant working basis and are detailed further on. For further information on their application at the state of the art, the work by Willner et al. [25] may be used as a reference.

3

Computational Aspects

Contents

Objectives

In order to enable our experiment, some computational work is required in two different fronts. First, we will need to provide some code to be able to generate the phase patterns which we will load in our SLMs in order to shape our wavefronts. Second, we will want to simulate the propagated field after the SLM interaction as a control method to our methodology. As an additional simulated experience, we will try to demodulate a spiral phase CGH OAM beam. In this section, for the technical development of these methods, unless stated otherwise, the books by Poon and Liu [63] and Picart and Li [60] were used as guides for Matlab. The gray scale for our images follows the one indicated in figure 2.5.

Phase Pattern Generation

The LCoS SLM devices allow for a precise control of the phase front of a beam [38, 64]. Typical commercial solutions regarding these equipments include specialised software solutions which enable optical beam pattern generation, aberration correction and other useful features [65]. Unfortunately, at the time of this work, given the high cost of more typical solutions in the order of several thousands of euros, only low cost SLMs, which cost ten times less, were within the budget. Given these constraints, we chose as our reference equipment a LCoS SLM SDE1024 by Cambridge Solutions[1]. As it is expected, low cost solutions don't provide software support at the same level of more typical brands and so, in order to be able to use our SLM, phase pattern generation routines had to be created from scratch. Our SLM is controlled through a standard VGA port which connects to a standard PC. The SLM is detected as a generic computer display by the PC. The SLM pattern is then loaded by simply displaying an appropriate image in that display. Given this context, a Matlab routine shown in appendice B was created to generate these images. The routine consists in creating a square matrix which is then filled according to an appropriate equation (which shall be detailed further on) which describes a certain pattern using a cycle. Then, a grey scale color map is applied to the numerical matrix and a print out is exported carefully imposing ratio constraint requirements. For inverse masks, the color map may be easily inverted by adjusting the appropriate parameter in the routine (further details commented on code). All the images with generated with 1024 per $1024\,\mathrm{px}$ in order to fit the width of the SLM and the excess length is cropped in the image loading method. When these greyscale patterns are loaded into the SLM, they translate into CGH which allow phase modulation[1]. The most practical way to control the SLM was found by using presentation software like Microsoft PowerPoint or Apple Keynote. Presentation software allows proper resolution control, and also facilitate the correct placement of the phase patterns regarding alignment and size while providing some manipulation capabilities which prove themselves to be useful to do some tweaks (namely if one wants to disable phase modulation in some zones of the SLM matrix). The convention followed to characterise the generated phase patterns is the usual one, that corresponds to a direct interpretation of the topological charge associated with them. This implies that in our setup, since we use a reflective device, that in order to generate a l valued OAM beam, the phase pattern must have a $-l$ parameter. This is valid for every reflection that a OAM beam may have: it translates as an

[1] Since in this chapter, we are addressing computational aspects, the physical properties of our equipment shall be addressed in its proper chapter further on.

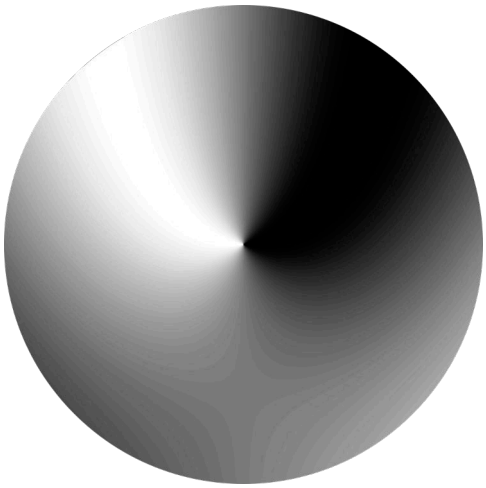

Figure 3.1: Pure spiral vortex $l = -1$.

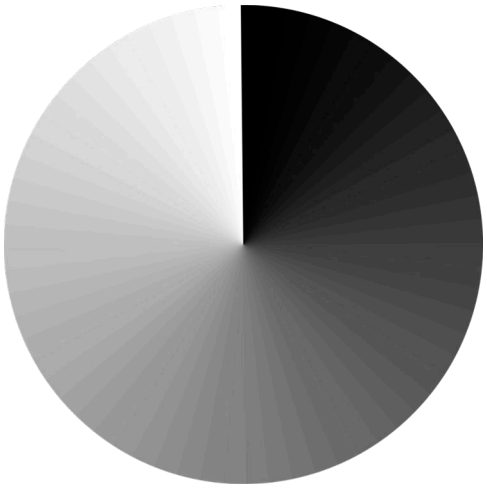

Figure 3.2: Linearized spiral vortex $l = -1$.

inversion of the topological charge.

Spiral Phase CGH

Before proceeding, it is important to distinguish the main differences between the two approaches that were used to shape our OAM carrying beams. SLM beam shaping along with more classic but similar methods consists of imposing a certain phase pattern in a diffractive optical element, in our case the LCoS SLM. In order to generate phase shaped LG beams, the pattern may be the phase profile of the interference of a certain LG beam with a Gaussian beam. For LG^0_{-1}, the singularity pattern is shown in figure 3.1. This rather complex phase profile is unnecessary for our purposes. The essential phase feature which allows for OAM creation resides in the center of the phase pattern where the phase is shaped like a spiral. This way, in order achieve our purpose, it suffices to generate a simpler phase profile as shown in figure 3.2. Additionally, as it is visible in the phase profile of the figure 3.1, the gradient is curved along the polar angle. However, it is usual to approximate this linearly as it is shown in 3.2. Despite uncommon in high precision beam shaping methods because of its approximative nature, this procedure is standard regarding not only but also the optical communications applications of OAM as it can be seen in the work by Wang et al. [48] and Bozinovic et al. [46]. Given this context, the final image may be described as a greyscale matrix $m \times n$ which obeys the equation 3.1 which will be used directly in routine `phasemask.m` shown in the appendice B.

$$T(m,n) = T_0 \mod (\theta l, 2\pi) \tag{3.1}$$

$$\theta = \arctan 2 (y_{m,n}, x_{m,n}) \tag{3.2}$$

In this equation, θ is the polar angle, l is the topological charge and T_0 is an adjustment parameter only relevant if we want to create superpositions of multiple patterns in order to adjust relative weight on the final pattern which we won't be using. Perhaps one of the most important features of these phase patterns is that they allow for wavelength, beam size and resolution independence although restricted by pixel pitch. Some examples of generated spiral phase patterns are presented in figures 3.3 and 3.4, which will be the ones we

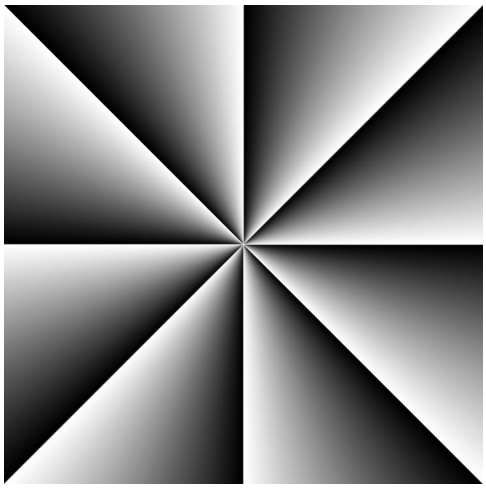

Figure 3.3: Spiral phase pattern for $l = -8$.

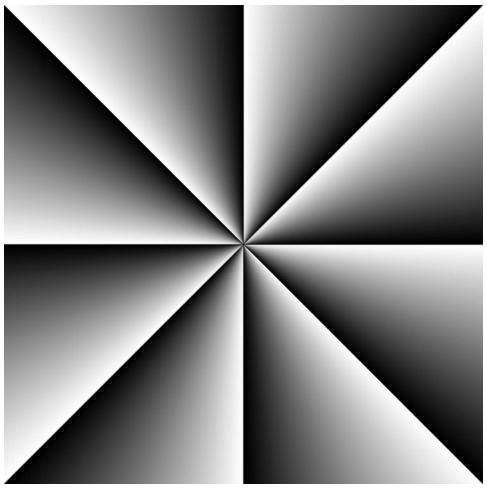

Figure 3.4: Spiral phase pattern for $l = 8$.

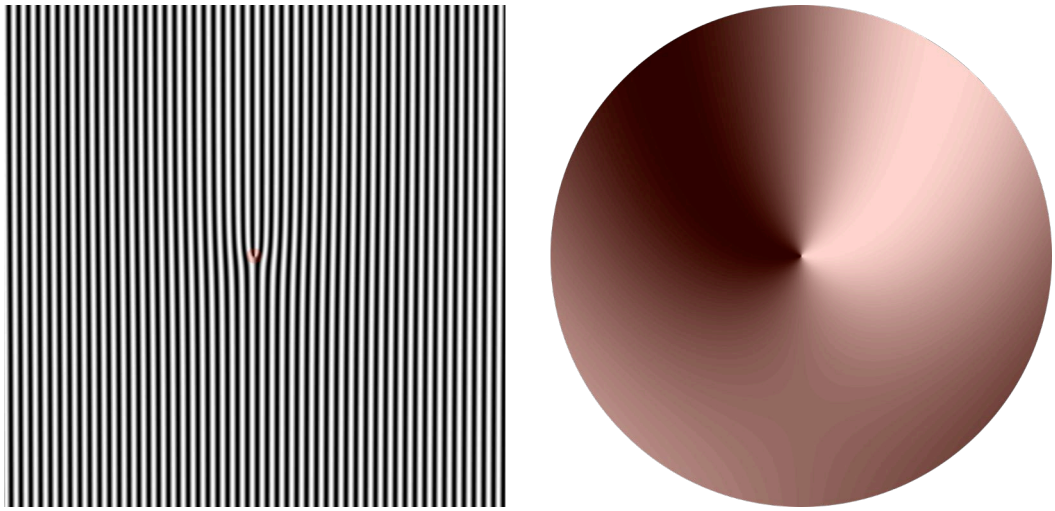

Figure 3.5: Forked diffraction pattern with $l = 1$ on the left. Vortex singularity which provides OAM zoomed in in the right.

will be using in our experiment. To this method, opposed to the next one, is often described as aligned spiral phase shaping.

Forked Diffraction CGH

Despite different, this method is actually based in the former one. In the previous method, it appears to be experimentally challenging to ensure high precision of the generated OAM beam since the LCoS SLM is a reflective device which will always reflect some unmodulated Gaussian component of the original beam. Since OAM modes are much less intense than the Gaussian component, the final beam will be affected by a Gaussian component. In order to address this difficulty, by combining the former spiral phase pattern in its approximate form with a standard linear diffraction pattern, the OAM modes may be separated in different angles as it shall be demonstrated further on. Again, if we consider a $m \times n$ greyscale matrix, this combination may be described by equation 3.3.

$$T(m,n) = T_0 \cdot \exp\left[\alpha \cdot li \cdot \cos\left(\theta \frac{l}{2} - \frac{(2\pi r \cdot \cos\theta)}{G}\right)\right] \tag{3.3}$$

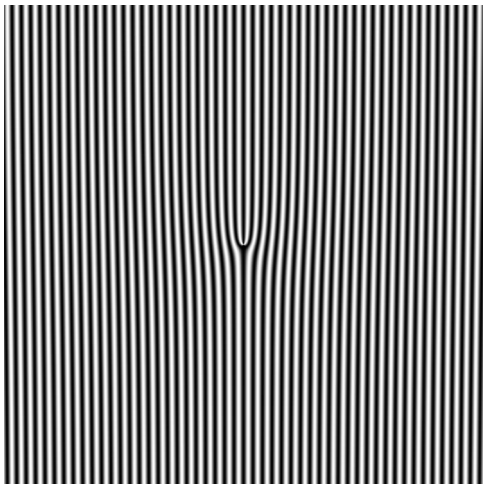

Figure 3.6: Forked diffraction phase pattern for $l = 2$.

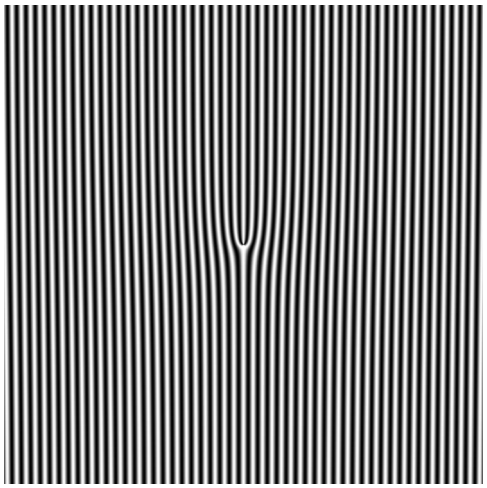

Figure 3.7: Forked diffraction phase pattern for $l = -2$.

$$r = \sqrt{x_{m,n}^2 + y_{m,n}^2} \tag{3.4}$$

More complex than the first equation, this equation parameters has the same parameters and some additional ones: G controls the fringe spacing through what can be interpreted as a scale factor around the singularity[2] and α is an amplitude adjustment parameter which we won't be using since we use a phase only SLM. An example of a generated phase pattern according to this equation for $l = 1$ is shown in figure 3.5 and $l = 2$ and $l = -2$ (all with $G = 30$ which translates into about 8 px per fringe) in figures 3.6 and 3.7 respectively. Again, the essential feature in this pattern is the center of the image where the singularity takes place. Given its form, this patterns are frequently referred as forked diffraction patterns or, opposed to the former method, unaligned spiral phase shaping. This equation is also implemented in the phasemask.m routine available in appendice B.

Propagated Field Simulations

As we've mentioned previously, a simple simulation of the propagated field was developed in order to predict some results and as a control method of our experiment. The algorithm used is a direct implementation of the Fresnel diffraction approximation derived in chapter 2, in section 2.2 namely in subsection 2.2.4 and shown in result 5.

Result 5 (Fresnel Diffraction Approximation)**.**

$$U^{out}(x_2, y_2) = \iint_{-\infty}^{+\infty} U^{in}(x_1, y_1) \cdot h(x_2 - x_1, y_2 - y_1)\, dx_1 dy_1 = U^{in}(x_1, y_1) * h(x_1, y_1) \tag{2.20}$$

$$h(x_1, y_1) = \frac{\exp(ikz)}{i\lambda z} \exp\left[\frac{ik}{2z}\left(x_1^2 + y_1^2\right)\right] \tag{2.21}$$

[2] Big values for G increase the size of the fringes "zooming in" the singularity while small values "zoom out" distancing ourselves from the singularity and increasing the fringes pattern. It is important to notice that this pattern has some resolution independence since the image appears to have fractal properties which can optically be identified by creating an image with a small enough value of G. Resizing this patterns beyond certain limits of spatial resolution results in a recurring pattern, although scaled.

This choice was made because the direct implementation of the angular propagation method derived in the subsection 2.2.3 of the same chapter and section, shown in result in result 4 is extremely complex. Therefore, it is unreasonable to follow such path in this comprehensive work, although it may be of interest to pursue it in a dedicated work on its own merit. Also, the Fresnel approximation for diffraction seems to be the standard approach in these cases, although its implementation may be more or less refined [48].

Following the result 5, the expression can be further simplified by writing it in the form of equation 3.5.

$$U^{out}(x_2, y_2) = \mathscr{F}^{-1}\left\{\mathscr{F}\left\{U^{in}(x_1, y_1)\right\} \cdot H\left(\nu_{x_1}, \nu_{y_1}\right)\right\} \tag{3.5}$$

Function H presented in equation 3.6 is the transfer function valid for the Fresnel diffraction approximation and is obtained from the Fourier transform of the Fresnel diffraction approximation impulse h shown in equation 2.21.

$$H\left(\nu_{x_1}, \nu_{y_1}\right) = \mathscr{F}\left\{h\left(x_1, y_1\right)\right\} = \exp\left(ikz\right) \cdot \exp\left[-i\pi\lambda z\left(\nu_{x_1}^2 + \nu_{y_2}^2\right)\right] \tag{3.6}$$

Our algorithm implements this approach. Its input is a starting optical field which we want to propagate. The input will correspond, as far as phase is concerned, to the phase pattern imposed in our Gaussian beam. We also assume the original pattern to propagate is the modulated phase of the beam at the SLM and therefore, since our device is reflective this implies that experimentally the pattern that gave origin to it is inverse from the one we use to propagate the simulation since reflections invert the topological charge of OAM carrying beams [48]. In order to avoid confusions, here we will ignore the issue of reflections and simulate our beams as we would by using transmissive SLMs which means that the topological charge is not inverted in the simulation which demands caution. The implemented routine allows for input of the laser wavelength `w`, the complex amplitude of the starting optical field `U0`, which is introduced through the image input of the phase pattern and `L0` which is the width of starting optical field plane.

Possessing these variables, the sampling theorem is applied suggesting the maximum distance allowed for diffraction according to the sampling theorem [60] expressed as `zmax=L0^2/A/w` (where `A` is the biggest size of the pixelated matrix), suggested maximum value for the diffraction plane distance `z0`.

The routine proceeds by squaring the input image of the optical phase field which is stored in a XRGB matrix (which discards color as XRGB is defined), and then, a grayscale color map is applied to the stored matrix to plot the input field with the appropriate axis. Then, the bi-dimensional fast Fourier transform algorithm of Matlab `fft2` is applied to the input field as indicated in equation 3.5 while calculating the needed spatial frequencies and its respective ranges. Finally, the transfer function 3.6 is defined and the diffraction convolution is calculated. The final field is then obtained through the Matlab's inverse fast Fourier transform algorithm `ifft2` of the convolution as indicated in expression 3.5 and plotted in a figure.

The routine wasn't provided with scaling calculations since they weren't needed but scaled axis may be easily added in the future. Therefore, the propagation results are pixel size images which means that no scaling considerations will be done about them.

Results

Before proceeding, it should be noticed that tests using simple apertures where done in order to verify the implementation. Both Fraunhofer and Fresnel regimes were tested and Fresnel regime appears to perform

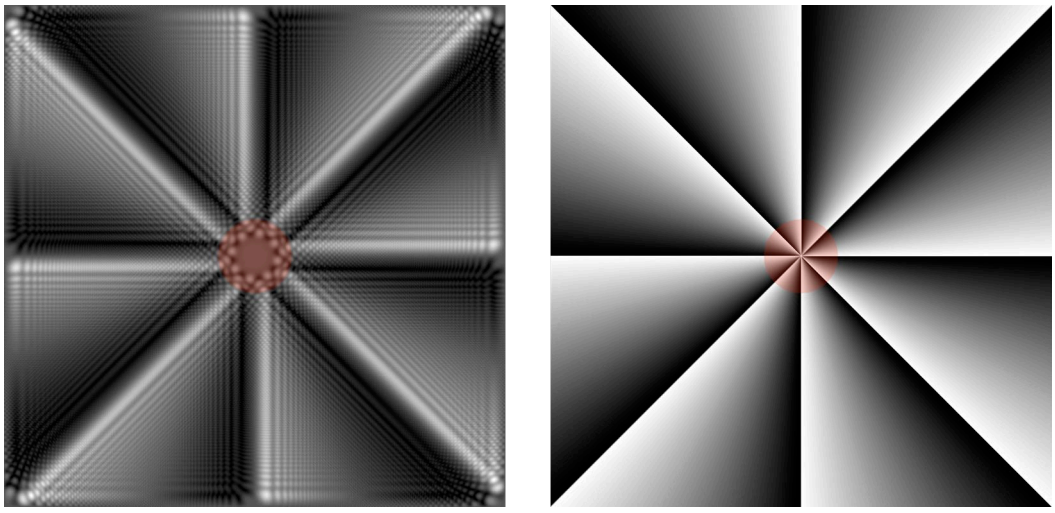

Figure 3.8: Propagation simulation for $l = -8$ spiral CGH on the left and original phase CGH on the right (the phase CGH represents the optical field, not the SLM phase pattern). The OAM optical vortex is signaled in red on the left and the incidence is signaled in red on the right.[4]

closer to reality as predicted and therefore, Fraunhofer results were discarded.

OAM Generation for Multiplexing

As our main objective, three tests were performed using three different phase patterns in the same physical conditions: wavelength `w=633nm`, diffraction plane distance `z0=100mm` and width of the starting field `L0=9mm` (the width of the SLM matrix). Both spiral and fork CGHs were propagated with a value of $l = -8$ for the former and $l = -2$ for the latter. Inverse phase patterns produce similar results, although inverted. The propagations assume that the entire SLM cell is illuminated for simplification reasons[3]. The starting patterns and their respective propagation are presented in figures 3.8 for the spiral phase CGH and 3.9 for forked diffraction CGH[4].

OAM Demodulation for Demultiplexing

In order to try to simulate OAM spiral phase CGH demodulation, a simulated experience using two configurations was done: a composition of a propagated OAM $l = 8$ beam and an inverse spiral phase CGH was made using imaging software and contrast adjustments were made to diminish aliasing effects on the former. As a control subject, the same was done but chaging the second phase pattern to one equal to the original one. Both situations assume the viewer is behind the beam, and we want to propagate the spiral beam through two inverse SLM phase CGHs configurations. Because of this assumption, the color scale significance is inverted in this particular simulation (black for 0 and white for 2π). The resulting images were propagated in the simulation and both results were filtered from aliasing using equal parameters. Results are presented in figures 3.12 and 3.13.

[3]This is false since only a localized beam with about 1.2 mm will be used but this doesn't affect the validity of the results and the early experimental tests which illuminated the entire cell, actually produced results as the ones presented in the case of the spiral CGH where this is relevant.

[4]The red circle spots in the original phase patterns are also an approximated representation of the beam we expect to use, having a diameter of about 15 px, the phase patterns were made to fit the SLM with a width of 1024 px which by assuming a pixel size of 9 m translates into 1.35 mm which is close to the value of 1.2 mm we expect to use.

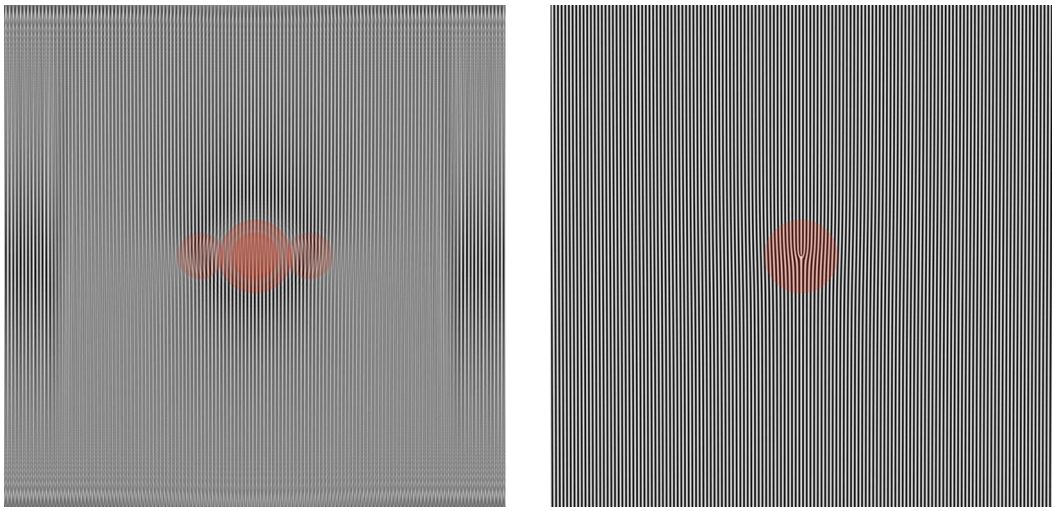

Figure 3.9: Propagation simulation for $l = -2$ fork CGH($l = 2$ on the left and $l = -2$ on the right) with $G = 15$ (4 px per fringe which is about 40 m in our SLM) on the left and original phase CGH on the right. The OAM optical vortices are signaled in red in the left and the incidence is signaled in red on the right.[4]

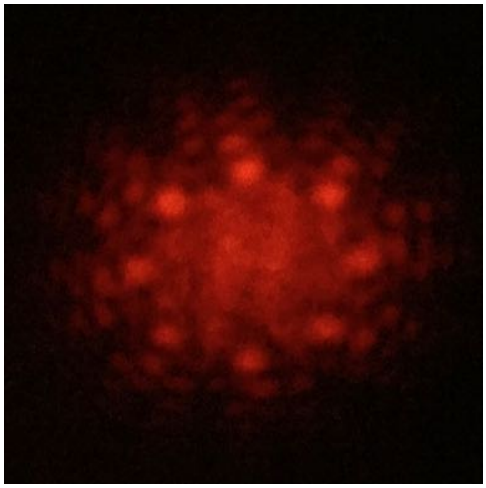

Figure 3.10: Long distance propagation photo for projected $|l| = 8$ spiral CGH using the setup shown in figure 4.6 without a polariser.

Figure 3.11: Long distance propagation photo for $|l| = 2$ fork CGH with $G = 15$ (4 px per fringe which is about 40 m in our SLM) using the setup shown in figure 4.6 without a polariser.

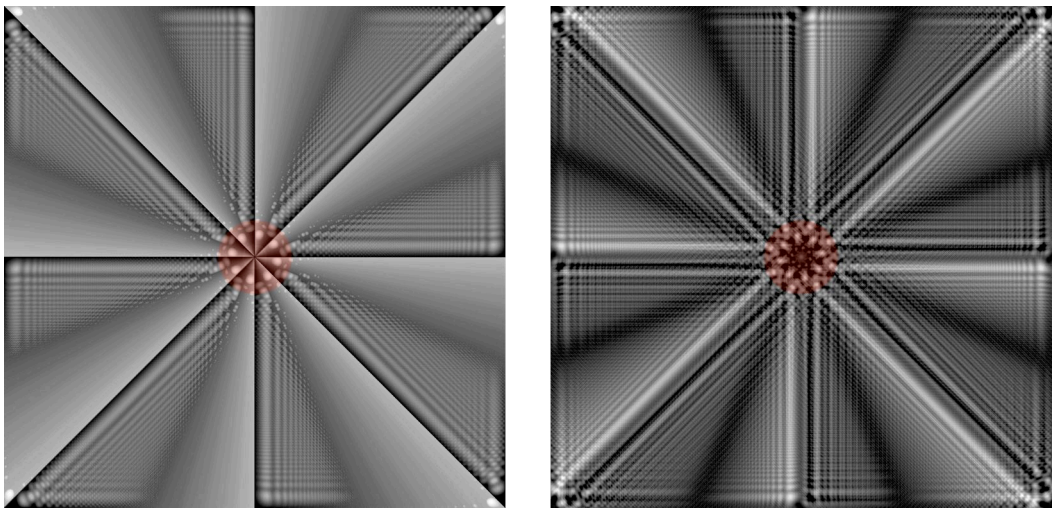

Figure 3.12: Composition for $l = -8$ spiral beam and $l = 8$ phase CGH on the left and its propagation on the right. The OAM optical vortex is signaled in red on both sides.[4]

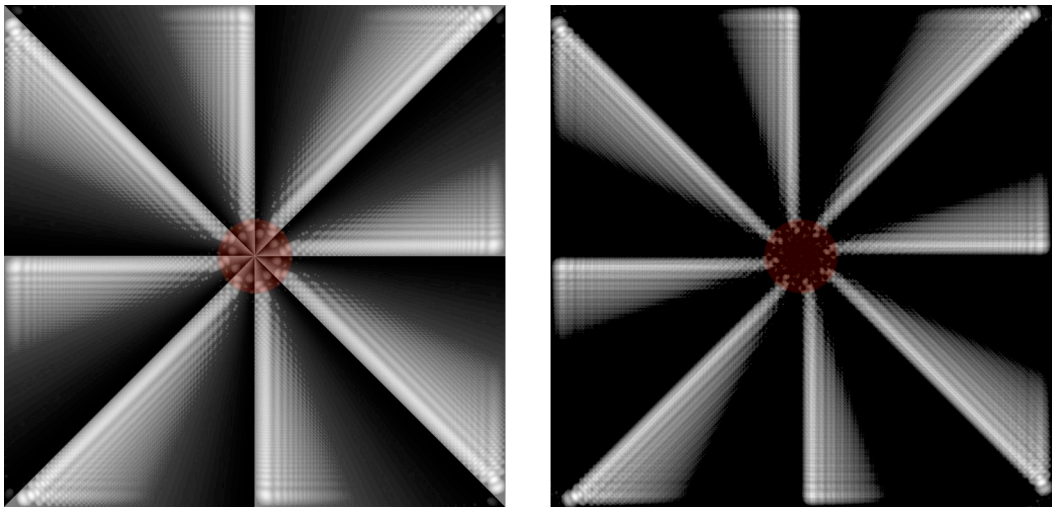

Figure 3.13: Composition for $l = -8$ spiral beam and $l = -8$ phase CGH on the left and its propagation on the right. The OAM optical vortex is signaled in red on both sides.[4]

Comments

The pixelation of the final results is probably related to aliasing but also to the use of fast Fourier transform algorithms instead of more refined implementations of the Fourier transform, namely by using polar coordinates [66]. However, FFT based algorithms are very fast and allow for a practical approach where fast results are more important than exact ones. Since the purpose of this simulation is to control our experimental results, at least as a starting point this should suffice. Later work may include improvement of this routine.

Regarding the spiral diffraction CGH propagation, the result appears quite in agreement with the early results obtained in the laboratory by direct observation of intensity (due to amplitude-phase coupling effects present in Twsited Nematic Liquid Crystal (TN) technology) [65].

Regarding the forked diffraction CGH propagation, a different problem arises. In our theoretical approach we always assumed the premise of very small angles in the diffraction problem. The pattern of unaligned spiral phase shaping, actually diffracts in angles which are significant. This may affect the validity of our approach which summed with the pixelation problem, may weigh heavily on the quality of the simulation. However, despite these issues our simulation is not without merit and the actual result is surprisingly good. A central maximum can be clearly seen in the propagated field. Additionally, the symmetrically charged OAM beams vortices can be easily seen where they should appear. A very interesting detail is that the swirl of the vortex can be identified quite clearly in this simulation as shown in figure 3.9.

As for the demodulation attempt, we have to be careful. This simulation was performed as a trial experiment. Some pre-processing and post-processing was needed in order to improve the results. The contrast of the original OAM beam was enhanced using imaging software through fixed parameters in both situations. Then, the beam was composed with a unaltered inverse phase pattern and another beam was composed with a identical phase pattern. Both compositions were propagated. In order to reduce aliasing, fixed parameter contrast adjustment was performed in both results in order to eliminate aliasing effects. The results are quite in agreement with what we expect: the inverse phase pattern recovers some of the original phase while the the identical one maintains the singularity. However, given the rather heavy pre and post-processing pro-

cesses involved, without strict quantitative control measures, the result could be a coincidence. However, the adjustments made through contrast are not without relation to our real life setup: dynamic range limitations and the phase modulation limit of $0.8 \cdot \pi$ express themselves in augments of contrast in imaging which remove gray levels, which is equivalent to a reduced dynamic range. It should be added that the adjusted propagation simulations are actually more resemblant with real life results than the originals which is quite in agreement with the former assessment.

4

Experimental Setup

Contents

Objectives

The first and main objective of our experiment is to generate a OAM carrying beam using two different methods: aligned and unaligned spiral phase shaping. We hope to achieve this by loading the appropriate patterns generated in chapter 3, section 3.2 in a SLM [25, 31, 38, 48]. As a secondary objective of our experiment, we wish to back convert the OAM carrying beams generated in the first part of the experiment and recover the planar wavefront geometry[1]. This is done by loading an inverse phase pattern in the second SLM which will compensate the spiral phase and recover the plane phase front [48]. Two measurements are instrumental in our study: intensity and phase front profiles. The detailed procedures and setups for our objectives shall be covered further on through the next subsections. Depending on the authors and area of study, sometimes phase modulation effectiveness is often referred as phase dynamic range or simply dynamic range[2] while multiplexing is usually used in optical communications since physical modulation may be confused with information modulation. In this document, all the definitions are used rather freely but it should be noticed that every reference to dynamic range always relate to the phase front, and the term modulation usually[3] refers to phase front modulation in the physical sense. This choice is based on the fact that this work is focused on OAM carrying beams generation through phase front modulation or shaping.

Spatial Light Modulator

Before proceeding to the proper methodology description and other basic concepts, it is important to introduce a vital element of our experiment setup: the SLM. Here, we will address the physical principle of operation of this equipment and how it will interact with light in order to achieve our purpose. There are a lot of different SLM technologies like the DMDs, the MQWs, the magneto-optic, the acoustic-optic or electro-optic SLMs, but given the nature of our work, we will incise on Liquid Crystal on Silicon (LCoS) devices. The state of the art guide for SLMs regarding our objectives follows from [65] and [67] and detailed information about the underlying technologies of these devices is available in textbooks [68].

There are several types of LCoS SLMs but most of them rely on the application of an electric field to a Liquid Crystal (LC) substrate contained by optical surfaces [65, 67] . This is done through the usage of transparent electrodes patterned onto the inner surface of the containing optical surfaces which form the pixelated matrix of the LC SLM [67]. Thousands of pixel LC cells constitute this matrix where the voltage is applied [65]. Because of this, their categorisation often divides itself rather ambiguously between basic principle of operation and the type of LC used, since the electrooptical properties of the LC cell define greatly the operational properties of the device [67].

In addition, several factors regarding speed and efficiency condition these devices which summarize into two important parameters: spatial resolution and frame rate [65]. While display applications usually require relatively large resolutions (above 1000×1000 px) and slow frame rates (30 Hz to 60 Hz), some optical applications demand modest resolutions (about 100×100 px) and fast frame rates (about 1 kHz) while optical data processing applications demand both (above 1000×1000 px and above 1 MHz) [65]. For our purpose, a good

[1] This back conversion principle may be used in theory as a multiplexing method, by using several different OAM beams superposed.
[2] Despite the usage of this regarding intensity in several optical devices.
[3] Outside every state of the art explanation or third party work.

spatial resolution is paramount and since this is a proof of concept work, despite speed being important in the long term for commercial applications specially regarding the demodulation process, which selects the OAM channel to demultiplex. It should be noticed that despite the usage of rather slow frame rate SLMs for multiplexing, terabit performance capabilities have been obtained with this limitation [25, 46, 48]. For the current purpose, we are concerned about efficiency since in principle, we wish only to multiplex information in order to be able to use a future OOK modulation scheme which requires only a fixed configuration in time. The nature of these factors shall be enlightened further on. Along with those parameters, and focusing on LC SLMs, despite several differences usually related to the core LCs, they are usually characterized by the properties discussed further on, if applicable.

Liquid Crystals: Ferroelectric, TN and PAN

Naturally, the first and biggest distinction between LC SLMs are the LCs used to modulate the light. Other LC applications do exist despite those presented in this thesis [68], but for the sake of conciseness, only the most typical commercially available technologies are addressed.

Ferroelectric Liquid Crystals

In a Ferroelectric Liquid Crystals matrix, the ferroelectric couples follow the orientation of the externally applied electric field rotating the molecules along the optical axis [67, 69] Ferroelectric devices are fast (50 s to 100 s) but they are often limited to binary output and are very sensitive to shock and vibrations [67]. Their binary behaviour offers precise 2π phase modulation in ideal conditions. This binary behaviour makes them unsuitable to our needs since in order to shape the phase front of the beam, adjustable phase modulation is a requirement.

Twsited Nematic Liquid Crystals

TN technology will be our main focus regarding LCs since our equipment of choice is based on this technology. As a source for this physical interpretation, specialized books and works were used [65, 68]. TN-LC technology is a product of the LC display industry from which resulted a strong availability of SLMs retaining a good enough cost-quality relation to use in research activities where spatial light modulation is required [65]. In TN-LC SLMs, the LCs start aligned in a helix pattern across each pixel cell[4] like it is shown in figure 4.1. By applying a certain voltage, the molecules start to align with the field breaking the aforementioned pattern allowing adjustable phase modulation. If a polariser sheet is present, the pixel cell acts as an intensity modulator (which is a straightforward way to check if our equipment is working). In our work, we won't be interested in the latter application.

In detail, as it is shown in 4.1, the LC nematic rods usually twist through an angle α between the two surfaces of 90°. The rods' long axes tend to follow the molecular director axis $\vec{n}$. The orientation of the $\vec{n}$ across the TN cell is specified by the twist and the tilt angles θ and χ illustrated in figure 4.1. The twist occurs around the direction perpendicular to the alignment layers which is defined as the twist axis. Assuming the z reference axis parallel to the twist axis, at a given plane perpendicular to the z axis, all the LC molecules

[4] Alignment polyamide layers coated onto the electrodes in the glass substrate undergo a polishing process in a specific way that both align the LC molecules along the surface and also establish a small pretilt angle with respect to the plane of the glass surface.

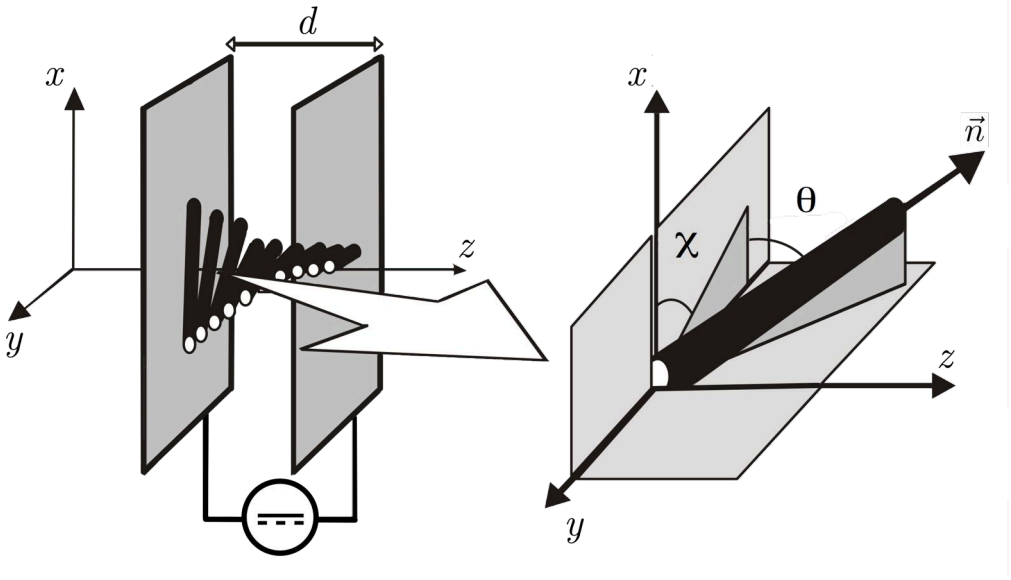

Ruiz [65]

Figure 4.1: Twsited Nematic Liquid Crystal LC pixel cell detailing $\vec{n}$, tilt angle θ and twist angle χ.

have the same orientation which allows to define both angles through the z coordinate: $\theta = \theta(z)$ and $\chi = \chi(z)$. Additional detailed information about TN-LC behaviour is available from numerous sources [65, 68].

A nematic LC material is an anisotropic medium which locally can be considered to behave as a uniaxial crystal whose optical axis is parallel to the molecular director $\vec{n}$ which results in different values for both the parallel and perpendicular components of both the dielectric permittivity and refractive index. Thus, since nematic LCs have positive dielectric anisotropy and positive difference of refractive index, one obtains the following equations 4.1 and 4.2 [65].

$$\Delta\varepsilon = \varepsilon_{\parallel} - \varepsilon_{\perp} > 0 \tag{4.1}$$

$$\Delta n = n_{\parallel} - n_{\perp} > 0 \tag{4.2}$$

The nematic LC molecules used in these devices are nonconductive and apolar. Therefore, by the application of an electric field parallel to the z axis, an induced dipole appears along the axis of the LC molecules that shifts the $\vec{n}$ to align with the z axis. Since the optical axis coincides with this vector, it is also shifted. This situation results in birefringence where the ordinary refractive index n_0, independent of the direction of the propagation of the light, is constant and equal to $n_{\perp}$ and the extraordinary refractive index n_e will depend on the angle between the optical axis and the light's propagation direction according to equation 4.3 where all the parameters have been previously defined [65].

$$\frac{1}{n_e^2(\theta)} = \frac{\cos^2\theta}{n^2} + \frac{\sin^2\theta}{n_{\perp}^2} \tag{4.3}$$

Finally, by applying the definition of birefringence following the manner usually found in literature related

to LCs as shown in the integral below, one obtains the 4.4 result [65, 68–70].

$$\delta = \frac{\pi}{\lambda} \int_{z=0}^{z=2d} \Delta n\,(z)\, dz = \frac{2\pi d \Delta n}{\lambda} \tag{4.4}$$

Therefore TN-LCs allow phase retardation as a function of voltage while allowing fast switching and some dynamic range. However there are more effective LCs and large polarisation changes may be in a issue in polarisation sensitive setups [67].

As a side notice for future simulations, it should be noticed that SLM numerical models for optical simulations do exist ranging from simpler ray tracing applications by using multiple Jones matrices [71] to sophisticated models derived from the Maxwell's equations [72, 73].

Parallel Alligned Nematic Liquid Crystals

Parallel Alligned Nematic Liquid Crystal (PAN) technology is similar to the TN but the initial alignment is parallel through the SLM. This decreases the polarisation issues referred above and allows for a superior dynamic range regarding phase but restricts phase modulation to the alignment direction of the LCs making these devices highly dependent of alignment and precision requirements. Similar to PAN technology is the Vertically Alligned Nematic Liquid Crystal (VAN) [67]. PAN SLMs by Hamamatsu are the technology of choice in the most sophisticated OAM optical communications studies [46, 48].

A figure depicting the three LC types is shown in figure 4.2.

Principle of Operation: EASLM and OASLM

Many liquid crystals are permanent electric dipoles while others induce electric dipoles through the application of an external field. Therefore, by applying electric fields to the matrix, the molecules can be rotated resulting in a change of the effective refractive index (due to birefringence effects) of the material which will translate itself as a spatially dependent phase change to any light traveling through the liquid crystal matrix [67].

Regarding the creation of the fields which will address the nematic liquid crystals, two methods are commonly used: the usage of pixelated electrodes on a silicon wafer such as a CMOS chip (Liquid Crystal on Silicon) constitutes the Electrically Addressed Spatial Light Modulator (EASLM) modulation method while the Optically Addressed Spatial Light Modulator (OASLM) achieves this through the usage of an incident light which will change the dielectric properties of a photo-sensitive material [5] sandwiched between two transparent electrodes resulting in a change of the original electric field [67].

Both configurations have its advantages and disadvantages and basic schematics are shown in figures 4.3 and 4.4. The EASLMs are closely related to the display technology based on TN LCs and this shows in the currently available market offerings where these devices often are the increasingly affordable TN LCoS micro-displays with a removable sheet of plain polarised film[6], providing fast update rates and high resolution while suffering from rather poor surface flatness, pixelation artefacts and poor phase modulation abilities due mainly to the type of LC used. While PAN EASLMs do exist, this LC type is usually more related to the more expensive optics industry. Optics industry related OASLMs by not using any electronics in their layered

[5] Typically amorphous silicon (a-Si:H).

[6] Allowing ease of use regarding intensity modulation objectives and quick equipment evaluation.

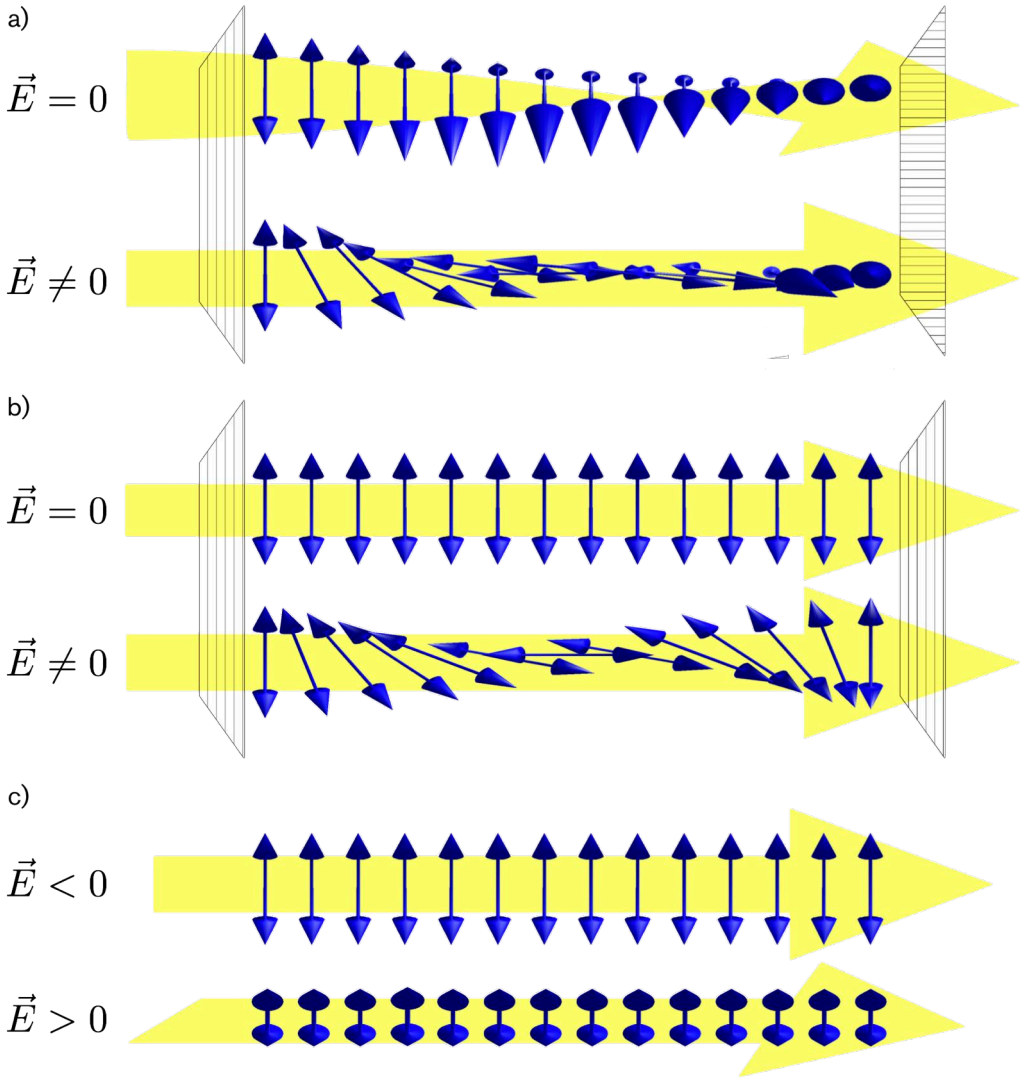

Preece [67]

Figure 4.2: a) TN, b) PAN and c) Ferroelectric LC technology functioning principle illustrated.

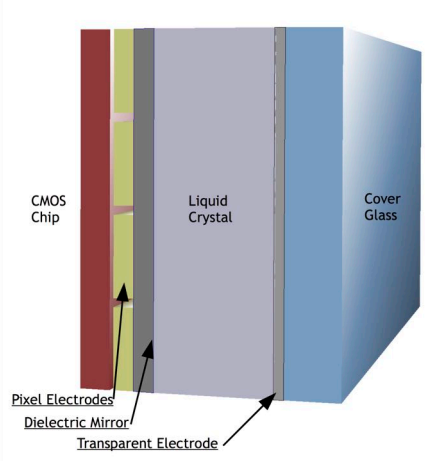

Preece [67]

Figure 4.3: Electrically Addressed Spatial Light Modulator (LCoS) schematic.

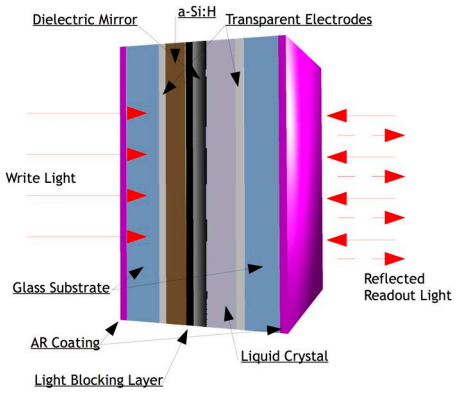

Preece [67]

Figure 4.4: Optically Addressed Spatial Light Modulator schematic.

composition have better optical flatness and have superior phase modulation properties but they are slower to respond and require intensity modulation. It should be noticed that at the time of this work, the difference in cost between the PAN and TN SLMs ranged from 10 to 15 times in favour of TN-LCs.

Conditioning Factors

Several factors may condition the functioning of the SLMs. We shall provide a brief overview of the most typical factors taken into account, and present our approach to tackle each one of them.

Diffraction Efficiency

Since SLMs are diffractive devices, diffraction efficiency appears as a reference measurement to ensure maximum efficiency in diffraction based works. A way of defining diffraction efficiency is through the ratio of the power of the 0^{th} order and 1^{st} order diffracted beams defined in equation 4.5. This has some relevance in optimizing diffractive CGH patterns, where through the choice of appropriate spatial parameters, aliasing and fill factor, nefarious consequences to the diffracted intensities may be reduced by fitting the patterns to the size of the physical LC matrix of the SLM. In the present work, this would make some sense in forked diffraction CGHs but since intensity is of little concern in the present work, we chose to adjust those patterns through simulation work done in chapter 3, section 3.3 in order to maximize the LG mode decomposition in order to be able to isolate each LG mode.

$$\eta = \frac{P_{1\,\text{st order}}}{P_{0\text{th order}}} \tag{4.5}$$

Fill Factor

Fill factor is related to the distance between the pixels in the LC matrix. The fill factor is defined by the ratio between the total LC area by the area of the SLM cell. The lower the fill factor is, greater will be the unmodulated light reflected by the grid structure. This may be reduced by the supplier by applying anti-reflective coating in the grid structure, but these details of implementation are usually not provided. Research

grade equipments usually provide this parameter on the opposite of our low cost SLM but calculations from the given specifications indicate a fill factor on the range of 98% which is doubtful since top tier equipments usually range in the 93%.

Aliasing

The aliasing problem is related to pixelated nature of the device since ideally, theoretical treatment assumes infinite resolution. This effect generates artifacts which are predicted in computer simulations based on pixelated inputs. Since our device has a good resolution, we don't expect this factor to be the source of much trouble. It should be noticed, that where high precision beam shaping is required, there is the development of holographic techniques which may minimize this [62].

Reflectivity or Transmittance

This is probably the most troublesome source of noise in SLMs. Reflective devices will always reflect some unmodulated light which reflects in the glass surface of the device resulting in undesired noise. Anti-reflective coatings or external filters may be used to diminish this, but it is a problem in the present work, since OAM modulated beams are not specially intense specially for some phase values (also, TN-LC suffer phase-amplitude coupling effects), and strong filtering may affect strongly the results. In the present work, filters were used on a trial approach, trying to reduce noise while maintaining relevant intensity. In transmissive SLMs, the same problem occurs through unmodulated light which crosses the device resulting in noise.

Angle of Incidence

This is obviously an issue related to reflective devices. Reflective SLMs work optimized to perpendicular incidence. Setups that make use of angular incidence will always result in wrongly modulated or unmodulated light which will be a major source of noise even for small angles. In the present work, due to equipment availability restrictions, an angular incidence was used, but we propose a future work in 6, section 6.2 using a perpendicular incidence setup through the use of a beam splitter.

Thickness

Another very important factor outside our control. Thicker devices usually provide superior phase modulation but are unfortunately increasingly unlikely in the market[7] and suppliers usually don't provide this value. Through the exploitation of thickness, [74] and [75] achieved increased performance beyond specifications. For our equipment of choice, this value is not known.

Voltage

As explained, LCs are controlled through DC balancing. Given the intrinsic bad performance in phase modulation by TN technology when the LCs are very tilted by the applied electric field, some research grade top tier suppliers like Holoeye claim optimized pixel by pixel performance through optimized nonlinear DC balancing, therefore improving the dynamic range performance. Our equipment of choice probably uses standard linear DC balancing.

[7] TN-LC SLM relate deeply to the display industry which pursues thinner and thinner LC matrices making ancient devices, usually recycled from older digital projectors a typical requirement in order to study this property effects on phase modulation.

Temperature

LCs behaviour is dependent on temperature [68]. Our equipment of choice claims operational range between $0\,^{\circ}C$ to $50\,^{\circ}C$. Since we work on a controlled environment clean room with an average temperature of $25\,^{\circ}C$, this is not expected to be an issue.

Cambridge Correlators SDE1024 LCoS SLM

Our equipment of choice is a LCoS TN SLM SDE1024 by Cambridge Correlators shown in figure 4.5 whose properties are shown in A.2. Given the prior information and regarding our objectives, this may seem a questionable choice of equipment but that it's not the case. State of the art SLM OAM beam generation for optical communications usually use PAN technology [46, 48]. However, OAM beam generation for optical tweezers applications have long been using TN technology [67].

Regarding possible issues of diffraction efficiency associated with TN technology, assuming a maximum value of 0.8π and OAM beam generation through the usage of a 0 to 2π unaligned spiral pattern, [67] refers that the beam is attenuated only in its diffraction orders as it should, since the unmodulated component should simply reflect aligned. He also states that the pixelation has little effect on the quality of the generated beams as long as the SLM has a resolution superior than approximately 10 per 10 pixels. Regarding aligned spiral patterns, even limited by a rather low dynamic range, partial phase modulation may be enough to generate optical vortices carrying OAM which is enough considering our objectives. Full phase modulation or demodulation are not a possibility with these technical limitations, although it is expected that at least a partial modulation and demodulation are possible by using these equipments. It should be noticed that despite that OAM is usually associated with integer values of l, fractional values of l are also possible [76]. Additionally, several approaches do exist to increase the dynamic range of TN technology up to about $\frac{3}{4}\cdot 2\pi$ which may be tried if needed [77, 78].

However, the possibility of a limited dynamic range or weak diffraction efficiency in our equipment is not without concern. Using an aligned spiral phase pattern, may result in very weak OAM modes comparing to the unmodulated component of the beam. This may or may not be a problem depending on the origin of the unmodulated component: if it results simply from polarisation changes within the SLM, despite reducing our signal, it won't interfere in subsequent demodulating since we can always remove it through a polariser, but if it is simply polarised unmodulated light due to dynamic range limitations, assuming it maintains polarisation it may be a problem regarding further treatment of the original signal since the subsequent SLM will treat this signal as a new optical input. Despite this bleak possibility, it should be noticed that this effect may be corrected through the reduction of the dynamic range of the used phase patterns and properly calibrating them as suggested in 6, section 6.2.

As a final remark regarding the choice of the SLM, state of the art PAN SLMs are incredibly expensive costing several thousands of euros while low cost TN-LCoS SLMs equipments are about one thousand euros each. This is a rather important limitation since our budget is very limited. Taking this into account, and at least some promising possibilities regarding our study, this was our choice.

Figure 4.5: Cambridge Correlators TN-LC SLM SDE1024.

Operational Standpoint

Regarding our equipment of choice and as a summary from an operational standpoint: undesired unmodulated light may origin from a low fill factor, high reflectivity, aliasing effects and angular incidence which will be addressed through the use of filters; a phase modulation limitation[8] will outcome from the use of TN technology related to the LCs themselves, linear DC balancing and possible thinness of the LC matrix may be addressed using a modulation technique explained further on.

Basic Concepts and Methodology

Three different methods were explored to generate OAM carrying beams: the use of a l valued spiral CGH loaded onto the SLM incised with linearly polarised light according to the specifications of the equipment, but following the works proposed by Pezzaniti and Chipman [77] and Moreno et al. [78], a beam possessing some ellipticity was tried in order to improve the phase modulation and finally, a fork diffraction CGH was also used. In a second phase, OAM is removed and the beam is back-converted which is done through the use of an inverse $-l$ valued phase spiral CGH.

OAM Generation for Multiplexing

The basic setup for OAM carrying beams generation is similar in broad terms in the three cases: we use a 5 mW 632.8 nm HeNe laser Melles-Griot 05-LHR-151, expand it to about 1.2 mm diameter from 0.8 mm maintaining the collimation of the beam and incise it in the active area of the SLM. This is done through a set of mirrors in order to minimize the angle of incidence in the SLM and the beam expander is a Keplerian setup

[8] Sometimes refered as dynamic range issues-preece-.

using two lenses of 100 mm and 150 mm. After the incidence in the SLM, the modulated beam is registered through a Phasics SID4 CCD-WFS[9] again at a closed angle in order to minimize the angle of incidence in the SLM (except on the fork diffraction CGH where the modulated beam diffracts with a significant angle) at a distance of about 10 cm. Due to undesired reflections, some tilting was needed in the last lens of the expander, but despite the nefarious aspects regarding phase this may cause due to deformations, the setup appeared to be robust enough and this wasn't an issue. It should be noticed that the lens tilt angle was solidary with the angle of the SLM which may have resulted in some corrective effect. This modest beam expansion was the maximum available since, despite having a 4.8 mm by 3.6 mm aperture in the CCD-WFS, OAM carrying beams are shaped like rings much larger than the original beam, whose radius increases proportionally to the absolute value of l. On the other hand, it is crucial to expand the beam in order to maximize the relative size of the modulated beam versus the unmodulated components which arise due to aliasing and reflectivity while easing the alignment and overall work. It was also observed that, the SLM had more difficulty in modulating a thinner beam, perhaps due to superior photon density. As a final remark regarding the input Gaussian beam calibration, great care was initially used to calibrate the beam using the CCD-WFS, but during the actual evolution of the experiment using several spiral phase patterns with different values of l, and even during the demodulation attempts, two main factors proved to be much more relevant than the Gaussian quality of the input beam: alignment and collimation. In a practical way, this is to be expected since theoretically, a Gaussian mode is important to obtain exact LG modes, but since we only wish to imprint OAM in our beam, as stated in chapter 2, section 2.4, mode purity is not much relevant to our purpose. Assuming a pixel size of 10 m adding 1 m to the reference value in order to compensate for grid spacing, a beam diameter of 1.2 mm and assuming the beam is collimated, and provided that OAM modes expand according to the LG beam diameter dependence on l expressed in equation 4.6 Padgett et al. [79], for the most used configuration of $l = 8$ we expect a ring of about 2.4 mm to the maximum intensity. Since the ring overflows from the maximum intensity point, about 3 mm total diameter is perhaps a good estimation. Since the CCD-WFS has a pixel size of about 30 m, an image of about100×100 px is a likely result.

$$d_{LG}(I_{max}) = \sqrt{2|l|}w(z) \tag{4.6}$$

Spiral Phase CGH Using a Linearly polarised Beam

Following the basic setup described above, the first approach consists in using a horizontally polarised beam as an optical input signal. In order to achieve this, a polarising beam splitter is used at the output of the HeNe laser following the schematic in 4.6. In order to assess the effects of the polarisation dependence of the SLM, profiles for both phase and intensity were measured. After attempts to use spiral phase CGHs of topological charges $|l| = 1, 2, 4, 8, 16, 32, 40,$ it was observed that the optimal value was $l = 8$. This optimal performance relates itself with two SLM limitations: partial phase modulation or limited dynamic range and aliasing effects. It may be possible that the use of lower wavelength lasers within the working range of the SLM may result in superior performance for higher values of the topological charge since a wavelength reduction,

[9] In order to measure phase profiles for OAM carrying beams, since the device imposes a Gaussian form to the phase, residual phase measurement must be used.

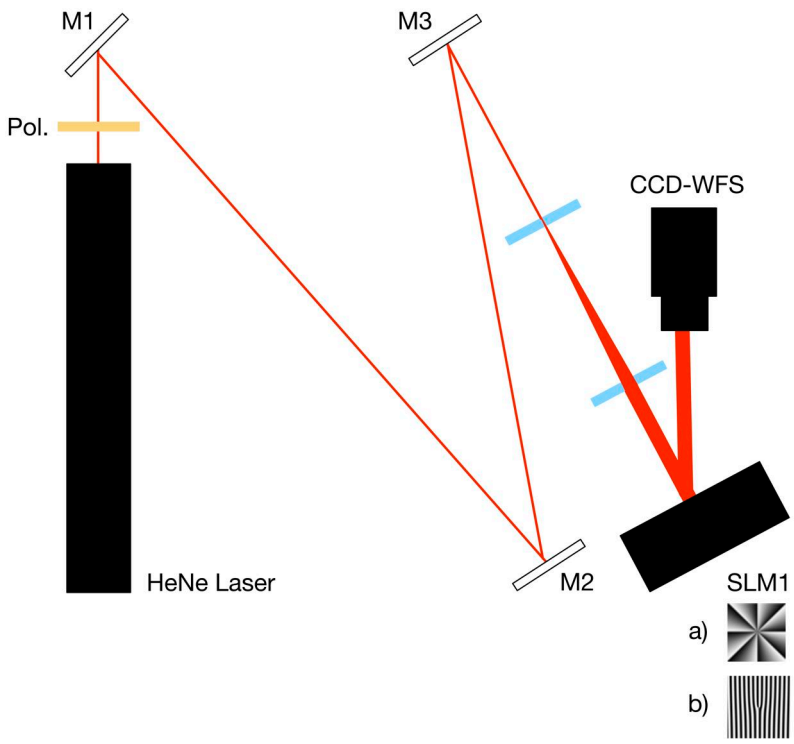

Figure 4.6: Setup for modulating an OAM beam for MUX schematic.

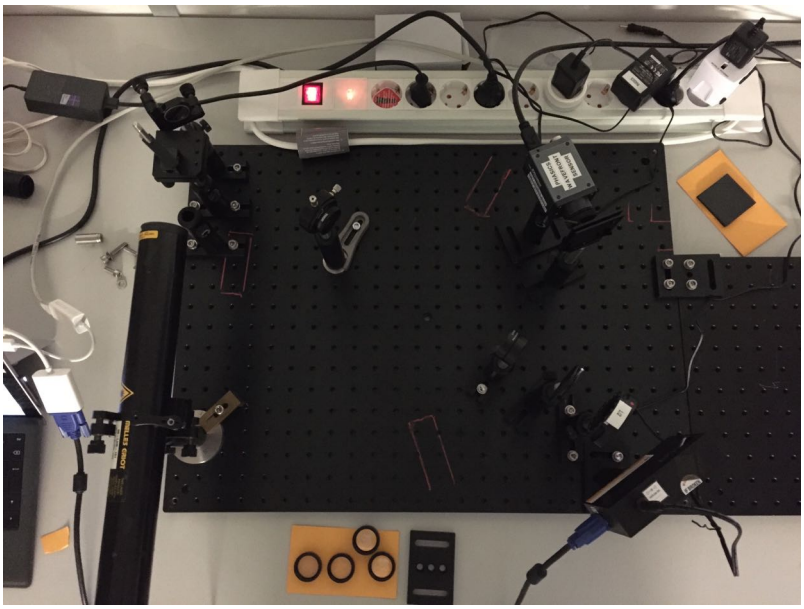

Figure 4.7: Setup for modulating an OAM beam for MUX photo.

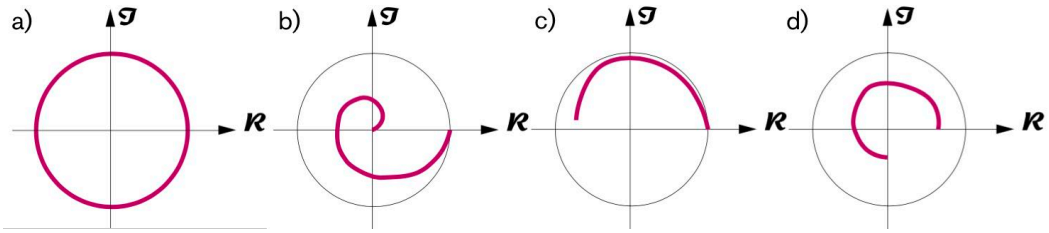

Figure 4.8: Complex plane modulation illustrations: ideal in a) and TN-LC SLM profiles in b), c) and d).

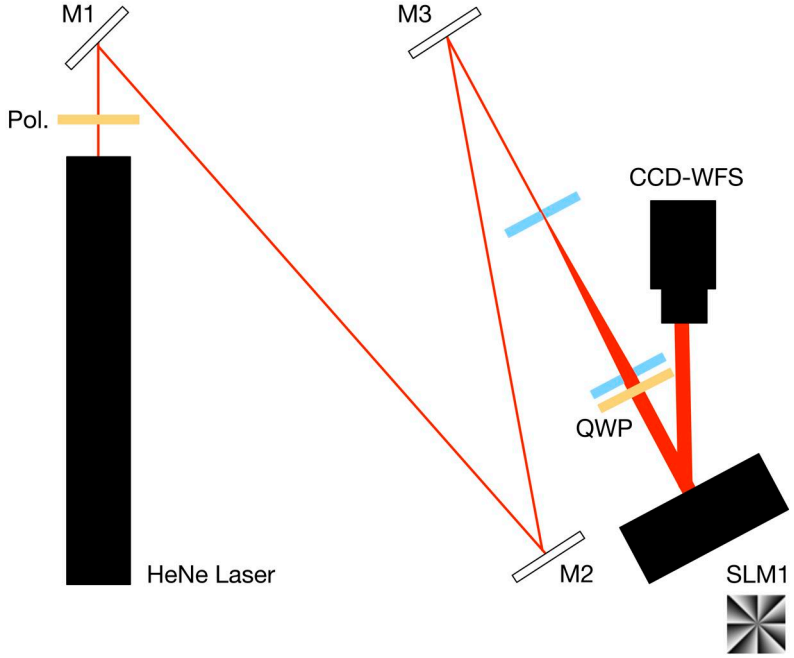

Figure 4.9: Setup for modulating an OAM beam for MUX schematic.

reduces the diffraction limit enabling higher effective diffraction resolution. In a practical way, from all the values tested, this was the value which minimized spurious undesired intensity at the center of the ring of the modulated beam.

Spiral Phase CGH Using a Elliptically polarised Beam

This approach actually resulted from an unexpected effect due to the use of a QWP instead of a HWP to adjust polarisation. The introduction of ellipticity in the polarisation had an unforeseen effect on the modulation of the beam using a TN-LC SLM. After some research, following the work of Pezzaniti and Chipman [77] and Moreno et al. [78], a setup involving a polarising beam splitter with a Quarter Wave Plate (QWP) was tested in order to introduce some ellipticity in the polarisation of the input beam. Again, following the conclusions by Pezzaniti and Chipman [77] and Moreno et al. [78], superior phase modulation was apparently obtained (while sacrificing amplitude as it is shown in figure 4.8) surpassing the specifications of the SLM which is promising for future work using TN-LC technology. Details regarding the setup are shown in 4.9 and again, a topological charge of $l = 8$ was chosen as in the previous case because of the same reasons. It should be noticed that the first result, despite apparently better, it needed further analysis. It should be added that the supplier recommends the use of a linearly polarised beam.

Forked Diffraction CGH

Finally, the last approach uses forked diffraction CGH. Regarding the setup, the general approach described above was used, using a polarising beam splitter in order to obtain a linearly polarised beam, following the supplier specifications. These structures result conceptually from the combination of a linear diffraction grating with a spiral phase plate. They are very important regarding OAM as fundamental property of light since they allow the full conversion of a TEM_{00} into a LG mode decomposition as it is predicted by the theory. In order to optimize the mode decompositions, the adjustment parameters were chosen following the results of the simulation in chapter 3, section 3.3. In order to validate the simulation, several adjustment parameters were tested and the simulation, despite its limitation proved itself as good method to chose working values for the parameters of the fork diffraction CGH. Details regarding the setup are shown in 4.6 and a topological charge of $l = 1$ was chosen since it was observed that this patterns become increasingly complex with the increase of l and alignment becomes complicated for values bigger than $l > 1$. The increased curve pattern complexity for high values of l in fork diffraction CGHs create nefarious consequences regarding aliasing so a simple approach was chosen. The rest of the parameters choice was done in 3, section 3.3.

OAM Demultiplexing

Regarding demodulation, only one approach was successful at the time of the writing of this thesis. In principle, demodulation should be possible using the other generated beams. Unfortunately time constraints limited our work to a single approach, since demodulation proved itself quite challenging using the rather limited resources available of time and equipment. However, it is important to notice that these limitations provide opportunities to creatively improve our setup through the development of methods usually disregarded and unneeded in high cost experiments. This is important in the long term, since eventual commercial success of technologies based on this type of work often depends on profit scalability which is sometimes impossible using the best research equipments available. It should also be added that this work continued to be improved on the behalf of the preparation of a paper by the author [3].

Spiral Phase CGH Using a Linearly polarised Beam

For the second part of the experiment, the modulated OAM beam should be back-converted to a Gaussian beam at least partially. The intensity singularity present in OAM beams should be replaced by a recognizable peak of intensity. In order to achieve this, another SLM is needed where an inverse $-l$ spiral phase CGH is loaded in order to cancel the spiral imprint which generates the OAM. Correct alignment is very difficult since it is needed in both orthogonal and polar coordinates in order to be able to rotate the SLM to adjust the spiral alignment optimizing the experiment. In order to achieve this, a ThorLabs cage system was used to hold the second SLM. Additionally, recalling the first beam expansion which is then followed by a OAM modulation which further increases the size of the ring, since our beam is now outside the diffraction region, the use of a 35 mm lens was needed at the input (in the cage mount) of the second SLM to optimize the back conversion process. The lens was placed in a position where the beam is reduced, but big enough to be able to be modulated. Since the Gaussian depth of focus may not apply to OAM modes, care was taken into account to

avoid the focusing point of the lens where the beam reduces itself to a point where it becomes smaller than the pixel size of the SLM which would obviously nullify any possibility of demodulation. From an operational standpoint, about 30 mm was found to be the optimum distance enabling a quick reduction while allowing the measuring of the demodulated signal at a possible operational distance regarding the cage mount and the size of the CCD-WFS. It should be added that the only possible way to measure the demodulated beam related to the angle of incidence restrictions, was through the use of the third order diffraction image, which happens to occur because of the pixelated nature of the LC matrix. Since we reduced the beam close enough to values not much higher than the pixel size, this effect was needed and fortunate. Since the beam suffers size alteration through an optical component, while the theory states it shouldn't be affected it is consistent with our visual analysis and measured data.

Additionally, a control test was conceived. The test is simple but quite clear: since the back conversion will be far from ideal due to the limitations of the SLM, and since the original spiral phase CGH generated beams possess some degree of noise in the center region, it is important to diminish the possibility that a peak might be related to noise rather than phase demodulation. Disconnecting the demodulating SLM doesn't erase this possibility since the LC randomized helix pixel matrix will cause unpredictable effects on the input signal and the use of a mirrored surface in the current setup is not only extremely hard but useless since we are measuring the third diffraction image of generated by the SLM pixel structure. Therefore, the way found was simply to load an identical spiral phase CGH which may have one of two results: assuming an inverse spiral phase CGH, it should result in a measurable central peak, if despite its pattern, the identical one also generates a peak, then, our experiment is at best inconclusive. On the other hand, if the residual intensities at the beam are modulated resulting in an improved intensity singularity[10], we can safely discard the possibility of the desired peak being noise.

[10] An additional use to this setup was found during the experiment: since residual intensities at the core are unavoidable, their modulation using a similar spiral phase CGH which generates another petal ring pattern, allows for superior modulation if both rings are aligned.

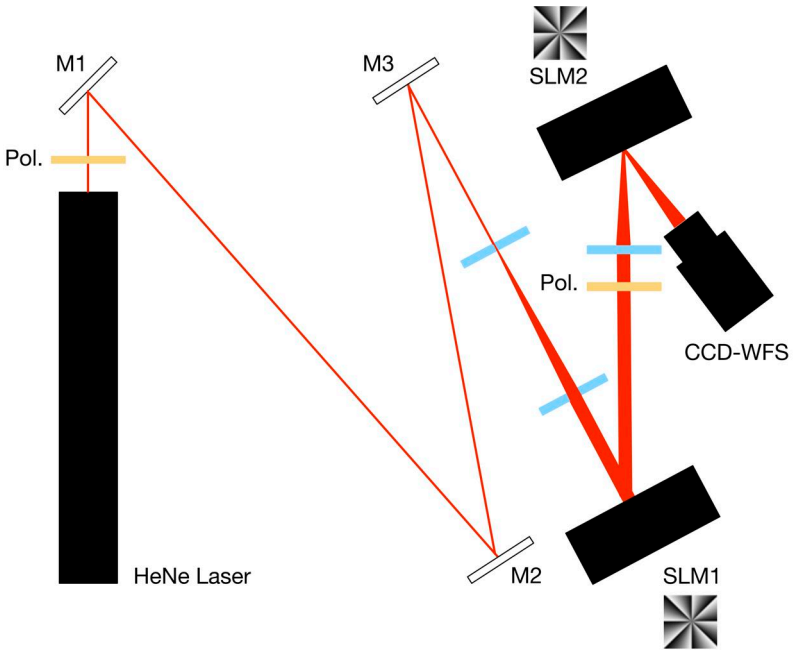

Figure 4.10: Setup for demodulating an OAM beam for DEMUX schematic (inverted mask shown for illustration purposes, due to the reflection the same mask must be used to demodulate the beam in the second SLM).

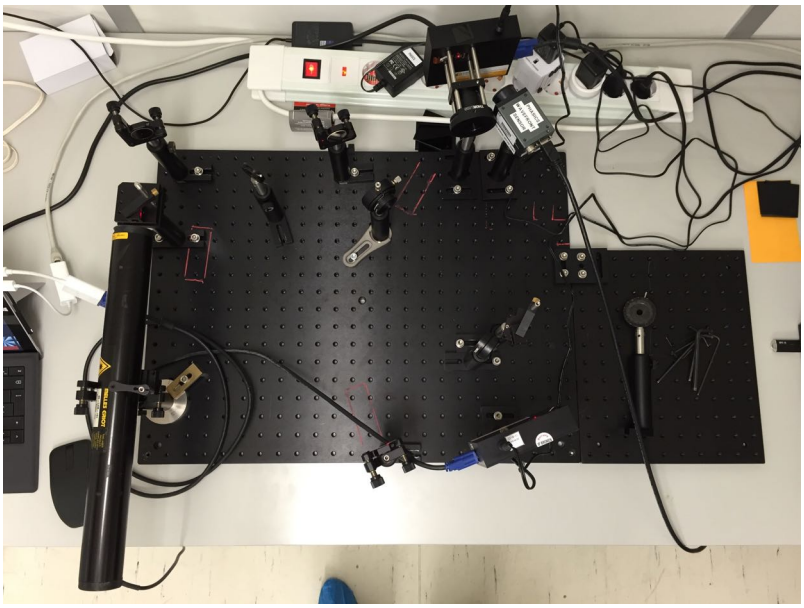

Figure 4.11: Setup for demodulating an OAM beam for DEMUX schematic.

5

Results & Analysis

Contents

Results Presentation

The obtained results divide themselves in two main sections. In section 5.2 the results for several methods regarding OAM carrying beams generation are presented usually through phase and intensity profiles with normalized values. The data in this section is raw meaning that no image or data enhancing was performed. In section 5.3 we also present both intensity and phase profiles with normalized values. In individual cases, some noise reduction was performed and shall be explained further on. In both sections, both 2D and 3D plots are presented in order to facilitate the visualization of the data.

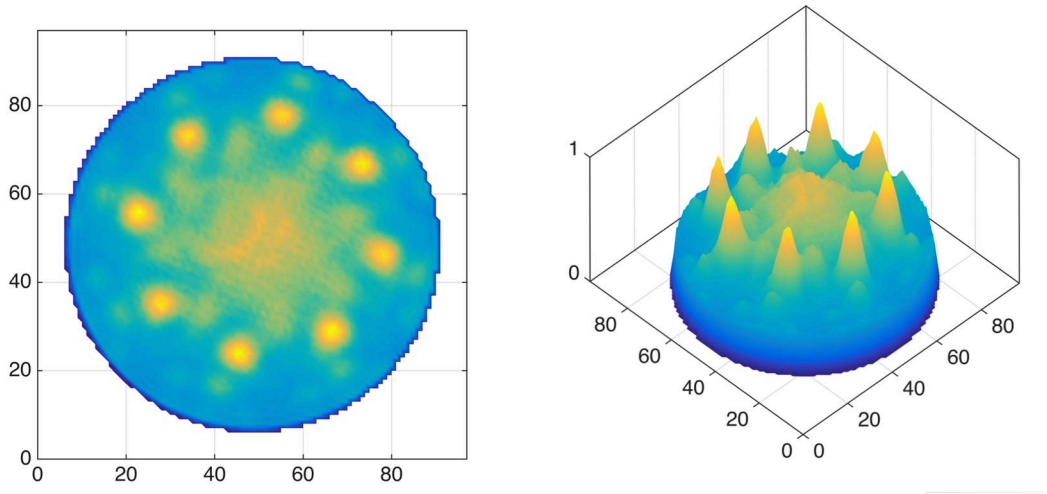

Figure 5.1: Normalized intensity profile for a $l = 8$ OAM beam (randomly polarised input beam and $l = -8$ spiral phase CGH).

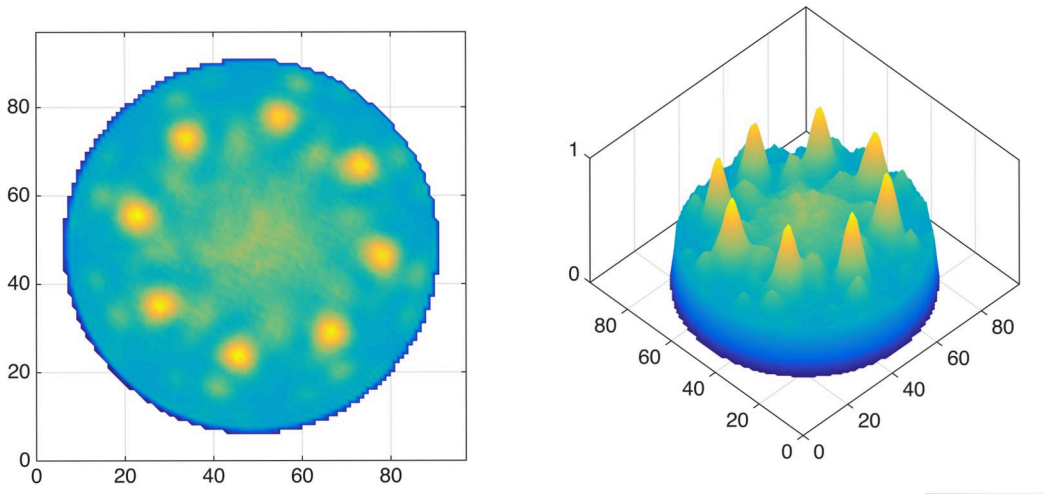

Figure 5.2: Normalized intensity profile for a $l = 8$ OAM beam (linearly polarised input beam and $l = -8$ spiral phase CGH).

OAM Generation for Multiplexing

Spiral Phase CGH Using a Linearly polarised Beam

The intensity results for a $l = -8$ spiral phase CGH (which generates a $l = 8$ OAM beam) using both randomly polarised light in figure 5.1 and linearly polarised light in figure 5.2 are within the expected. The quantity of unmodulated light is clearly visible in both cases but the introduction of a polariser visibly improves this issue. At the time of these measurements, wavefront measurement wasn't available but at a later stage, this measurement was performed and it is shown in figure 5.8 and it's according to the simulations done in chapter 3, section 3.3.

The intensity results clearly show the expected amplitude-phase coupling effects for TN technology where the intensity follows the phase profile. The obtained intensity profile despite being annular, the ring is made of intensity peaks instead of a smooth constant intensity ring as it is usually obtained by using PAN technology

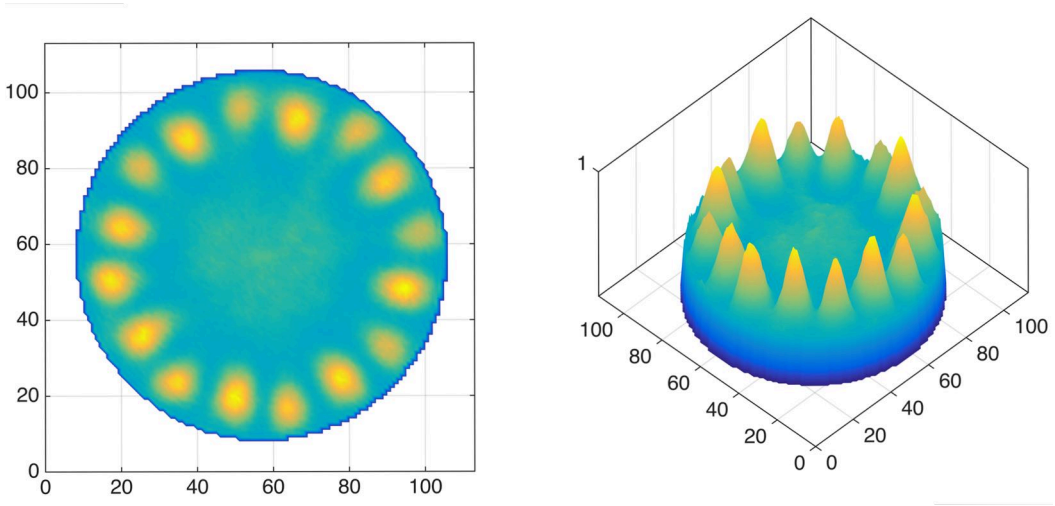

Figure 5.3: Normalized intensity profile for a $l = 8$ OAM beam (elliptically polarised input beam and $l = -8$ spiral phase CGH.)

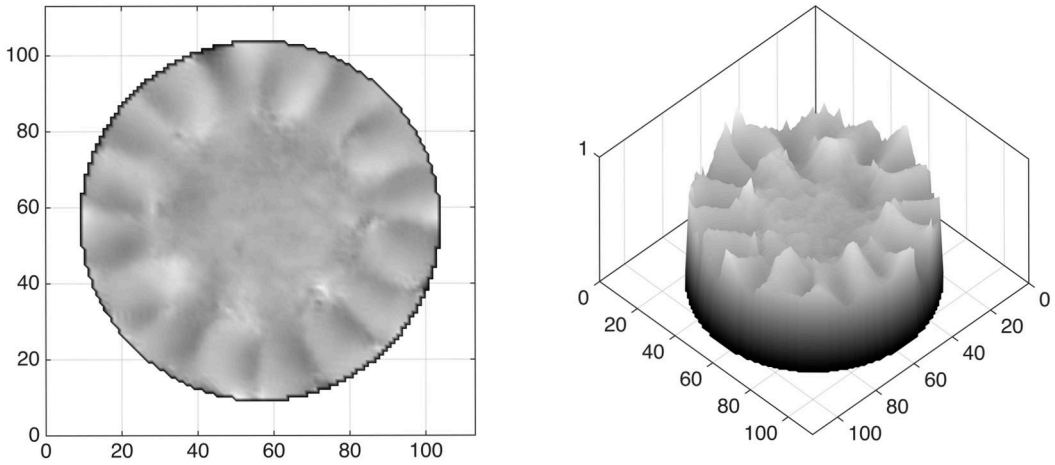

Figure 5.4: Normalized phase profile for a $l = 8$ OAM beam (elliptically polarised input beam and $l = -8$ spiral phase CGH.)

[48]. The limited phase modulation capability of our equipment, typical of TN SLMs, also helps to justify this result.

Spiral Phase CGH Using a Elliptically polarised Beam

Afterwards, still using the same $l = 8$ spiral phase CGH, by introducing a QWP in our setup adjusted to add some ellipticity to the polarisation of the input beam, a rather curious result is obtained. The intensity profile in figure 5.3 suggests improved phase modulation since the profile is more continuous and closer to a closed ring and the quantity of unmodulated light is greatly reduced comparing to the previous result. However, through the analysis of the wavefront of this beam, the profile in figure 5.4 seems to indicate an $|l| = 16$ wavefront which is strange. Closer inspection suggests some kind of phase disruption on each ramp of what we would want to be 8 smooth ramps and ends up looking like 16 ramps. Work on polarisation eigenstates by Pezzaniti and Chipman [77] and Moreno et al. [78] suggests that TN technology phase modulation may be improved through the introduction of polarisation ellipticity but in order to understand the nature of this result,

further work is needed since their setups weren't completely followed since they use transmissive TN SLMs. Of special interest is that the wavefront form appears to be better: the ramp shape in the slopes is very close to what is predicted by the theoretical models and through adjustments and further investigation, perhaps the phase disruptions may be smoothed out allowing better modulation perhaps through the calibration of the gray levels of the spiral phase CGHs. Given these considerations, possible applications may be studied in future works regarding optical communications.

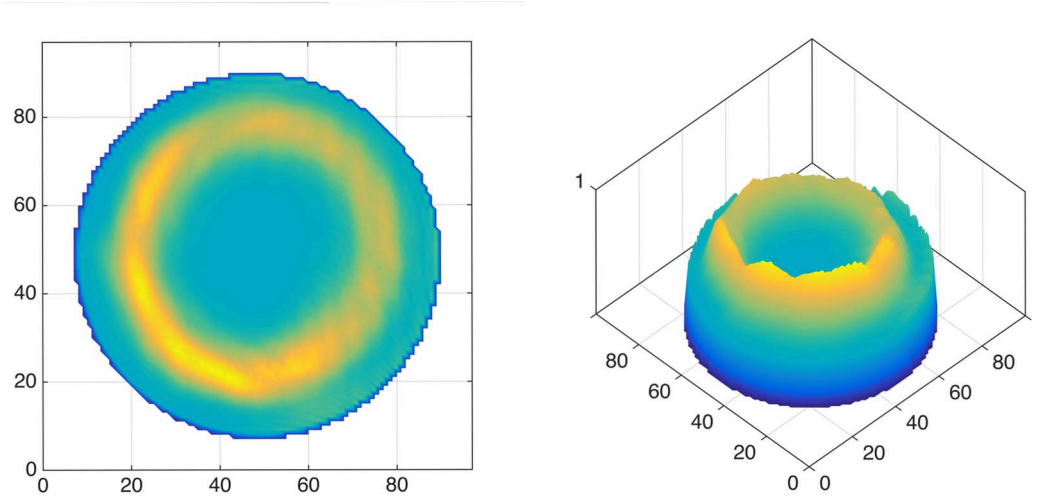

Figure 5.5: Normalized intensity profile for a $l = -1$ OAM beam (linearly polarised input beam and $|l| = 1$ forked diffraction CGH.)

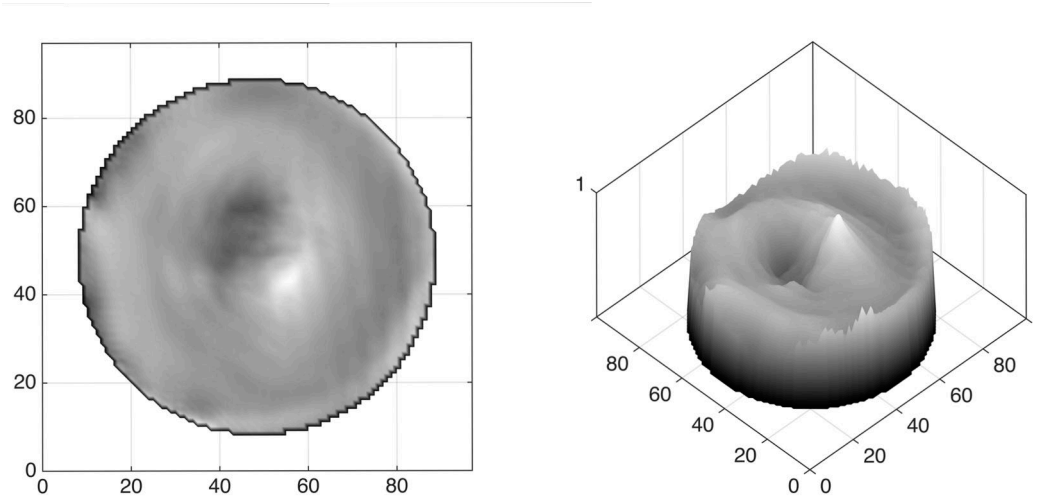

Figure 5.6: Normalized phase profile for a $l = -1$ OAM beam (linearly polarised input beam and $|l| = 1$ forked diffraction CGH.)

Forked Diffraction CGH

What appears to be the best result regarding OAM beams purity is obtained through forked diffraction CGHs since they possess a true vortex singularity and through diffraction, unmodulated light gathers at the 0^{th} order beam.

By using a $|l| = 1$ forked diffraction CGH to generate a pair of $l = 1$ and $l = -1$ OAM symmetric beams, the measured intensity of the $l = -1$ beam in figure 5.5 is an almost perfect shaped ring despite amplitude-phase

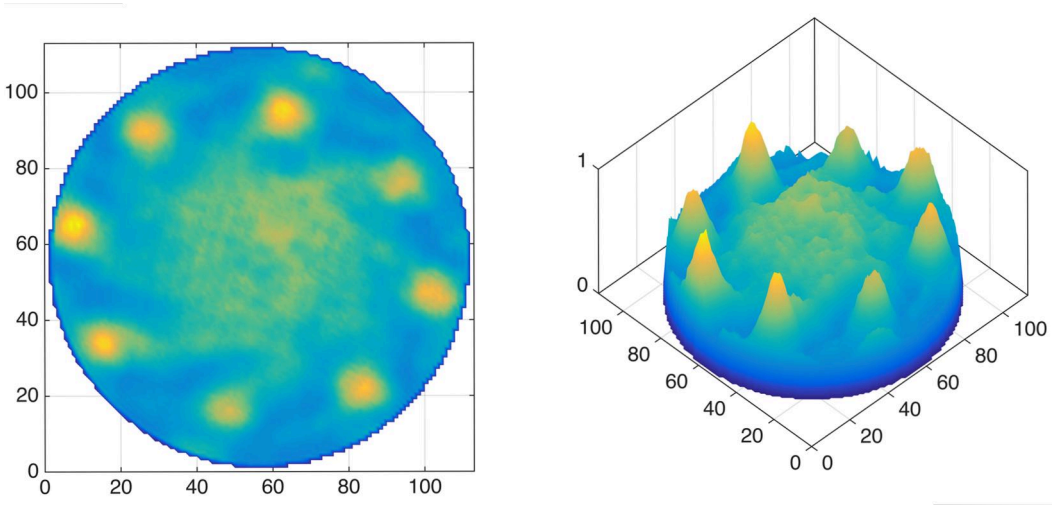

Figure 5.7: Normalized intensity profile for a $l = 8$ OAM beam (linearly polarised input beam and $l = 8$ spiral phase CGH generated on SLM 1 and reflected on turned off SLM 2).

coupling effects still being visible. The wavefront shape in figure 5.6 is also very good, closely resembling to a spiral ramp surrounding a singularity. Despite quite good, the effect of limited phase modulation capabilities of TN technology should exist between the maximum and minimum phase difference in the wavefront shape. Again, the simulation performed in chapter 3, section 3.3 was very good predicting this result.

OAM Demultiplexing

Regarding demodulation of OAM beams, only the most typical spiral phase CGH generated beams using linearly polarised light were demodulated. The demodulation proved itself more challenging than the beam generation process specially regarding alignment. The demodulation of the other generated beams was attempted, but the results were either inconclusive or unsuccessful. Time restrictions and a rather limited setup and lack of appropriate optical equipment at the time of this work reduced the possibilities of further work using other beams. Nevertheless, a continuation of this work is proposed in chapter 6, section 6.2.

Spiral Phase CGH Using a Linearly polarised Beam

Before proceeding to a OAM carrying beam demodulation, a $l = 8$ spiral phase CGH was loaded in the first SLM while maintaining the second SLM turned off. The result for intensity shown in figure 5.7 shows increased noise, probably induced by random modulation effects generated by the LC matrix but also beam deformation related to the angles of incidence and the lens used in the second SLM. Along with the increase of the noise, the random modulation effects are also visible because of the reduction of the intensity of the modulated peaks. Regarding the phase profile shown in figure 5.8, we can see that the wavefront modulation is maintained. Given this result, this result is unsuitable to use as a reference beam for our final result, regarding noise considerations. Because of this, a different approach to devise noise contributions was conceived and it shall be explained further on and was suggested in 4, section 4.6.

Proceeding to OAM demodulation, since we use a reflective SLM and considering that OAM charge flips with reflection, a $l = 8$ spiral phase CGH was loaded in the first SLM generating a $l = -8$ beam. Then, a

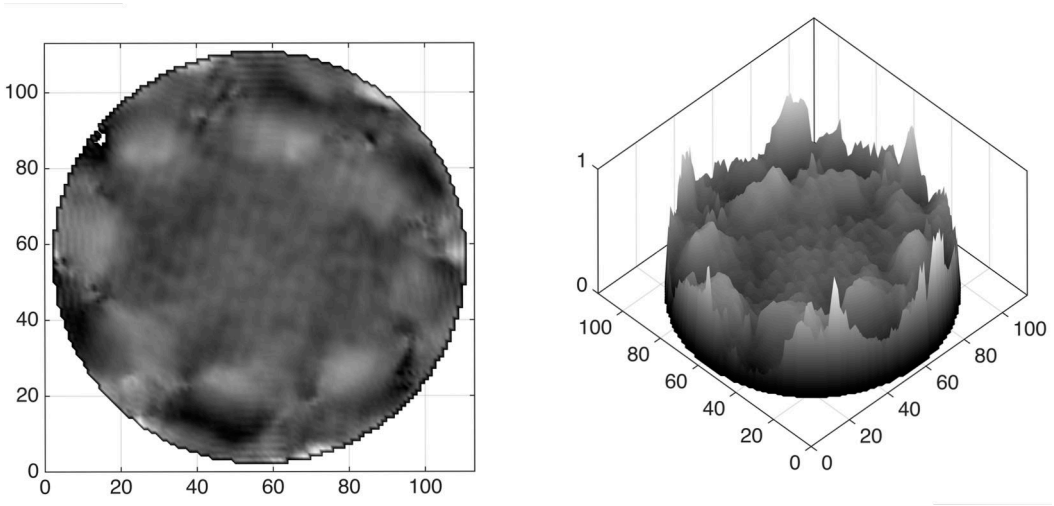

Figure 5.8: Normalized phase profile for a $l = 8$ OAM beam (linearly polarised input beam and $l = 8$ spiral phase CGH generated on SLM 1 and reflected on off SLM 2).

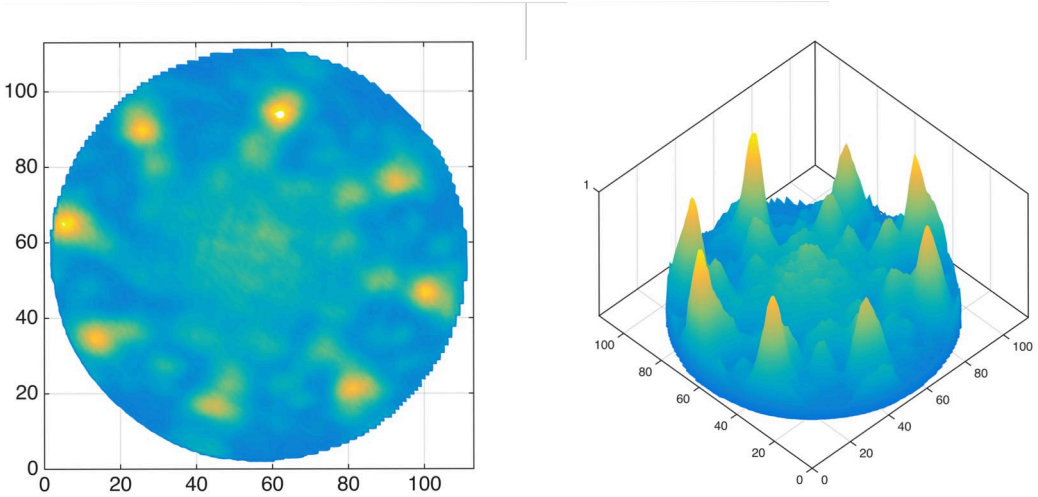

Figure 5.9: Normalized intensity profile for a $l = -8$ OAM demodulated beam (linearly polarised input beam and $l = 8$ spiral phase CGH generated on SLM 1 and demodulated on SLM 2 with $l = 8$ spiral phase CGH).

complementary $l = 8$ spiral phase CGH was loaded on the second SLM. The polar alignment of the second SLM was adjusted by using the ThorLabs mount cage system and through observation of the resulting beam in the CCD-WFS. It's possible that this alignment was needed because of optical misalignments but through the study of the inverse set of spiral phase CGHs it appears possible that the SLM modulation capabilities are flatter closer to 0 as it is expected in TN technology. However, the only way to assess this is through a interferometry study of the dynamic range of the SLM which should be done in future works in order to generate optimised phase modulation CGHs.

The obtained result for intensity shown in figure 5.9 was considered unclear. Despite a clear existence of intensity in the center, the majority of the intensity remains modulated as it can be seen through the peaks in the intensity profile. Recalling the results for the phase demodulation simulation in figure 3.13 and recalling that amplitude and phase coupling is expected, the core pattern appears similar to the one we simulated in phase. However, and despite the lack of a good reference for noise in this setup recalling the considerations above, further analysis was done and it is presented further on.

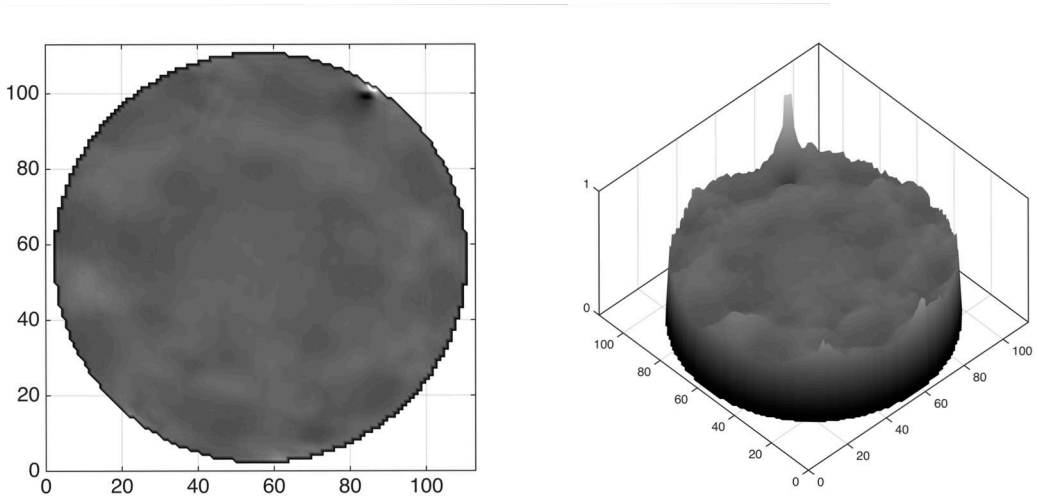

Figure 5.10: Normalized phase profile for a $l = -8$ OAM demodulated beam (linearly polarised input beam and $l = 8$ spiral phase CGH generated on SLM 1 and demodulated on SLM 2 with $l = 8$ spiral phase CGH).

Regarding phase, the result is quite satisfactory. Recalling that we measure residual phase effects considering a Gaussian beam reference, the residual phase for this beam is almost nonexistent and only an almost flat ring trace can be seen. Recalling the simulation in 3.13, it should be noticed that if the wavefront at the core in fact resembles a Gaussian or cylindrical profile, it is promptly removed since we only look for the residual phase profile. Recalling the simulation, it should be added that the residual continuos ring was predicted corresponding to the predominantly white annular region around the core in the simulation shown in figure 3.13. However, given the rather weak premises of this particular simulation, no strong conclusions should be derived.

Spiral Phase CGH Demodulation Control Test

In order to try to improve the comprehension of this results regarding noise, and as referred previously, a control test was devised. Since our SLM modulation capability is limited to less than 2π, perhaps modulation can be improved through the introduction of a similar phase profile instead of a complementary one. Therefore, enhanced phase modulation is expected (which also helps to verify the alignment) and if our result is related to random noise effects, both intensity profiles shouldn't be different. So, after the introduction of a $l = -8$ spiral phase CGH in the second SLM the results for both intensity and phase are shown in figure 5.11 and 5.12 respectively.

The obtained result for intensity shows what appears to be a lot of noise, but an interesting feature should be pointed. Unlike the previous result where a local maximum for intensity could be identified in the center, here the intensity at the core appears actually to diminish as we expect. It should be added that both the control and the standard tests were done in exactly the same conditions. However, the result by itself is unclear and further analysis is needed and was done further on.

Regarding the phase profile shown in figure 5.12, the result is quite clear. Unlike the standard demodulation where an almost flat profile is obtained, here we have an increased modulation behaviour, since the peaks are not only more clear than what we see in the almost flat phase profile of the standard test, but more pronounced than those of a standard OAM beam generated with this setup as shown in 5.8. Naturally, this

translates itself as a stronger intensity singularity in the core. Regarding the simulation shown in figure 3.12, it appears to be concordant given the enhanced phase peaks shown in the simulation. Then again, given the weak premises of this particular simulation, no strong conclusions should be derived.

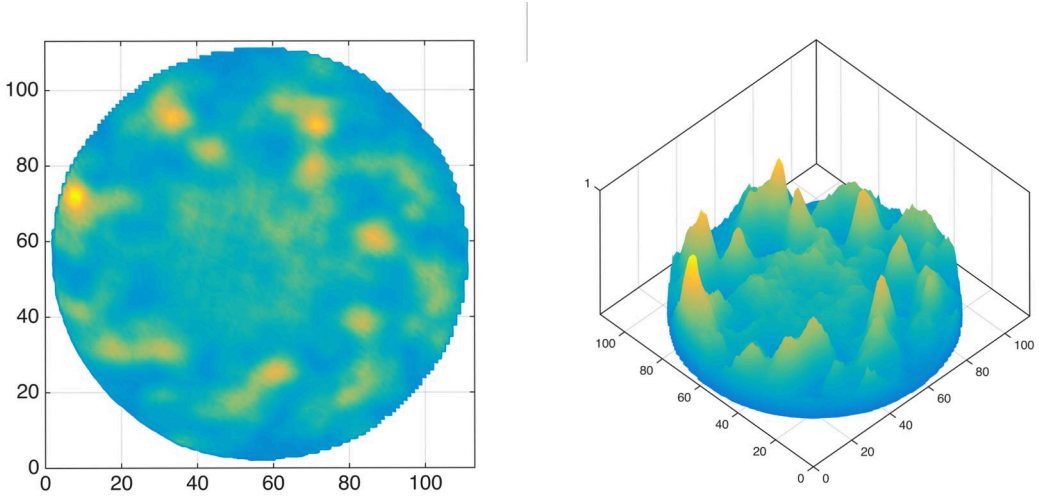

Figure 5.11: Normalized intensity profile for a double modulated $l = -8$ OAM beam (linearly polarised input beam and $l = 8$ spiral phase CGH generated on SLM 1 and remodulated on SLM 2 with $l = -8$ spiral phase CGH).

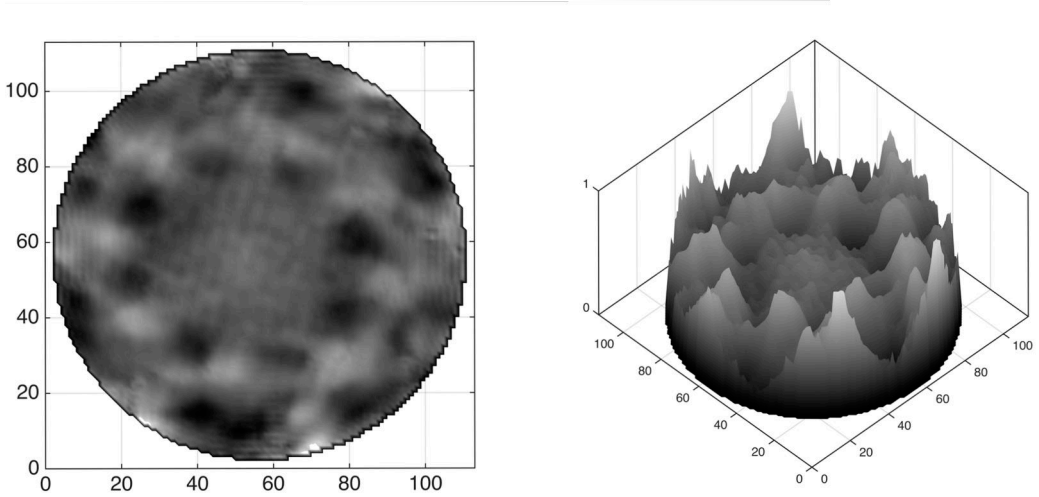

Figure 5.12: Normalized phase profile for a double modulated $l = -8$ OAM beam (linearly polarised input beam and $l = 8$ spiral phase CGH generated on SLM 1 and remodulated on SLM 2 with $l = -8$ spiral phase CGH).

Finally, in order to clarify the obtained intensity results for both the standard demodulation and the control test, an equal noise filter was applied in the data in order to enhance any hidden significance since the intensities are very weak. The results for the standard demodulation and the control test are shown in figures 5.13 and 5.14 respectively.

After applying the noise filter, our first impressions mentioned above are proven. The standard demodulation actually shows a central peak surrounded by a smaller vortex ring related to the reversal of the phase modulation which can also be seen, if we assume amplitude and phase coupling, in the simulation in 3.13. By opposition, the core of the control test intensity is almost flat, and the visible intensities are clearly due to inhomogeneities of the beam. The profile is far from clear, but the superposition of the peaks predicted in the

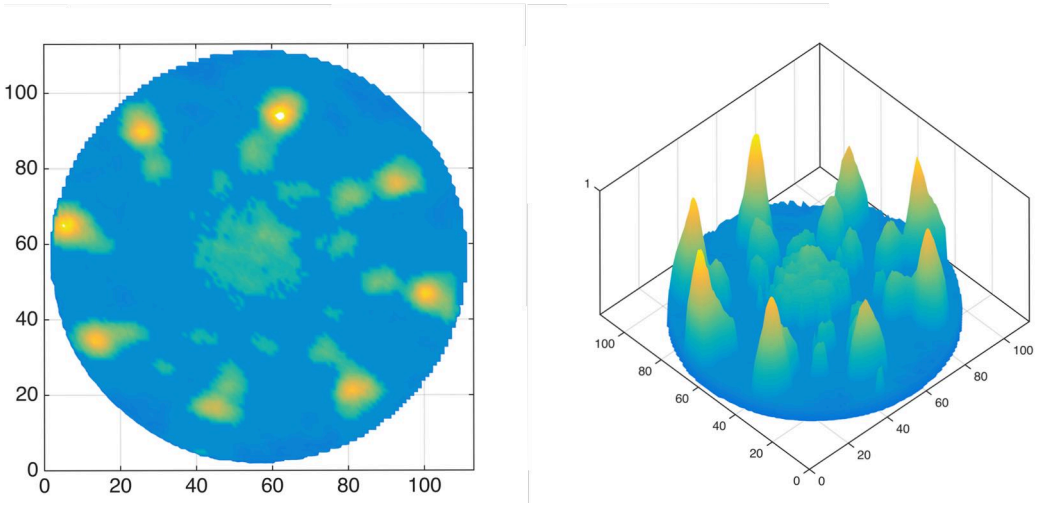

Figure 5.13: Noise filtered normalized intensity profile for a $l = -8$ OAM demodulated beam (linearly polarised input beam and $l = 8$ spiral phase CGH generated on SLM 1 and demodulated on SLM 2 with $l = 8$ spiral phase CGH).

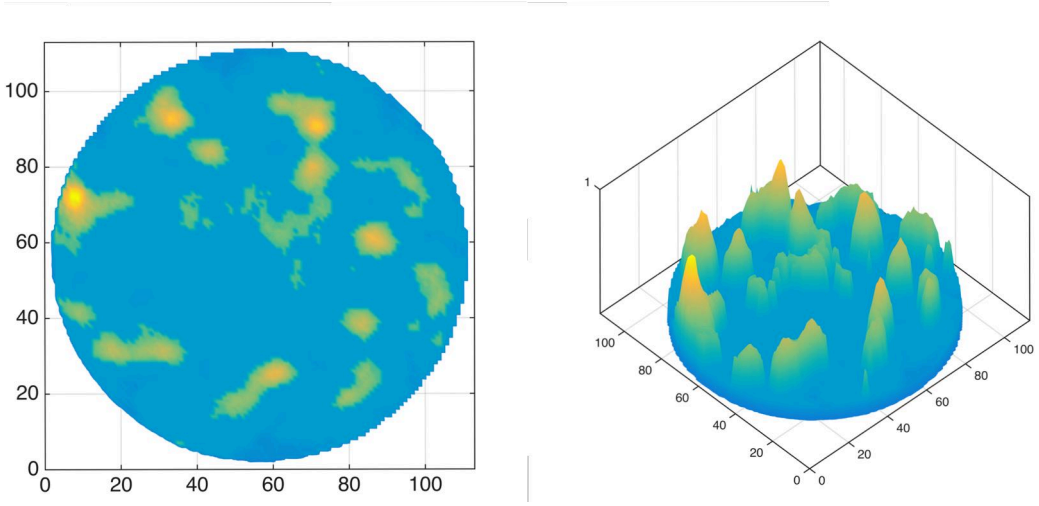

Figure 5.14: Noise filtered normalized intensity profile for a double modulated $l = -8$ OAM beam (linearly polarised input beam and $l = 8$ spiral phase CGH generated on SLM 1 and remodulated on SLM 2 with $l = -8$ spiral phase CGH).

simulation in figure 3.12 is also identifiable.

As a final test, both the original raw intensities for both the standard demodulation and the control test were subtracted in order to identify the noise and systematic inhomogeneities and the result is shown in figure 5.15. The result solidifies what we already saw in the former analysis. There's a clear local maximum at the core as expected through the demodulation of a OAM beam, and the effects of systematic inhomogeneities and noise common to both profiles is diminished. The core profile is in complete agreement with the simulation shown in figure 3.13, again assuming amplitude-phase coupling.

This experiments were also tried for inverse values of l and also for $|l| = 32$. The obtained results for a $l = -8$ spiral phase CGH were similar and while at $|l| = 32$ the OAM intensities become weaker since the SLM hasn't enough resolution to be able to modulate beams at such values of $|l|$ for this wavelength, and there's a big maximum at the core. However, performing similar studies regarding noise points to similar conclusions. Beams with $|l| = 16$ weren't studied in detail, but suffered from the same problems of $|l| = 32$ beams.

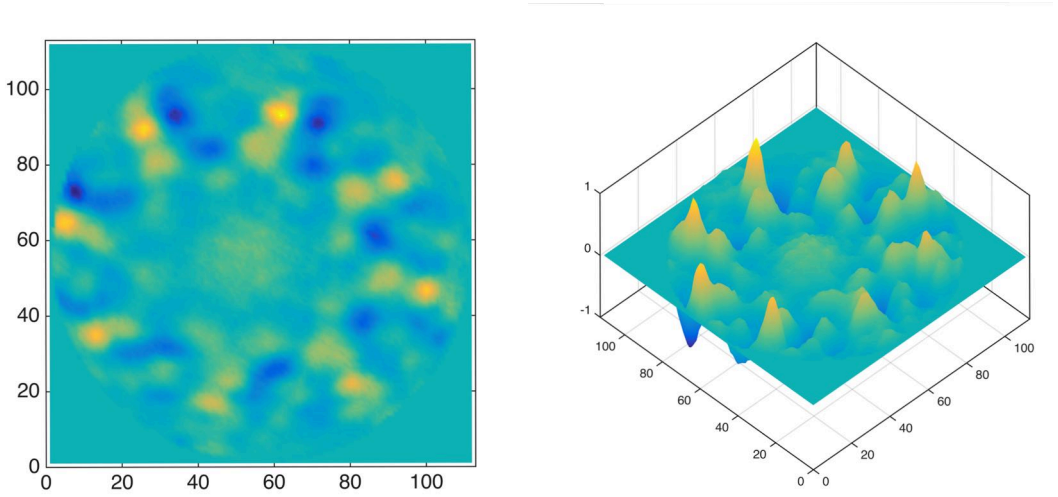

Figure 5.15: Normalized intensity profile for the subtraction of the demodulated $l = -8$ OAM beam by the double modulated $l = -8$ OAM beam (shown in figures 5.9 and 5.11 respectively).

6

Conclusions

Contents

Final Remarks

The corner stone of the proposal of this work was to establish a foundation for the study of the OAM of photons applied to optical communications. In order to achieve this, a rather comprehensive approach was chosen in order to connect the several areas of study that provide the technical and human motivation for this work.

Since a foundation assumes a continuation, we tried to be inclusive and started our state of the art in the regard of optical communications, followed the theoretical and experimental physics related to the OAM of light, proceeded to establish a theoretical context regarding some key concepts used in this area, from chosen topics of Fourier optics to the mathematical characterization of laser beam modes related to OAM, continued through the light-matter interaction physics in LCs behind the key device used in this work, the SLM in order to be ready to perform experiments and evaluate its results with a solid and comprehensive context.

From a technical point view, since it is a foundation work, a strong incidence was pointed to OAM carrying beam generation. Several approaches were experimented on, and their results were dissected and interpreted despite inherent limitations of used technology. In order to predict and build these experiments on OAM, a simple yet reliable simulation based on Fourier optics was conceived. Finally, regarding the basis of information multiplexing using OAM, a demodulation experiment was performed with some success.

Given this description, we consider the main objective of this work, to establish a basis for OAM study in optical communications, to have been accomplished.

Naturally, this is not without criticism. Several technical challenges were encountered, some were solved, some were not. However, reflection was given to these issues and several suggestions were made for future work, some of which are summed up in a proposal for a future work in this chapter, in section 6.2.

All and all, we end this work with a sense of accomplished mission, we think that any work that may follow, either more related to physics or optical communications has here a good starting point and we hope that this work helps to seed interest in the study of the fascinating world of twisted light and its applications.

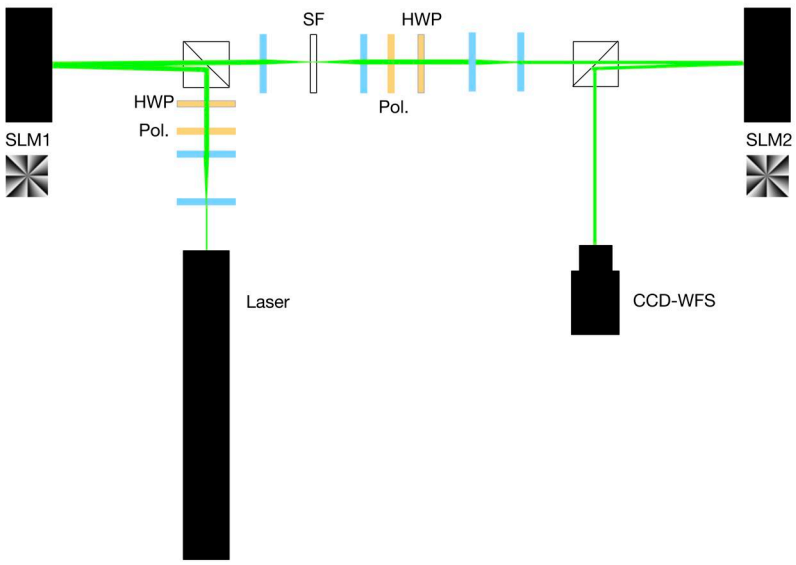

Figure 6.1: Improved setup for demultiplexing schematic (inverted mask shown for illustration purposes, due to the reflection the same mask must be used to demodulate the beam in the second SLM).

Future Work

As a final remark, and summing some of the suggestions made throughout this work, an improved setup for demodulation is proposed (see figure 6.1) and the key differences from the approach used in this work on chapter 4, section 4.6 shall be highlighted.

In order to reduce the noise resulting from the angle of incidence on the SLMs, a crossed nicols optical system is used as suggested by Hamamatsu guides for SLM usage. This method consists of using a beam splitter or a half mirror in order to incise the beam onto the SLM and then passing the modulated beam at a very closed angle through the same beam splitter or half mirror as an output exit. This is expected to greatly diminish the noise resulting from the wider angles of incidence and therefore improving the SLM efficiency. Wang et al. [48] and Bozinovic et al. [46] follow this kind of approach on their respective works.

Then, in order to clean the modulated beam by SLM1, the use of a spatial filter is advised. Again, by using a spatial filter we expect the resulting OAM beam to be cleaner than without it as it was shown by Luo et al. [80] and it is of notice that OAM is maintained through the passage by the spatial filter.

Another change I propose, is to follow Wang et al. [48] and use a green laser as it may be clear by the schematic in figure 6.1. Green lasers have smaller wavelengths and this expected to improve modulation near the singularity. It should be noticed that no actual calculations were made to corroborate this assertion considering the SLM we use and it may be possible that a green laser may result in weaker modulation due to less interaction, nevertheless, this option should be studied in more detail.

Another improvement that should be added is to use HWPs in agreement with the polarizers in order to obtain an control over the beams. This was actually tried out in the current work with partial success, but since the available equipment wasn't proper for a 632.8 nm wavelength, the results were mixed and we decided not to include it.

Naturally, we think it would be of interest to proceed demodulation studies using the several methods used to generate OAM beams in chapter 4, section 4.5.

Finally, we think the results obtained in chapter 5, section 5.2, subsection 5.2.2 suggest deeper study of the works by Pezzaniti and Chipman [77] and Moreno et al. [78] in order to try to exploit superior phase modulation through the use of QWPs in the setup.

From a practical point of view regarding the computational aspects, it would greatly improve the efficiency of the work at the laboratory to create a proper software solution to promptly introduce phase patterns by choosing a set of pre configured configurations and parameters. Also, work on the laboratory suggests that the calibration of the gray levels of the SLM would allow an optimized efficiency. This may be done through interferometry.

As miscellaneous suggestions, perhaps the simulations done in chapter 3, section 3.3 would be significantly improved by using a polar Fourier transform algorithm as the one proposed by Averbuch et al. [66]. Also of interest but a bit distant from this work, would be to study simulation methods for LCs interactions with light following works by Ruiz [65] or Saleh and Teich [58] for instance.

Bibliography

[1] André B Cunha, Gonçalo Figueira, and Paulo S André. Enabling the study of photons OAM applications for optical communications. In *The 23rd Annual International Conference on Advanced Laser Technologies ALT'15*, Faro, 2015. Instituto de Telecomunicações.

[2] André B Cunha, Gonçalo Figueira, and Paulo S André. Generation of Orbital Angular Momentum Beams . In *10a Conferência Nacional de Telecomunicações CONF TELE 2015*, Aveiro, 2015. Instituto de Telecomunicações.

[3] André B Cunha, Gonçalo Figueira, and Paulo S André. Enabling the study of photons OAM applications for optical communications. *Optical and Quantum Electronics*, 2015.

[4] C. E. Shannon. A mathematical theory of communication. *SIGMOBILE Mob. Comput. Commun. Rev.*, 5(1):3–55, January 2001. ISSN 1559-1662. doi: 10.1145/584091.584093.

[5] P J Winzer. Modulation and multiplexing in optical communication systems. *IEEE Leos Newsletter*, 2009.

[6] Y. A. Vlasov. Silicon photonics for next generation computing systems. In *Optical Communication, 2008. ECOC 2008. 34th European Conference on*, pages 1–2, Sept 2008. doi: 10.1109/ECOC.2008.4729553.

[7] A. F. Benner, M. Ignatowski, J. A. Kash, D. M. Kuchta, and M. B. Ritter. Exploitation of optical interconnects in future server architectures. *IBM Journal of Research and Development*, 49(4-5):755–776, 2005.

[8] Herwig Kogelnik. *On optical communication: Reflections and perspectives*. Massachusetts Institute of Technology, 2005.

[9] S. A. Townes, B. L. Edwards, A. Biswas, D. R. Bold, R. S. Bondurant, D. Boroson, J. W. Burnside, D. O. Caplan, A. E. DeCew, R. DePaula, R. J. Fitzgerald, F. I. Khatri, A. K. McIntosh, D. V. Murphy, B. A. Parvin, A. D. Pillsbury, W. T. Roberts, J. J. Scozzafava, J. Sharma, and M. Wright. The mars laser communication demonstration. In *Aerospace Conference, 2004. Proceedings. 2004 IEEE*, volume 2, pages 1180–1195 Vol.2, March 2004. doi: 10.1109/AERO.2004.1367717.

[10] S. Abbott. Review of 20 years of undersea optical fiber transmission system development and deployment since tat-8. In *Optical Communication, 2008. ECOC 2008. 34th European Conference on*, pages 1–1, Sept 2008. doi: 10.1109/ECOC.2008.4729092.

[11] J. A. Kash, F. E. Doany, C. L. Schow, R. Budd, C. Baks, D. M. Kuchta, P. Pepeljugoski, L. Schares, R. Dangel, F. Horst, B. J. Offrein, C. Tsang, N. Ruiz, C. Patel, R. Horton, F. Libsch, and J. U. Knickerbocker. Terabus: Chip-to-chip board-level optical data buses. In *Lasers and Electro-Optics Society, IEEE LEOS Annual Meeting*, 2008. doi: 10.1109/LEOS.2008.4688718.

[12] Graham Gibson, Johannes Courtial, Miles Padgett, Mikhail Vasnetsov, Valeriy Pas'ko, Stephen Barnett, and Sonja Franke-Arnold. Free-space information transfer using light beams carrying orbital angular momentum. *Optics Express*, 12(22):5448–5456, November 2004.

[13] Gabriel Molina-Terriza, Juan P Torres, and Lluis Torner. Twisted photons. *Nature Physics*, 3(5):305–310, May 2007.

[14] Kazuro Kikuchi. Coherent optical communication systems. *Optical Fiber Telecommunications VB: systems and networks*, 2008.

[15] Hiroaki Sanjoh, Eiichi Yamada, and Yuzo Yoshikuni. Optical orthogonal frequency division multiplexing using frequency/time domain filtering for high spectral efficiency up to 1 bit/s/hz. In *Optical Fiber Communication Conference and Exhibit, 2002. OFC 2002*, pages 401–402. IEEE, 2002.

[16] Sander L Jansen, Itsuro Morita, Kamyar Forozesh, Sebastian Randel, Dirk van den Borne, and Hideaki Tanaka. Optical OFDM, a hype or is it for real? In *2008 34th European Conference on Optical Communication*, pages 1–4. IEEE.

[17] W A Atia and R S Bondurant. Demonstration of return-to-zero signaling in both OOK and DPSK formats to improve receiver sensitivity in an optically preamplified receiver. *LEOS '99. IEEE Lasers and Electro-Optics Society 1999 12th Annual Meeting*, 1:226–227, 1999.

[18] C R Fludger, T Duthel, D Van den Borne, C Schulien, E-D Schmidt, T Wuth, E de Man, G D Khoe, and H de Waardt. 10 x 111 Gbit/s, 50 GHz Spaced, POLMUX-RZ-DQPSK Transmission over 2375 km Employing Coherent Equalisation. *Optical Fiber Communication Conference and Exposition and The National Fiber Optic Engineers Conference (2007), paper PDP22*, page PDP22, March 2007.

[19] Xiang Zhou, Jianjun Yu, Dayou Qian, Ting Wang, Guodong Zhang, and Peter Magill. 8x114 Gb/s, 25-GHz-Spaced, PolMux-RZ-8PSK Transmission over 640 km of SSMF Employing Digital Coherent Detection and EDFA-Only Amplification. *Optical Fiber Communication Conference/National Fiber Optic Engineers Conference (2008), paper PDP1*, page PDP1, February 2008.

[20] P J Winzer and A H Gnauck. *112-Gb/s polarisation-multiplexed 16-QAM on a 25-GHz WDM grid*. Proc. ECOC, 2008.

[21] David O Caplan, Bryan S Robinson, Robert J Murphy, and Mark L Stevens. Demonstration of 2.5 Gslot/s Optically-Preamplified M-PPM with 4 Photons/Bit Receiver Sensitivity. *Optical Fiber Communication Conference and Exposition and The National Fiber Optic Engineers Conference (2005), paper PDP32*, page PDP32, March 2005.

[22] D O Caplan and W A Atia. *A quantum-limited optically-matched communication link*. … Communication Conference and Exhibit, 2001.

[23] Hidenori Takahashi, Abdullah Al Amin, Sander L Jansen, Itsuro Morita, and Hideaki Tanaka. 8x66.8-gbit/s coherent pdm-ofdm transmission over 640 km of ssmf at 5.6-bit/s/hz spectral efficiency. In *2008 34th European Conference on Optical Communication*, pages 1–2. IEEE, 2008.

[24] M Nakazawa. Challenges to FDM-QAM coherent transmission with ultrahigh spectral efficiency. In *Optical Communication, 2008. ECOC 2008. 34th European Conference on*, pages 1–2. IEEE, 2008.

[25] A E Willner, H Huang, Y Yan, Y Ren, N Ahmed, G Xie, C Bao, L Li, Y Cao, Z Zhao, J Wang, M P J Lavery, M Tur, S Ramachandran, A F Molisch, N Ashrafi, and S Ashrafi. Optical communications using orbital angular momentum beams. *Advances in Optics and Photonics*, 7(1):1–42, March 2015.

[26] Richard A. Beth. Mechanical detection and measurement of the angular momentum of light. *Phys. Rev.*, 50:115–125, Jul 1936. doi: 10.1103/PhysRev.50.115.

[27] M J Padgett and L Allen. Light with a twist in its tail. *Contemporary Physics*, 41(5):275–285, May 2000.

[28] D.K. Cheng. *Field and wave electromagnetics*. The Addison-Wesley series in electrical engineering. Addison-Wesley Publishing Company, 1989. ISBN 9780201528206.

[29] B.E.A. Saleh and M.C. Teich. *Fundamentals of Photonics*. Wiley Series in Pure and Applied Optics. Wiley, 2007. ISBN 9780471358329.

[30] L Allen, M W Beijersbergen, R J Spreeuw, and J P Woerdman. Orbital angular momentum of light and the transformation of Laguerre-Gaussian laser modes. *Physical review. A*, 45(11):8185–8189, June 1992.

[31] Alison M Yao and M J Padgett. Orbital angular momentum: origins, behavior and applications. *Advances in Optics and Photonics*, 3(2):161–204, 2011.

[32] L Allen and M J Padgett. The Poynting vector in Laguerre-Gaussian laser modes. 1995.

[33] John David Jackson. *Classical electrodynamics*. Wiley, New York, NY, 3rd ed. edition, 1999. ISBN 9780471309321.

[34] Juan P Torres and Lluis Torner. *Twisted Photons*. Applications of Light with Orbital Angular Momentum. John Wiley & Sons, March 2011.

[35] Stephen M Barnett and L Allen. Orbital angular momentum and nonparaxial light beams. *Optics Communications*, 110(5):670–678, December 1993.

[36] J H Poynting. The Wave Motion of a Revolving Shaft, and a Suggestion as to the Angular Momentum in a Beam of Circularly Polarised Light. *Proceedings of the Royal Society A: Mathematical, Physical and Engineering Sciences*, 82(557):560–567, July 1909.

[37] Jonathan Leach, Stephen Keen, M J Padgett, Christopher Saunter, and Gordon D Love. Direct measurement of the skew angle of the Poynting vector in a helically phased beam. *Optics Express*, 14(25): 11919–11924, December 2006.

[38] N Bozinovic. Orbital angular momentum in optical fibers. 2013.

[39] S Ramachandran, N Bozinovic, P Gregg, S E Golowich, and P Kristensen. Optical vortices in fibres: A new degree of freedom for mode multiplexing. In *Optical Communications (ECOC), 2012 38th European Conference and Exhibition on*, pages 1–3, 2012.

[40] E Abramochkin and V Volostnikov. Beam transformations and nontransformed beams. *Optics Communications*, 83(1):123–135, May 1991.

[41] N González, G Molina-Terriza, and J P Torres. How a Dove prism transforms the orbital angular momentum of a light beam. *Optics Express*, 14(20):9093–9102, October 2006.

[42] G Swartzlander Jr and R Hernandez-Aranda. Optical Rankine vortex and anomalous circulation of light. 2007.

[43] J Courtial. Light's orbital angular momentum. *Physics Today*, 2004.

[44] Stuart D. Coomber, Colin D. Cameron, Jonathon R. Hughes, David T. Sheerin, Christopher W. Slinger, Mark A. G. Smith, and Maurice Stanley. Optically addressed spatial light modulators for replaying computer-generated holograms, 2001.

[45] Jonathan Leach and Miles Padgett. Observation of chromatic effects near a white-light vortex. *New Journal of Physics*, 5(1):154–154, November 2003.

[46] N Bozinovic, Y Yue, Y Ren, M Tur, P Kristensen, H Huang, A E Willner, and S Ramachandran. Terabit-scale orbital angular momentum mode division multiplexing in fibers. *Science*, 340(6140):1545–1548, June 2013.

[47] J Carpenter and T D Wilkinson. All Optical Mode-Multiplexing Using Holography and Multimode Fiber Couplers. *Lightwave Technology, Journal of*, 30(12):1978–1984, June 2012.

[48] Jian Wang, Jeng-Yuan Yang, Irfan M Fazal, Nisar Ahmed, Yan Yan, Hao Huang, Yongxiong Ren, Yang Yue, Samuel Dolinar, Moshe Tur, and Alan E Willner. Terabit free-space data transmission employing orbital angular momentum multiplexing. *Nature Photonics*, 6(7):488–496, July 2012.

[49] Hao Huang, Guodong Xie, Yan Yan, Nisar Ahmed, Yongxiong Ren, Yang Yue, Dvora Rogawski, Moshe Tur, Baris Erkmen, Kevin Birnbaum, Samuel Dolinar, Martin Lavery, Miles Padgett, and Alan E Willner. 100 Tbit/s Free-Space Data Link using Orbital Angular Momentum Mode Division Multiplexing Combined with Wavelength Division Multiplexing. *Optical Fiber Communication Conference/National Fiber Optic Engineers Conference 2013 (2013), paper OTh4G.5*, page OTh4G.5, March 2013.

[50] Shuhui Li and Jian Wang. A Compact Trench-Assisted Multi-Orbital-Angular-Momentum Multi-Ring Fiber for Ultrahigh-Density Space-Division Multiplexing (19 Rings 3 22 Modes) . *Scientific Reports*, 4: 1–8, January 2014.

[51] N K Fontaine, C R Doerr, and L L Buhl. Efficient multiplexing and demultiplexing of free-space orbital angular momentum using photonic integrated circuits. In *Optical Fiber Communication Conference and Exposition (OFC/NFOEC), 2012 and the National Fiber Optic Engineers Conference*, pages 1–3. IEEE, 2012.

[52] R J Essiambre, R Ryf, N K Fontaine, and S Randel. Breakthroughs in Photonics 2012: Space-Division Multiplexing in Multimode and Multicore Fibers for High-Capacity Optical Communication. *IEEE Photonics Journal*, 5(2):0701307–0701307, April 2013.

[53] H Huang, Y Yue, Y Yan, N Ahmed, and Y Ren. Orbital-Angular-Momentum-Based Reconfigurable and "Lossless" Optical Add/Drop Multiplexing of Multiple 100-Gbit/s Channels. *Optical Fiber …*, 2013.

[54] Tiehui T Su, Ryan P RP Scott, Stevan S SS Djordjevic, Nicolas K NK Fontaine, David J DJ Geisler, Xinran X Cai, and S J B SJ Yoo. Demonstration of free space coherent optical communication using integrated silicon photonic orbital angular momentum devices. *Optics Express*, 20(9):9396–9402, April 2012.

[55] G Molina-Terriza, A Vaziri, R Ursin, and A Zeilinger. Experimental Quantum Coin Tossing. *Physical Review Letters*, 94(4):40501, January 2005.

[56] Joseph W Goodman and Steven C Gustafson. *Introduction to Fourier Optics*, volume 35. International Society for Optics and Photonics, second edition edition, May 1996.

[57] Werner Lauterborn, Thomas Kurz, and Martin Wiesenfeldt. *Coherent Optics*. Fundamentals and Applications. Springer Science & Business Media, April 2013.

[58] Bahaa E A Saleh and Malvin Carl Teich. *Fundamentals of Photonics*. John Wiley & Sons, February 2013.

[59] Vasudevan Lakshmi Narayanan, María L Calvo, and Tatiana Alieva. *Mathematical Optics*. Classical, Quantum, and Computational Methods. CRC Press, December 2012.

[60] Pascal Picart and Jun-chang Li. *Digital Holography*. John Wiley & Sons, January 2013.

[61] Taro Ando, Yoshiyuki Ohtake, Naoya Matsumoto, Takashi Inoue, and Norihiro Fukuchi. Mode purities of Laguerre-Gaussian beams generated via complex-amplitude modulation using phase-only spatial light modulators. *Optics Letters*, 34(1):34–36, January 2009.

[62] Victor Arrizón, Ulises Ruiz, Rosibel Carrada, and Luis A González. Pixelated phase computer holograms for the accurate encoding of scalar complex fields. *Journal of the Optical Society of America A*, 24(11): 3500–9, 2007.

[63] Ting-Chung Poon and Jung-Ping Liu. *Introduction to modern digital holography: with Matlab*. Cambridge University Press, New York, NY, 2014.

[64] Naoya Matsumoto, Taro Ando, Takashi Inoue, Yoshiyuki Ohtake, Norihiro Fukuchi, and Tsutomu Hara. Generation of high-quality higher-order Laguerre-Gaussian beams using liquid-crystal-on-silicon spatial light modulators. *Journal of the Optical Society of America A*, 25(7):1642–1651, July 2008.

[65] A M Ruiz. Accurate predictive model for twisted nematic liquid crystal devices [: application for generating programmable apodizers and Fresnel lenses, 2001.

[66] A Averbuch, R R Coifman, D L Donoho, M Elad, and M Israeli. Fast and accurate Polar Fourier transform. *Applied and Computational Harmonic Analysis*, 21(2):145–167, September 2006.

[67] Daryl Preece. *Novel Uses of Spatial Light Modulators in Optical Tweezers*. PhD thesis, March 2011.

[68] Keigo Iizuka. *Elements of Photonics, In Free Space and Special Media*. John Wiley & Sons, June 2002.

[69] P Ambs. Characterization of an analog ferroelectric spatial light modulator application to dynamic diffractive optical elements and optical information processing. pages 1–29, June 2001.

[70] S M Kelly and M O'Neill. Liquid crystals for electro-optic applications. *Handbook of advanced electronic and …*, 2000.

[71] Bahaa EA Saleh and Kanghua Lu. Theory and design of the liquid crystal tv as an optical spatial phase modulator. *Optical Engineering*, 29(3):240–246, 1990.

[72] Dwight W. Berreman. Optics in stratified and anisotropic media: 4×4-matrix formulation. *J. Opt. Soc. Am.*, 62(4):502–510, Apr 1972. doi: 10.1364/JOSA.62.000502.

[73] Dwight W. Berreman. Optics in smoothly varying anisotropic planar structures: Application to liquid-crystal twist cells∗. *J. Opt. Soc. Am.*, 63(11):1374–1380, Nov 1973. doi: 10.1364/JOSA.63.001374.

[74] Naim Konforti, S-T Wu, and E Marom. Phase-only modulation with twisted nematic liquid-crystal spatial light modulators. *Optics letters*, 13(3):251–253, 1988.

[75] Thomas H Barnes, Tomoaki Eiju, Kiyofumi Matusda, and Naotake Ooyama. Phase-only modulation using a twisted nematic liquid crystal television. *Applied optics*, 28(22):4845–4852, 1989.

[76] M V Berry. Optical vortices evolving from helicoidal integer and fractional phase steps. *Journal of Optics A: Pure and Applied Optics*, 6(2):259–268, January 2004.

[77] J L Pezzaniti and R A Chipman. Phase-only modulation of a twisted nematic liquid-crystal TV by use of the eigenpolarisation states. *Optics Letters*, 18(18):1567–4, 1993.

[78] Ignacio Moreno, Jeffrey A Davis, Carlos R Fernández-Pousa, and David J Franich. polarisation eigenvectors for reflective twisted nematic liquid crystal displays. *Optical Engineering*, 40(10):2220, October 2001.

[79] Miles J Padgett, Filippo M Miatto, Martin Lavery, Anton Zeilinger, and Robert W Boyd. Divergence of an orbital-angular-momentum-carrying beam upon propagation. *arXiv.org*, (2):023011, October 2014.

[80] Jia Luo, Hongxin Huang, Yoshinori Matsui, Haruyoshi Toyoda, Takashi Inoue, and Jian Bai. High-order optical vortex position detection using a Shack-Hartmann wavefront sensor. *Optics Express*, 23(7): 8706–14, 2015.

[81] Andrey S Ostrovsky, Carolina Rickenstorff-Parrao, and Miguel Á Olvera-Santamaría. Using the Liquid Crystal Spatial Light Modulators for Control of Coherence and polarisation of Optical Beams, 2011.

[82] Mario Krenn, Robert Fickler, Matthias Fink, Johannes Handsteiner, Mehul Malik, Thomas Scheidl, Rupert Ursin, and Anton Zeilinger. Communication with spatially modulated light through turbulent air across Vienna. *New Journal of Physics*, 16(11):1–11, November 2014.

[83] J Lin, X C Yuan, S H Tao, and R E Burge. Multiplexing free-space optical signals using superimposed collinear orbital angular momentum states. *Applied Optics*, 46(21):4680–4685, July 2007.

[84] Alipasha Vaziri, Gregor Weihs, and Anton Zeilinger. Superpositions of the orbital angular momentum for applications in quantum experiments. *Journal of Optics B: Quantum and …*, 4(2):S47–S51, April 2002.

[85] J B Götte and S M Barnett. Quantum formulation of angle and orbital angular momentum. Cambridge University Press, Cambridge, 2009.

[86] Jaime A Anguita, Joaquin Herreros, and Ivan B Djordjevic. Coherent Multimode OAM Superpositions for Multidimensional Modulation. *IEEE Photonics Journal*, 6(2):1–11, March 2014.

[87] Jörg B Götte, Kevin O'Holleran, Daryl Preece, Florian Flossmann, Sonja Franke-Arnold, Stephen M Barnett, and Miles J Padgett. Light beams with fractional orbital angular momentum and their vortex structure. *Optics Express*, 16(2):993–1006, January 2008.

[88] Y Zhang, L Y Wu, and J Zhang. Study on the Phase Modulation Characteristics of Liquid Crystal Spatial Light Modulator. *Journal of Physics: Conference Series*, 48:790–794, October 2006.

[89] Long Zhu and Jian Wang. Arbitrary manipulation of spatial amplitude and phase using phase-only spatial light modulators. *Scientific Reports*, 4:7441–7, December 2014.

[90] E G van Putten, I M Vellekoop, and A P Mosk. Spatial amplitude and phase modulation using commercial twisted nematic LCDs. *Applied Optics*, 47(12):2076–2081, April 2008.

[91] R Bowman, V D'Ambrosio, E Rubino, O Jedrkiewicz, P Di Trapani, and M J Padgett. Optimisation of a low cost SLM for diffraction efficiency and ghost order suppression. *The European Physical Journal Special Topics*, 199(1):149–158, December 2011.

[92] Ajoy Ghatak and K Thyagarajan. *An Introduction to Fiber Optics*. Cambridge University Press, June 1998.

[93] Richard E. Wagner. Fiber based broadband access technology and deployment. *Optical Fiber Telecommunications, Vol. VB of Systems and Networks, IP Kaminow*, 2008.

[94] G. E. Moore. Cramming more components onto integrated circuits. *Electronics*, 38(8):114–117, April 1965. ISSN 0018-9219. doi: 10.1109/jproc.1998.658762.

A

Additional Tables

N. of Cores	OAM modes	Other	SDM ch.	WDM ch.	Mod. (GBaud)	ETDM (B.R.[a])	Agg. capacity	Lenght (m)	Year
1	2	0	2	10	20 (16-QAM)	4 Gbit/s	1.6 Tbit/s	1100	2013[46]
1	2	2	2	1	50 (QPSK)	2 Gbit/s	0.4 Tbit/s		
1	1	1	1	1	28 (QPSK)	2 Gbit/s	0.1 Tbit/s	8000	2013[47]
1	1	1	1	1	28 (QPSK)	2 Gbit/s	0.1 Tbit/s	2000	
19	18	4	1	137	42.8 (16-QAM)	4 Gbit/s	9.8 Pbit/s	1000[b]	2014[50]
-	24	0	1	42	50 (QPSK)	2 Gbit/s	0.1 Pbit/s	1 (F.S.[c])	2013[49]
-	8	2	2	1	20 (16-QAM)	4 Gbit/s	2.6 Tbit/s	1 (F.S.[c])	2012[48]
-	4	2	1	1	42.8 (16-QAM)	4 Gbit/s	1.4 Tbit/s		

Table A.1: Latest OAM transmission performances in optic fibers and free space.

[a] Bit rate.
[b] Expected theoretical result for proposed experiment.
[c] Free space.

SDE1024 SLM Technical Properties	
Bit-depth	8-bit
Pixel pitch	9 m per 9 m
Reflectance	62% at 633 nm
Operating temperature	0 °C to 50 °C
Active area diagonal	1.14 cm
Active area dimensions	9.3 mm per 7 mm
LCs	Twsited Nematic Liquid Crystal
Input polarisation	Parallel with longest side
Contrast ratio	350:1
LC response time	200 s
Interface	VGA
Input voltage	5 V
Retardation	$\sim 0.8\pi$ at 633 nm
Resolution	1024 px per 640 px
Operating wavelenght	430 nm to 650 nm

Table A.2: Cambridge Correlators SDE1024 SLM technical properties as presented by the supplier.

B

Code

phasemask.m

```
clear all
close all
clc
x = -512 : 1 : 512; % a row-vector of points for the x-axis
y = -512 : 1 : 512; % a row-vector of points for the y-axis
[X,Y] = meshgrid(x,y); % create matrices for grids of X and Y
T_0 = 1;
alpha = 1; %amplitude of the phase modulation
l = 2; %topological charge absolute value
bigdelta = 150; %controls the period of the grating (fringe spacing)
%bigdelta = 100
G = bigdelta;
[M,N] = size(X);
for m = 1:M
for n = 1:N
q = atan2(Y(m,n),X(m,n));
r = sqrt(Y(m,n)^2 + X(m,n)^2);
T(m,n) = mod(q*l,2*pi); % spiral phase mask
%T(m,n) = T_0*exp(alpha*1i*cos(l/2*q-(2*pi*r*cos(q))/G)); % forked diffraction grating
%T(m,n) = 1;
end
end

Treal = real(T);
gray_colormap = colormap('gray');

fig1 = figure(1);
figure(1);
fig1_colormap = 1 - gray_colormap;
pcolor(X,Y,Treal)
colormap(fig1_colormap)
shading interp %(removes the grid)
pos1 = get(gca, 'Position');
pos1(1) = 0.0;
pos1(2) = 0.0;
pos1(3) = 1;
pos1(4) = 1;
set(gca, 'Position', pos1)
axis('square')
axis('off')
set(gcf,'PaperUnits','points','PaperSize',[1,1],'PaperPosition',[0 0 1024 1024])
print('-dpng','-r72','p-mask')
print('-dbmp','-r72','p-mask')

fig2 = figure(2);
figure(2);
fig2_colormap = gray_colormap;
pcolor(X,Y,Treal)
colormap(fig2_colormap)
shading interp
pos2 = get(gca, 'Position');
pos2(1) = 0.0;
pos2(2) = 0.0;
pos2(3) = 1;
pos2(4) = 1;
set(gca, 'Position', pos2)
axis('square')
axis('off')
set(gcf,'PaperUnits','points','PaperSize',[1,1],'PaperPosition',[0 0 1024 1024])
print('-dpng','-r72','n-mask')
print('-dbmp','-r72','n-mask')
```

propagation.m

```
%------------------------------Fresnel Diffraction Approximation------------------------------
% Variables :
% w : laser wavelength (mm);
% z0 : diffraction plane distance (mm);
% U0 : complex amplitude of the starting optical field;
% L0 : width of the starting optical field and plane (mm);
%-----------------------------------------------------------------------------------------------
clear;close all;

% Starting field profile image input
root='';
[name,root]=uigetfile([root,'*.*'],['Starting field']);
[XRGB,MAP]=imread([root,name]);
X=XRGB(:,:,1);

% Variables input
w=input('Wavelength (mm) : ');
L0=input('Width of the starting field L0 (mm) : ');
k=2*pi/w;
[M,N]=size(X);
X=double(X);
A=max(M,N)

% Squaring by filling it with zeros the starting image to get a AxA size
Z1=zeros(A,(A-N)/2);
Z2=zeros((A-M)/2,N);
UT=[Z1,[Z2;X;Z2],Z1]; % Temporary starting field variable

% Maximum distance to fullfill sampling theorem
zmax=L0^2/A/w;

% Variable input
disp(['Maximum distance to comply with the sampling theorem : ',num2str(zmax),' mm']);
z0=input(['Diffracted field distance z0 (mm) (<',num2str(zmax),'mm) : ']);
U0=UT; % Starting field variable U0

% Grayscale mesh applied to starting field
figure(1),imagesc(UT),colormap(flipud('gray'));ylabel('pixels');
axis equal;axis tight;
xlabel(['Width of the starting field =',num2str(L0),' mm']);title('Starting amplitude ');

%----------------------------------Diffraction FFT algorithm----------------------------------

Uf=fft2(U0,A,A); % Work variable for input field

Uf=fftshift(Uf); % Spectrum of the starting field

fex=A/L0;fey=fex; % Spatial frequencies calculation

fx=[-fex/2:fex/A:fex/2-fex/A]; % Spatial frequency range for x

fy=[-fey/2:fey/A:fey/2-fey/A]; % Spatial frequency range for y

[FX,FY]=meshgrid(fx,fy); % Spatial frequency mesh space

% Angular spectrum transfer function
H=exp(i*k*z0)*exp(-i*pi*w*z0*(FX.^2+FY.^2)); %Fresnel
%H=exp(i*z0*sqrt(k^2-(FX.^2+FY.^2))); %Fraunhofer

% Diffraction convolution
result=Uf.*H;

% Inverse Fourier transform to return to spatial coordinates
Uf=ifft2(result,A,A);
%-------------------------------------End of FFT algorithm-------------------------------------

If=abs(Uf);
figure(2),imagesc(abs(Uf)),colormap(gray);ylabel('pixels');
axis equal;axis tight;
xlabel(['Diffraction distance = ',num2str(z0),' mm, Plane width= ',num2str(L0),'mm']);...
    title('Amplitude of field diffracted by FFT');
%-----------------------------------------------------------------------------------------------

fig1 = figure(1);
figure(1);
%fig1_colormap = 1 - gray_colormap;
%pcolor(X,Y,Treal)
%colormap(fig1_colormap)
shading interp %(removes the grid)
pos1 = get(gca, 'Position');
pos1(1) = 0.0;
```

```
82  pos1(2) = 0.0;
83  pos1(3) = 1;
84  pos1(4) = 1;
85  set(gca, 'Position', pos1)
86  axis('square')
87  axis('off')
88  set(gcf,'PaperUnits','points','PaperSize',[1,1],'PaperPosition',[0 0 1024 1024])
89  print('-dpng','-r72','dif-p-mask')
90  print('-dbmp','-r72','dif-p-mask')
91
92  fig2 = figure(2);
93  figure(2);
94  %fig2_colormap = gray_colormap;
95  %pcolor(X,Y,Treal)
96  %colormap(fig2_colormap)
97  shading interp
98  pos2 = get(gca, 'Position');
99  pos2(1) = 0.0;
100 pos2(2) = 0.0;
101 pos2(3) = 1;
102 pos2(4) = 1;
103 set(gca, 'Position', pos2)
104 axis('square')
105 axis('off')
106 set(gcf,'PaperUnits','points','PaperSize',[1,1],'PaperPosition',[0 0 1024 1024])
107 print('-dpng','-r72','dif-n-mask')
108 print('-dbmp','-r72','dif-n-mask')
```